UNIVERSITÀ DEGLI STUDI DI MESSINA

DIPARTIMENTO DI SCIENZE MATEMATICHE E INFORMATICHE,
SCIENZE FISICHE E SCIENZE DELLA TERRA

Dottorato di Ricerca in Fisica

XXXVI CICLO

Lighting the Path: Optical Trapping in Active Matter and Beyond

David Bronte Ciriza

Supervisors:
Dr. Onofrio M. Maragò
Dr. Maria Antonia Iatì
Prof. Rosalba Saija

Co-Supervisor:
Prof. Philip H. Jones

PhD course coordinator:
Prof. Vincenza Crupi

ACADEMIC YEAR 2022-2023

Para papá, mamá, Asier y Leire, por dármelo todo.

Acknowledgements

While I cherish the memories of numerous moments that have shaped my journey, this thesis too has been molded by the significant and unique contributions of many individuals, each propelling this work forward in their distinct and invaluable ways.

Immense appreciation fills my heart for the NanoSoft Lab group, who welcomed me into their beautiful scientific family. Onofrio and Antonella, your guidance, support, and opened doors were fundamental in this journey. Pietro, your scientific passion has been truly inspiring. Maria Grazia, your readiness to help and our morning conversations have been a source of great support and joy. Nino, your enthusiasm, and shared moments on the other side of the strait will always be remembered. A big thank you to Alessandro for the warmth welcome and shared enjoyment of sports, to Sonia for the shared concerns and laughter, to Donatella for your help, and to Rosalba for your support maneuvering through university bureaucracy. Moreover, I cannot thank everyone at CNR-IPCF Messina enough - the researchers, administration, cleaning staff, and door personnel. You've all made my time here truly special; you are a wonderful team to be part of.

A big feeling of gratitude also goes to the research teams that, even though far from Messina, played a crucial role in my research. Big thanks to Giovanni for embracing me into the world of optical forces and Artificial Intelligence in Gothenburg, to Lucio for the open doors in Zurich that enabled me to dive into microparticle synthesis. A heartfelt thank you to Giorgio and Phil for welcoming me in London, where we investigated the intriguing dance of particles with light. Science is a collective effort, and this thesis would not have been possible without those with whom I've collaborated closely: Agnese, for navigating through geometrical optics calculations; Antonio, for optical forces theory; Luca and Falko, for engaging micromotor discussions; Carlijn, in particle synthesis; Riccardo, in confronting red blood cell trapping; and Antonio Ciarlo and Martin, for exploring the AI landscape in optical forces. A warm acknowledgment also extends to my fellow early-stage researchers in the ITN ActiveMatter and in the University of Messina—sharing this journey with you has been not only insightful but also a genuine joy.

Per i miei amici messinesi posso solo dire grazie ancora. Mi avete fatto sentire un po' siciliano anch'io. Pina e Antonio, senza tutte le conversazioni condivise, senza i buonissimi pranzi e senza di voi, questa tesi sarebbe stata molto più noiosa. Professori e ragazzi della Penny Wirton, siete una luce che illumina Messina! Una luce che mi ha riempito ogni giorno di speranza e che, se guardate bene, ancora risplende in diverse parti di questa tesi. Grazie Andrea e Valeria per avermi aperto le porte dell'insegnamento; è stato un piacere collaborare con voi. Studenti e studentesse del primo anno di data science, mi è piaciuto tantissimo aiutarvi con la fisica. Vedevo il mio riflesso di alcuni anni fa nei vostri occhi mentre guardavate le lezioni. Grazie per la vostra simpatia e gratitudine, vi auguro un futuro brillante. E a tutti gli amici con cui abbiamo condiviso pranzi, conversazioni, passegiate, escursioni, bagni al mare, grazie mille: voi siete la mia Messina. La Messina che amo e di cui sono orgoglioso!

A mi familia y amigos, me siento inmensamente afortunado de sentiros cerca y de que me hayáis acompañado en esta experiencia. El tiempo y la energía que ya no me consumirá la tesis quiero que sea para vosotros y vosotras, que la tesis es de luz, y sois gente luminosa. Las estrellas que me guían, los vientos que me empujan hacia adelante y las anclas que mantienen firme. Gracias.

Table of contents

List of figures

List of tables

Introduction

From the earliest observations of deflection of comet tails by sunlight in the 17th century to the sophisticated manipulation of microscopic entities using lasers in the 21st century, the interplay between light and matter has ceaselessly captivated and challenged humanity. The unique ability of light to interact with matter has illuminated pathways into the microworld, driving innovations in numerous fields of science. This thesis aims to offer an in-depth exploration of various aspects of optical forces, merging advanced computational tools with experimental novelties, all bound together by the central theme of manipulating the microscopic world using light.

In the initial chapter, we delve into the basics of optical trapping. Starting with its foundational theories, we gradually transition into the practical aspects of setting up and using optical tweezers. Additionally, I detail the wide-ranging applications of this tool, highlighting their significant contributions to fields such as biology, environmental science, and active matter.

In the succeeding chapter, we confront a challenge that has complicated optical forces research: the computationally demanding nature of force calculations, which results in significantly long computations. By weaving machine learning into the tapestry of conventional approaches, we can achieve calculations that combine both speed and precision. This innovation unlocks the doors to numerically probing complex systems, from ellipsoids in double traps to red blood cells and the environmentally harmful microplastics. As we wade through this chapter, it becomes evident that the confluence of optics (not only optical forces) and artificial intelligence is not just a marriage of convenience but a symbiotic fusion, signaling the dawn of an exciting chapter in this discipline.

In the third chapter, we maintain our focus on the microscale, but our subjects come from the vast reaches of space. Here, the focus is on using optical tweezers as a precise tool for examining cosmic dust. These tiny interstellar grains, spread throughout the cosmos, are more than just specks that complicate our space observations; they carry information about celestial evolution and processes. By probing and characterizing these particles, we underline the potential of optical tweezers in advancing our understanding of the universe and its mysteries.

In the fourth chapter, I introduce a microengine with full orbital motion control. At its heart is a Janus particle, intriguingly trapped not at the center of the beam, but at a precise distance where thermal forces pushing outward balance with the optical forces pulling inward. This equilibrium can be adjusted by varying the beam power. Adding another layer of complexity, when the system is exposed to circularly polarized light, the particle starts to rotate. Remarkably, this rotational motion can be halted or even reversed by simply shifting to linearly polarized light or using circularly polarized light in the opposing direction. This chapter unveils the vast potential of combining both optical and thermal effects.

In the concluding chapter, the emphasis is on how optical forces can move particles, not just confine them, within the domain of active matter. Shape-asymmetric particles exhibit an inherent ability to self-propel due to the momentum transfer via transverse optical forces. This unique propulsion mechanism is further enhanced when we introduce a light-absorbing coating, which instigates thermophoretic effects. These capped particles are propelled, charting their course along intricate pathways. The pathways are shaped by the interplay between deterministic optical forces and random Brownian motion, and are influenced by variables such as particle size and the distribution of light. A numerical model that closely aligns with our experimental findings offers further clarity. This chapter doesn't merely spotlight a novel application of optical forces; the implications of this study extend beyond targeted applications, shedding light on broader phenomena such as bacterial motion and animal migration, and enriching our understanding of determinants of motion across various scientific domains.

Every chapter highlights the unique powers of optical forces, and together they provide a detailed understanding of how we use light to work with and understand the tiny world around us. As you navigate this thesis, I extend an invitation: marvel at the versatility of light and envisage a future where its interplay with matter continues to unlock new scientific and technological horizons.

Chapter 1

Principles of optical trapping

The interaction between light and matter has fascinated scientists for centuries. As far back as 1619, Johannes Kepler observed the deflection of comet tails by the rays of the sun, a groundbreaking recognition of light's ability to exert a force on matter. With the advent of lasers in 1970, it became possible to concentrate enough optical power to significantly affect the motion of microscopic particles, leading to Arthur Ashkin's invention of optical tweezers. By employing a tightly focused laser beam, optical tweezers apply forces at the micro scale and now contribute to fields like biology, physics, or environmental sciences. In the image, comet Hale-Bopp had a notable blue ion tail and white dust tail due to the solar wind and to the Sun's light forces respectively. Credits: A. Dimai and D. Ghirardo, Col Druscie Observatory, Associazione Astronomica Cortina.

1.1 Theory of optical trapping

The radiation force exerted by light on matter stems from the conservation of electromagnetic momentum during the scattering process. Historically, optical forces have been understood within strong approximations based on limiting size regimes. The parameter used to determine the range of validity of these approximations is the size parameter

$$\xi = k_{\mathrm{m}} a = \frac{2\pi n_{\mathrm{m}}}{\lambda_0} a \,, \tag{1.1}$$

where k_{m} is the light wavenumber in the surrounding medium, a is the characteristic dimension of the particle (in the case of a sphere corresponds to its radius), λ_0 is the wavelength in vacuum, and n_{m} is the refractive index of the surrounding medium. When $k_{\mathrm{m}}a \gg 1$, the *geometrical optics approximation* [1, 2] is used to calculate the optical forces. In the opposite case, when $k_{\mathrm{m}}a \ll 1$, the *Rayleigh approximation* can be applied [3]. This approximation treats the particle as a dipole and assumes that the electromagnetic fields within the particle are homogeneous. This imposes one further condition on the size parameter, i.e.,

$$\left| \frac{n_{\mathrm{p}}}{n_{\mathrm{m}}} \right| k_{\mathrm{m}} a \ll 1 \tag{1.2}$$

where n_{p} is the refractive index of the particle. Finally, for intermediate size parameters, the accurate calculation of optical forces necessitates a comprehensive consideration of the full electromagnetic theory governing the light-matter interaction in the *intermediate regime* [4].

In optical trapping, the parameter that quantifies the robustness of the trap is the ’trap stiffness.’ This parameter elucidates the restoring force exerted on an optically confined particle when it displaces from the equilibrium position. Notably, the trap stiffness exhibits a dependency on the size parameter of the trapped particle. Fig. 1.1 delineates this relationship, presenting trap stiffness across three distinct regimes. An overview of the three distinct regimes, including the full electromagnetic theory for the intermediate stage, is provided in the following subsections. Furthermore, in the subsequent chapter, we will explore the application of machine learning to address certain limitations of these approaches and further refine optical force calculations.

1.1.1 Geometrical optics approximation

In the *geometrical optics approximation*, the optical field may be described as a collection of N rays, each of which is associated with a fraction, P_{i}, of the incident power $P = \sum_{\mathrm{i}} P_{\mathrm{i}}$. Each ray carries a linear momentum $n_{\mathrm{m}} P_{\mathrm{i}}/c$ through a fixed plane in unit time.

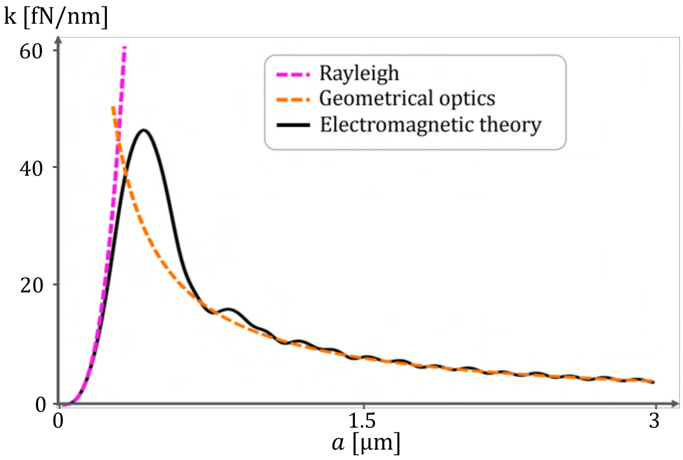

Fig. 1.1 Transverse trap stiffness calculated for the different regimes. The solid line represents the exact electromagnetic calculation while the dashed lines represent the Rayleigh (pink) and Geometrical optics (orange) approximations.

To understand the forces that act on a trapped microscopic particle, we start with a minimalistic model: the force due to a single ray $\mathbf{r}_\mathrm{i}$ hitting a dielectric sphere at an angle of incidence θ_i (Fig. 1.2). When $\mathbf{r}_\mathrm{i}$ strikes the sphere, a small part of the power is diverted into the reflected ray $\mathbf{r}_{\mathrm{r},0}$, while most of the power is carried by the transmitted ray $\mathbf{r}_{\mathrm{t},0}$. This transmitted ray $\mathbf{r}_{\mathrm{t},0}$ crosses the sphere until it reaches the next surface, where again it is largely transmitted outside the sphere into the ray $\mathbf{r}_{\mathrm{t},1}$, while a further small amount is reflected inside the sphere into the ray $\mathbf{r}_{\mathrm{r},1}$. This process continues until all light has escaped from the sphere. At each scattering event, the change in momentum of the ray causes a reaction force on the center of mass of the particle. By considering these multiple reflection and refraction events the optical force can be calculated directly [2] as:

$$\mathbf{F}_\mathrm{ray} = \frac{n_\mathrm{m} P_\mathrm{i}}{c}\hat{\mathbf{r}}_\mathrm{i} - \frac{n_\mathrm{m} P_\mathrm{r}}{c}\hat{\mathbf{r}}_{\mathrm{r},0} - \sum_{j=1}^{+\infty} \frac{n_\mathrm{m} P_{\mathrm{t},j}}{c}\hat{\mathbf{r}}_{\mathrm{t},j}\,, \tag{1.3}$$

where $\hat{\mathbf{r}}_\mathrm{i}$, $\hat{\mathbf{r}}_{\mathrm{r},j}$ and $\hat{\mathbf{r}}_{\mathrm{t},j}$ are unit vectors representing the direction of the incident ray and the j^th reflected and transmitted rays, respectively, calculated using Fresnel's reflection and transmission coefficients. Generally, most of the momentum transferred from the ray to the particle is due to only the first two scattering events, especially for small angle of incidence.

The force $\mathbf{F}_\mathrm{ray}$ in Eq. (1.3) has components only in the plane of incidence (Fig. 1.2) and can be split in two perpendicular components. The component in the direction of the incoming ray $\hat{\mathbf{r}}_\mathrm{i}$ represents the scattering force, $\mathbf{F}_{\mathrm{ray,s}}$, that pushes the particle in the direction of the incoming ray ($\hat{\mathbf{r}}_\mathrm{i}$). The component perpendicular to the incoming ray is the gradient force, $\mathbf{F}_{\mathrm{ray,g}}$, that pulls the particle in a direction perpendicular to that of the incoming ray

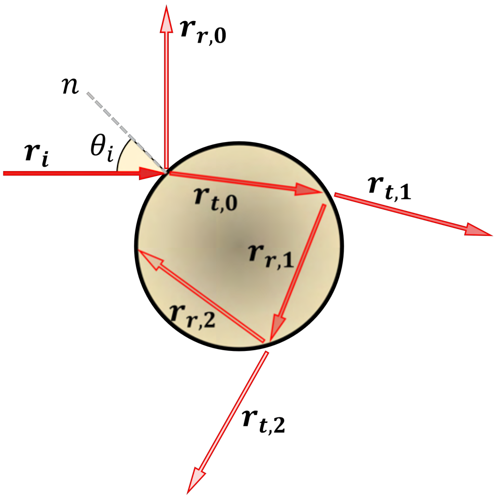

Fig. 1.2 Multiple scattering of a light ray impinging on a sphere in the incident plane. All the reflected and transmitted rays, as well as the optical force acting on the sphere lie in the plane of incidence.

($\hat{\mathbf{r}}_\perp$). Studying the dependence of the trapping efficiency of a ray on the angle of incidence, it is observed that independently of the size of the sphere, the maximum trapping efficiencies are obtained for large angles of incidence ($\approx 80°$) [1].

Even though so far we have explained the situation for the one-ray case, to model an optical trap we must not only consider a single incident ray but all the rays constituting a highly-focused laser beam, that is a set of many rays that converge at a very large angle. This means that the total force acting on the particle is a cumulative effect, derived from the individual contributions of each ray that forms the beam. In a single-beam optical trap, these focused rays generate a restoring force that is proportional to the particle's displacement from an equilibrium position. This equilibrium typically resides close to the beam waist, resulting in an harmonic potential that seeks to keep the particle centered.

The study of more complex non-spherical geometries can also be tackled using a geometrical optics approach, provided that all the characteristic dimensions of the object under examination are substantially greater than the light wavelength. However, deviations from sphericity introduces two major variations.

First, with non-spherical objects, a significant torque may be induced, leading to the rotation of the object. This phenomenon is referred to as the windmill effect, drawing an analogy to the motion of a windmill where the flow of momentum due to the electromagnetic field serves as the "wind" [5]. The torque generated by a single ray can be computed by contrasting the angular momentum associated with the incoming ray against that of the outgoing rays. The overall torque exerted on the object is then derived from the vector sum of the individual torques for each ray.

Second, in the case of a spherical particle, the radiation pressure from a plane wave (a set of parallel rays) is uniformly directed along the propagation direction due to symmetry. However, for particles with anisotropic shapes, this is not the case. The radiation pressure introduces a transverse component, giving rise to what is known as the optical lift effect. This means that non-spherical particles can move transversely with respect to the incident light's propagation direction, a phenomenon that distinguishes them from their spherical counterparts [6–8].

1.1.2 Rayleigh approximation

The *Rayleigh approximation* is based on the assumption that a particle can be approximated as a small dipole and that the fields are homogeneous inside the particle. An incident electromagnetic field $\mathbf{E}_\mathrm{i}$ induces an electric dipole moment $\mathbf{p}$ that, for sufficiently small fields, can be expressed in terms of the particle polarizability as:

$$\mathbf{p} = \alpha_\mathrm{p}(\omega)\mathbf{E}_\mathrm{i} \ , \tag{1.4}$$

where α_p is the complex polarizability of the particle relative to the surrounding medium given by [9]

$$\alpha_\mathrm{p} = \frac{\alpha_\mathrm{CM}}{1 - i\alpha_{CM}k_\mathrm{m}^3/(6\pi\varepsilon_\mathrm{m})} \tag{1.5}$$

with α_CM the static Clausius-Mossotti polarizability, i.e.,

$$\alpha_\mathrm{CM} = 3V\varepsilon_\mathrm{m}\left(\frac{\varepsilon_\mathrm{p} - \varepsilon_\mathrm{m}}{\varepsilon_\mathrm{p} + 2\varepsilon_\mathrm{m}}\right) \ , \tag{1.6}$$

ε_m and ε_p are the permittivities of the medium and particle, respectively, and V is the particle volume. k_m is the light wavenumber of the surrounding medium. The complex polarisability α_p, which typically depends on the frequency of the electromagnetic field ω, has a real part, α_p' which represents the oscillation of the dipole in phase with the field, and an imaginary part α_p'' which represents its oscillation in phase quadrature. The polarizability in the dipole regime is also linked to the cross-sections. In fact, the light-particle interaction can be described in terms of extinction, σ_ext, scattering, σ_scat, and absorption, $\sigma_\mathrm{abs} = \sigma_\mathrm{ext} - \sigma_\mathrm{scat}$ cross sections. For a small particle we can write the extinction and scattering cross-sections as $\sigma_\mathrm{ext} = k_\mathrm{m}\mathrm{Im}\{\alpha_\mathrm{p}\}/\varepsilon_\mathrm{m}$ and $\sigma_\mathrm{scat} = \frac{k_\mathrm{m}^4}{6\pi\varepsilon_\mathrm{m}^2}|\alpha_\mathrm{p}|^2$ [10].

Thus, we can consider the time-averaged optical force experienced by a small particle when illuminated by a time-varying electromagnetic field [3, 11, 12]:

$$\mathbf{F}_{\mathrm{DA}} = \frac{1}{2}\mathrm{Re}\left\{\sum_i \alpha_{\mathrm{p}} E_i \nabla E_i^*\right\}. \tag{1.7}$$

where E_i are the electric field components. Starting from this expression, one can explicitly write the optical force in terms of extinction cross-section and particle's polarizability [3, 11–13]:

$$\mathbf{F}_{\mathrm{DA}} = \frac{1}{4}\alpha_{\mathrm{p}}'\nabla|E_{\mathrm{i}}|^2 + \frac{n_{\mathrm{m}}\sigma_{\mathrm{ext}}}{c}\mathbf{S}_{\mathrm{i}} - \frac{1}{2}n_{\mathrm{m}}\sigma_{\mathrm{ext}}c\nabla\times\mathbf{s}_{\mathrm{d}}\ , \tag{1.8}$$

where $\mathbf{S}_{\mathrm{i}}$ is the time-averaged Poynting vector of the incident electromagnetic field, and $\mathbf{s}_{\mathrm{d}}$ is the time-averaged spin density [14, 12].

The first term in Eq. (1.8) represents the gradient force and is responsible for particle confinement in optical tweezers. Particles with a positive α_{p}' will be attracted towards the high intensity region of the optical field while if α_{p}' is negative, particles will be repelled. As an example, for an incident laser beam with a typical Gaussian profile which propagates along the z axis, the trap stiffness in the polarisation plane κ_ρ and along the direction of propagation κ_z related to the gradient force are [15]:

$$\kappa_\rho = 2\frac{\alpha_{\mathrm{p}}'}{cn_{\mathrm{m}}}\frac{I_0}{w_0^2}\ , \qquad \kappa_z = 2\frac{\alpha_{\mathrm{p}}'}{cn_{\mathrm{m}}}\frac{I_0}{z_0^2}. \tag{1.9}$$

where I_0 is the maximum intensity at the center of the beam, w_0 is the Gaussian beam waist, and z_0 is the beam Rayleigh range.

The second term in Eq. (1.8) corresponds to the scattering force, which is responsible for the radiation pressure and directed along the propagation direction of the laser. The last term in Eq. (1.8) is a spin-dependant force [13]. This term can be generated by polarisation gradients in the electromagnetic field but for optical trapping it typically becomes insignificant in comparison to the other terms. However, it plays a more significant role when trapping with beams of higher order with inhomogeneous polarisation patterns such us cylindrical vector beams [16] or superposition of Hermite-Gauss beams [17] and can be observed when trapping particles in vacuum [18].

1.1.3 Electromagnetic theory

The *intermediate regime* is characterised by a dimension of the particle that is comparable to the optical wavelength, that is by a size parameter close to 1. In this regime the *dipole* and *geometrical optics approximations* are no longer valid and a full modelling of the light-particle interaction is required, see Fig 1.1 for a comparison among the different approaches as a function of the particle size. In this regime, it is possible to derive $\mathbf{F}_{\mathrm{rad}}$ and $\mathbf{T}_{\mathrm{rad}}$ using the conservation of linear and angular momentum. The time-averaged force and torque exerted by monochromatic light on a particle are [19–21]:

$$\mathbf{F}_{\mathrm{rad}} = \int_S \overline{\mathsf{T}}_{\mathrm{M}} \cdot \hat{\mathbf{n}} dS\ , \quad \mathbf{T}_{\mathrm{rad}} = -\int_S \left(\overline{\mathsf{T}}_{\mathrm{M}} \times \mathbf{r}\right) \cdot \hat{\mathbf{n}} dS \qquad (1.10)$$

where the integration is carried out over a surface S surrounding the particle. The vector $\hat{\mathbf{n}}$ is the outward unit vector normal to the S, $\mathbf{r}$ is the position vector, and $\overline{\mathsf{T}}_{\mathrm{M}}$ is the time-averaged Maxwell stress tensor that describes the mechanical interaction of light and matter [22]. The general expression of $\overline{T}_{\mathrm{M}}$ in the Minkowski form [4] can be simplified when considering harmonic fields at angular frequency ω in a homogeneous, linear, and non-dispersive medium. In fact, writing the real physical fields, e.g.,$\mathbf{E}(\mathbf{r},t) = \mathrm{Re}\left\{\mathbf{E}(\mathbf{r})e^{-i\omega t}\right\}$, in terms of the complex amplitudes, e.g., $\mathbf{E} = \mathbf{E}(\mathbf{r})$, the averaged Maxwell stress tensor simplifies as [4]:

$$\overline{\mathsf{T}}_{\mathrm{M}} = \frac{1}{2}\varepsilon_{\mathrm{m}}\mathrm{Re}\left[\mathbf{E}_{\mathrm{t}} \otimes \mathbf{E}_{\mathrm{t}}^{*} + \frac{c^2}{n_{\mathrm{m}}^2}\mathbf{B}_{\mathrm{t}} \otimes \mathbf{B}_{\mathrm{t}}^{*} - \frac{1}{2}\left(|\mathbf{E}_{\mathrm{t}}|^2 + \frac{c^2}{n_{\mathrm{m}}^2}|\mathbf{B}_{\mathrm{t}}|^2\right)\mathsf{I}\right]\ , \qquad (1.11)$$

where $\otimes$ represents the dyadic (outer) product, I is the dydaic unit, and the fields $\mathbf{E}_{\mathrm{t}} = \mathbf{E}_{\mathrm{i}} + \mathbf{E}_{\mathrm{s}}$ and $\mathbf{B}_{\mathrm{t}} = \mathbf{B}_{\mathrm{i}} + \mathbf{B}_{\mathrm{s}}$ are the total electric and magnetic fields resulting from the superposition of the incident $(\mathbf{E}_{\mathrm{i}}, \mathbf{B}_{\mathrm{i}})$ and scattered $(\mathbf{E}_{\mathrm{s}}, \mathbf{B}_{\mathrm{s}})$ fields.

Several techniques have been proposed for computing electromagnetic scattering by non spherical particles and there is no single universal method that provides the best results in all situations. Depending on the specific parameters, different techniques may prove to be the most appropriate in terms of efficiency, accuracy and applicability [23]. Some of the common methods for the modeling of optical trapping of irregular shaped particles in the *intermediate regime* are discrete dipole approximation [24], finite-difference time-domain [25] and T-matrix [26].

Discrete dipole approximation is a finite element method in which a particle is split into a series of dipoles. Each of these dipoles interacts with the incident wave and with the re-radiated waves by all the other dipoles. The finite-difference time-domain method instead, is based on the numerical integration of the Maxwell equations in the time domain. The fields are sampled at discrete times and positions and, therefore, do not assume a harmonic time-dependence. Differently, the T-matrix method provides a compact formalism based on the multipole expansion of the fields. The transformation properties under rotation and translation of the T-matrix make possible to apply several simplifications in the force calculations since the T-matrix needs to be computed only once for a given orientation of the scatterer, making this approach the fastest one. On the other hand, even though discrete dipole approximation and the finite-difference time-domain method can be more computationally demanding, they can be slightly more versatile as they can be applied to particles of any shape and composition and to any light field configuration. All these methods have been used successfully for modelling optical trapping [27–29].

1.2 Experimental setups

In its simplest form, an optical tweezers is created by focusing a laser beam to a small spot using a high-numerical-aperture objective lens. This lens serves a dual purpose: concentrating the trapping light and imaging the trapped object. Optical tweezers typically require only a few milliwatts of optical power, minimizing the risk of damaging the sample.

Although the principle of optical trapping involves a relatively simple setup, researchers have developed more complex experimental arrangements for novel and challenging experiments. Examples include holographic optical tweezers, which use a spatial light modulator (SLM) to create customized optical potentials; time-sharing optical tweezers that employ an acousto-optic deflector (AOD) for fast beam manipulation and the creation of different effective optical traps; Raman tweezers coupled with an interferometer to obtain chemical information about the composition of the trapped sample, and interferometric optical tweezers capable of generating large-scale optical potentials. Detailed instructions for building advanced optical tweezers setups are available in [30, 4]. For the experiments presented in this thesis, we utilized three different setups: Standard optical tweezers with a quadrant photodiode (QPD), Raman Tweezers, and Speckle Tweezers, see Fig. 1.3.

In the following, we briefly review the main building blocks in an optical tweezers systems.

Microscopes: When setting up an optical tweezers system, a convenient option is to use a conventional commercial light microscope. These microscopes can be adapted with a dichroic mirror placed before the objective lens, which deflects the trapping laser beam into the lens while allowing the transmission of illumination light to a camera for sample imaging. While commercial microscopes are user-friendly and optimized to minimize aberrations in sample images, they offer limited customization possibilities and come with two main limitations: Their optics are typically optimized for visible light, which could cause issues when using infrared lasers, and the mechanical stability of commercial microscopes might not meet the requirements for highly sensitive nanometer-scale experiments.

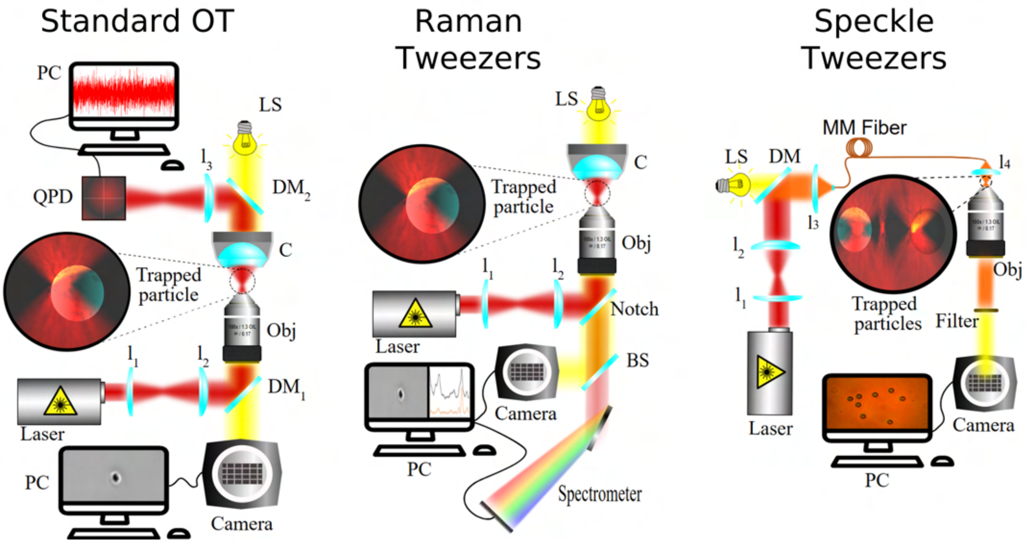

Fig. 1.3 Schematic of different optical tweezers setups. The standard optical tweezers are based on a highly focused beam and the position of the particle can be tracked with the camera or with the quadrant photo diode (QPD). Raman tweezers couple a spectrometer to the backscattered light in order to obtain chemical information from the trapped samples. Speckle tweezers use a multimode (MM) fiber to generate a complex interference pattern (speckle) that allows to trap particles at different positions. In the schematics, the light that traps the particles comes from the laser while the light source (LS) is used for illumination. In the inverted microscope setups (Standard and Raman tweezers) the light from the LS goes through the condenser. The lenses (l), dichroic mirrors (DM) and multimode (MM) fiber help us to shape and manipulate the laser beam while the quadrant photodiode (QPD), the camera and the spectrometer allow us to obtain information from the trapped sample.

As an increasingly popular alternative, homemade microscopes can be constructed using standard optomechanical components. Despite the challenges involved in their design and construction, these custom microscopes offer several advantages. They provide straightforward access to all parts and can achieve exceptional mechanical stability through careful material selection and design. Furthermore, homemade microscopes often prove more cost-effective compared to their commercial counterparts.

Laser sources: The quality of the laser is a critical factor in achieving the tightly focused spot necessary for optical trapping (the spot needs to be as close as possible to the diffraction limit). Furthermore, good pointing stability is essential for maintaining a steady position of the optical trap, while low power fluctuations are crucial for preserving a consistent strength in the trap. These considerations extend to the choice of laser wavelength as well. For those working with biological samples, care must be taken to select a wavelength that avoids photodamage; this often leads researchers to prefer lasers within the first or second biological windows. If working with metal particles, awareness of potential changes introduced by plasmonic effects becomes vital. Balancing these factors ensures that the laser functionality aligns with the requirements of the specific application, be it in biological or material contexts.

Particle tracking: Accurate particle tracking is essential for most measurements performed with optical tweezers. There are two primary methods for measuring the particle position: The first approach involves imaging the trapped particle using a CCD or CMOS camera, while the second method utilizes detectors capable of measuring the spatial distribution of intensity in the interference pattern formed between the light scattered by the trapped particle and the unscattered laser light.

Since a typical optical tweezers setup comes already equipped with a digital camera, the most straightforward way to measure the motion of a Brownian particle is by recording a video of its position and then tracking it frame by frame. This widely used technique, known as digital video microscopy [31, 32], finds widespread applications, particularly in colloidal studies and systems with multiple particles. The applicability of the technique has been further broadened with the integration of machine learning-based tools, which enhance particle tracking capabilities [33]. However, this method has its limitations, particularly in capturing rapid movements. The frame rate of the camera, which typically peaks at a few thousand frames per second, constrains its ability to document high-speed phenomena, underscoring the need for careful consideration in applications requiring the observation of quick motions.

An alternative to digital video microscopy involves using the interference pattern resulting from the interaction between the incoming and scattered fields [34]. By collecting this pattern with a condenser and recording the signals using a quadrant photodiode (QPD) at the condenser back-focal plane, it becomes possible to track the particle position based on the changes in the intensity distribution of the interference pattern. While this approach is not as straightforward as digital video microscopy and is limited to one particle, it comes with a faster acquisition frequency which can be critical to capture the fast dynamics of the trapped particle.

1.3 Calibration

Close to the equilibrium position, an optical tweezers system generates a three-dimensional potential well that can be approximated by a harmonic potential. In this context, we will introduce and examine three distinct methods—namely, *Power spectrum analysis*, *Autocorrelation* *function analysis* and *FORMA*—that can be employed to calibrate an optical trap utilizing experimental data. For simplicity, in this chapter we will focus on spherical particles and in situations where the friction coefficient γ is known. However, the presented methods can be expanded to non spherical particles [35–37] and to situations where γ is unknown [38, 39]. It is important to note that while in digital video microscopy the conversion from pixels to units of length can be straightforward upon a proper calibration, this is not necessarily the case for QPD signals where we need to derive the calibration factor. In these examples we solve the general case and we analyze measurements obtained with a QPD.

1.3.1 Power spectrum analysis

Power spectrum analysis is a commonly employed method for calibrating an optical trap, particularly for spherical particles [40]. In the overdamped regime, the motion of a trapped spherical particle can be described by the Langevin equations. If, for clarity, we consider only the x direction, we have:

$$\frac{dx(t)}{dt} + \frac{k_x}{\gamma} x(t) = \sqrt{2D} W_x(t) \tag{1.12}$$

Fourier transforming Eq. 1.12 and calculating the square modulus of both sides we obtain [4]:

$$P(f) = 2|\hat{X}(f)|^2 = \frac{D}{\pi^2 (f_c^2 + f^2)} \tag{1.13}$$

where the corner frequency is defined as:

$$f_c = \frac{k_x}{2\pi\gamma} \tag{1.14}$$

Eq. 1.13 is the *power spectral density* (PSD) of the Brownian fluctuations of the trapped particle. The fit with a Lorentzian curve provides both the corner frequency f_c and the diffusion coefficient D_{exp}. However, as the tracking signal is in Volt units, the experimentally obtained power spectrum is in $\mathrm{V}^2 \cdot \mathrm{s}$ units, so D_{exp} is related to the diffusion coefficient D in length (m) units by the calibration factor

$$\beta_x = \sqrt{\frac{D_{exp}}{D}} \tag{1.15}$$

which has V/m units. If the theoretical diffusion coefficient D is known, namely, if the radius of the bead and the viscosity of the medium (and, thus, its temperature) are known, by fitting the experimental power spectrum (which gives D_{exp}) the β_x calibration factor can be calculated. Moreover, by using the corner frequency also the trap spring constant is obtained. If this procedure is applied also to other directions (y and z), the full calibration of the trap is obtained [4, 40], see Fig. 1.4 (a-c).

1.3.2 Autocorrelation function analysis

Autocorrelation function analysis is an alternative approach for the calibration of optical tweezers. Besides, it has the advantage of being easily adaptable to the study of the complex dynamics of non-spherical particles [35, 37, 41]. Given a quantity A which is a function of the coordinates $\mathbf{r}^N$ and momenta $\mathbf{p}^N$ of N particles in a thermodynamic system, its autocorrelation function is a measure of how much A at time $(t+\tau)$ depends on the value it had at time t, that is

$$C_{AA}(\tau) = \langle A(t)A(t+\tau)\rangle \tag{1.16}$$

In case of optical trapping, we are interested in the autocorrelation function (ACF) of the particle position. In the following, we will restrict for simplicity to the x direction, but similar results can be obtained for y and z direction. The particle position autocorrelation function C_{xx} in the x direction is:

$$C_{xx}(\tau) = \langle x(t)x(t+\tau)\rangle \tag{1.17}$$

By using the overdamped Langevin equation, we find that

$$\langle x(t)x(t+\tau)\rangle = C_{xx}(0)e^{-\omega_x\tau} \tag{1.18}$$

where $\omega_x = \frac{k_x}{\gamma}$ is the ACF relaxation frequency and $C_{xx}(0) = \langle x^2(t)\rangle$ can be obtained by the equipartition theorem [4], that is

$$\frac{1}{2}k_x\langle x^2(t)\rangle = \frac{1}{2}k_BT \tag{1.19}$$

obtaining a final expression for the autocorrelation function as

$$C_{xx}(\tau) = \frac{k_BT}{k_x}e^{-\omega_x\tau} \tag{1.20}$$

By fitting the ACF with a single exponential decay we calculate the trap spring constant k_x. Moreover, as the detector provides voltage signals $V_x(t) = \beta_x x(t)$, we have to calculate the voltage/length conversion factor β_x:

$$C^V_{xx}(\tau) = \beta_x^2 C_{xx}(\tau) = \beta_x^2 \frac{k_B T}{k_x} e^{-\omega_x \tau} \tag{1.21}$$

and thus we obtain in V/m units:

$$\beta_x = \sqrt{\frac{C^V_{xx}(0) k_x}{k_B T}} \tag{1.22}$$

In the case of a spherical particle in 3D, all the formalism can be generalized to obtain the trap spring constants k_i and the corresponding conversion factors, provided that the drag coefficient γ is known, see Fig. 1.4 (d-f). It is important to note that the two approaches of the PSD and the ACF are equivalent, as the power spectral density of a signal is the Fourier transform of its autocorrelation function (autocorrelation theorem, [42]). Thus, the results obtained using the two approaches must be consistent. The choice of the calibration approach is made on the basis of the experimental situation. PSD approach is particularly useful when low frequency periodic noise, such as those due to electronic equipment or mechanical vibrations, must be removed, as they are easily recognized as δ peaks overlapping to the Brownian PSD. The ACF approach is more useful when the Brownian dynamics of non-spherical particles must be studied.

1.3.3 FORMA

Power spectrum and autocorrelation function analysis have traditionally been the most used methods to calibrate optical tweezers. However, they present some limitations as they require sampling at regular time intervals and the stiffness obtained depends on the choice of the parameters that are used for fitting the experimental data. FORMA [43] overcomes these constraints by exploiting the fact that in the proximity of an equilibrium position the force field can be linearized and then estimated using a maximum-likelihood estimator. Starting from the overdamped Langevin equation (Eq. 1.12), it is possible to discretize it and express the viscous friction force at a given n-th time interval as

$$f_n = \gamma \frac{\Delta x_n}{\Delta t_n} = -k x_n + \sigma w_n \tag{1.23}$$

where σ equals to $\sqrt{\frac{2D\gamma^2}{\Delta t_n}}$ and w_n is a random number normally distributed with zero mean and unit variance. Given that $\frac{\Delta x_n}{\Delta t_n}$ and x_n can be obtained from measurements as experimental data sets, and that Eq. 1.23 is written as a linear regression model, it is possible to calculate the parameters k and σ by means of maximum-likelihood estimators. In the case of the trap stiffness k, the estimator can be expressed as [43] (see Fig. 1.4 (g-i)):

$$k^* = \frac{\sum_n x_n f_n}{\sum_n x_n^2} \tag{1.24}$$

Eq. 1.24 can be solved very fast as its computational solution benefits from the existence of highly optimized linear algebra libraries. To provide a quantitative consistency check of the quality of the estimation, it is possible to compare the theoretical diffusion coefficient with the estimated one that can be computed from Eq. 1.23:

$$D^* = \frac{1}{N} \sum_n \frac{\Delta t_n}{2\gamma^2} (f_n + k^* x_n)^2 \tag{1.25}$$

FORMA, contrary to the power spectrum and autocorrelation methods, is also able to measure complex and non conservative optical fields by expanding the ideas introduced here. More information can be found on [43].

1.4 Applications

In this section, we provide an overview of recent developments in the applications of optical tweezers and optical forces. We focus on a selection of systems that are particularly relevant to this thesis, illustrating how optical trapping has emerged as a powerful tool to enhance the study and understanding of diverse systems such as red blood cells, cosmic dust, microplastics, and active particles.

1.4.1 Mechanical properties of red blood cells

Optical tweezers have found extensive use in the field of biological sciences, with one of their most successful applications being the exploration and measurement of the mechanical and elastic properties of red blood cells. While traditional blood tests typically emphasize the chemical attributes, changes in the mechanical properties of red blood cells have been associated with various pathological conditions [44, 45]. Very early in the history of optical tweezers Ashkin *et al.* showed that red blood cells (and many other biological species) could be trapped without optical damage using an infrared laser beam [46]. Subsequent experiments aimed at determining their mechanical properties have used the direct trapping method, or applied forces indirectly using optically trapped microbeads bound to the cell as 'handles'. Nowadays, optical tweezers have been used to test several diseases that affect red blood cells including malaria (*plasmodium falciparum*) [47, 48] and diabetic retinopathy [49]. Similarly, optical tweezers have been used to show the effects of drugs on the mechanical properties of cell membranes [50].

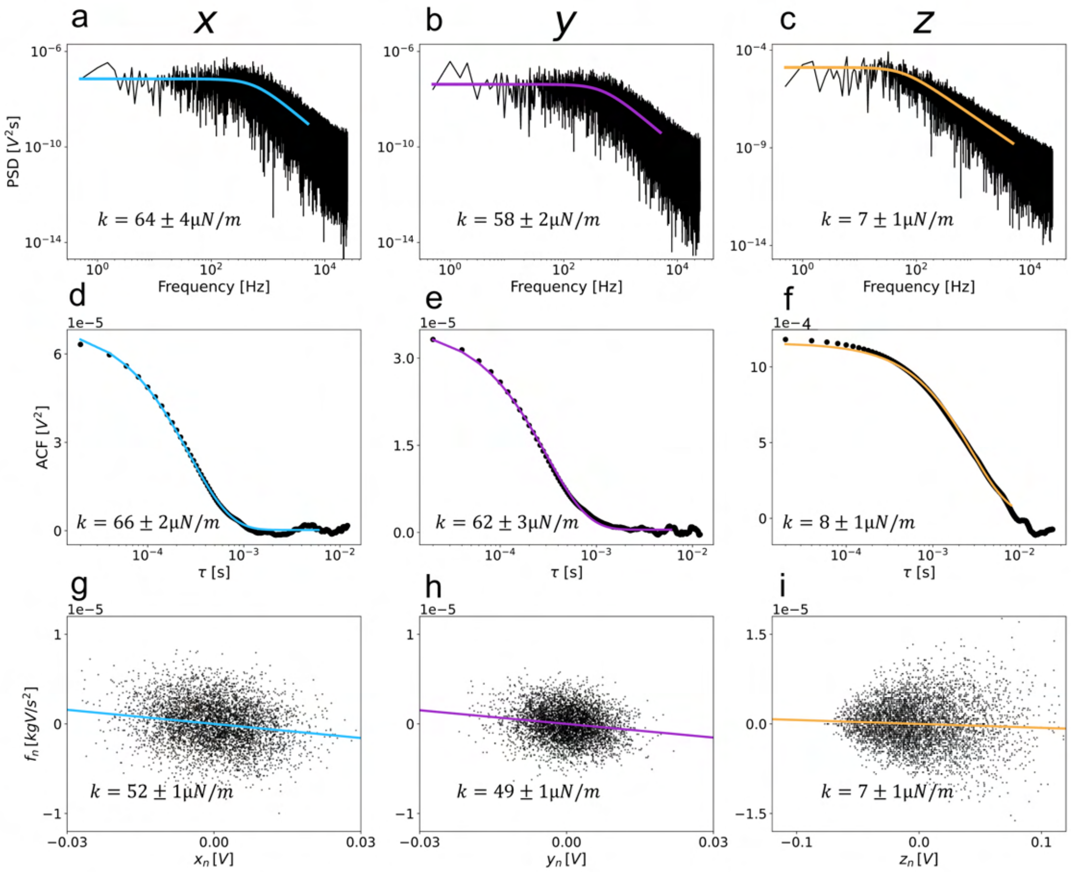

Fig. 1.4 Calibration methods applied to one measurement on the x, y and z directions. (a-c) Power spectrum analysis .(d-f) Autocorrelation method. (g-i) FORMA method. Even though the plots are for one single trajectory, the values of the trap stiffness k have been averaged over ten different measurements. The trap stiffness obtained through the three distinct methods shows strong agreement amongst them. As anticipated, the z component of the stiffness possesses the lowest value, indicating that the trap is weaker in that direction. The experimental data used for these calculations can be found at: github.com/brontecir/ExerciseOpticalTweezers/tree/main/ProblemForAM_Book/Exercise

1.4.2 Microplastics and cosmic dust

The ability of optical tweezers to isolate and control individual particles without physical contact is instrumental in ensuring that samples remain uncontaminated, a key requirement in the study of both microplastics [51] and cosmic dust [52].

In the realm of environmental science, microplastics have become a focal point due to their widespread presence in ecosystems and potential impact on human health [53]. Optical tweezers enable the isolation of individual micro and nano plastic particles [54, 55], allowing for contamination-free investigation. Such insights are fundamental in assessing the broader environmental and health implications of microplastics.

Concurrently, in astrophysics, optical tweezers offer a non-destructive, non-contact, and non-contaminating approach to the study of cosmic dust particles [29, 56]. Optical tweezers have the potential to trap dust particles in vacuum thus reproducing a microgravity environment and ensuring that the original characteristics of the dust particles are preserved. This allows for accurate analysis of physical properties, light scattering behavior, and composition, making optical tweezers an ideal tool for applications in curation facilities designed for the uncontaminated handling and preliminary characterization of extra-terrestrial samples returned by space probes.

The perspectives for optical trapping and manipulation of particles in space and on the surfaces of planetary bodies, might still need some key improvements in experimental setups. However, the current applications of optical tweezers in studying both microplastics and cosmic dust underscore their versatility and potential. By facilitating single particle, non-contact and contamination-free handling, optical tweezers continue to push the frontiers of research in both fields, contributing to a deeper understanding of our world and the universe beyond.

1.4.3 Active matter

Active matter refers to a diverse range of living and artificial systems capable of autonomously performing work, including cargo transport, movement, and the application of forces, by utilizing the energy present in their environment. These systems can exhibit remarkable self-organization and collective dynamics (school of fish, swarm of birds, motility induced phase separation), giving rise to complex emergent properties [57, 58]. In the context of optical forces, our focus lies on active matter at the microscale, encompassing entities like bacteria [59], sperm cells [60], and self-propelling colloids [61]. At this scale, Brownian fluctuations exert a significant influence on the motion of these systems, while inertia becomes negligible [62]. The control of active matter at the microscale poses challenges, and light-based methods offer distinctive advantages. Optical forces leverage high energy density, precise spatial and temporal control, the ability to tune different degrees of freedom independently, and the efficient transfer of both linear and angular momentum to effectively manipulate these microscale systems [63].

When light interacts with matter, both linear and angular momentum are transferred, resulting in the generation of forces and torques exerted on the material. In many instances, these forces and torques are employed to trap particles within a highly focused region, as seen in optical tweezers and in the previous sections [4]. However, there is a growing interest in utilizing these optical interactions to actively manipulate microscopic particles and induce controlled motion. Recent research has explored the momentum transfer to propel tiny vehicles by harnessing directional light scattering from plasmonic and dielectric surfaces incorporated into the particles [64–66]. This approach generates sufficient lateral force to drive the particles in a desired direction and the light-driven vehicles have been demonstrated as capable of micro manipulating colloidal particles and micro-organisms [64]. Moreover, in this thesis, we will explore how the shape of a particle can influence light scattering, thereby inducing an optical force that propels the particle along a specific direction. Furthermore, we explore the motion of these particles in complex optical landscapes (see Chapter 5).

While the focus of this thesis centers on exploring the momentum transfer between light and particles, it's important to acknowledge that light possesses other degrees of freedom that can be harnessed to control active matter, including light intensity, wavelength, and polarization. Among these, light intensity stands out as the most extensively used property for manipulating active matter. Some micro-organisms have evolved to sense and respond to light, adjusting their position and orientation to optimize photosynthesis efficiency [67]. Beyond naturally photoresponsive microorganisms, optogenetics has enabled the engineering of bacteria to modulate their mobility and population density in response to light [68], facilitating applications such as powering biohybrid microbots [69]. On the artificial side, a prominent example of micromotors lies in Janus particles [70]. These colloidal particles exhibit two different physico-chemical properties on their surface, this asymetry can be exploited to induce self-propulsion due to local thermodynamic gradients [71, 72]. Light intensity can be effectively utilized to induce such asymmetry and modulate temperature profiles (e.g., when one side is coated with a light-absorbing material) [73] or concentration profiles (e.g., by coating one side with a photocatalytic material) [74]. Combining different wavelengths further enhances the versatility of these particles, allowing for more complex behaviors. For instance, employing two hemispheres of a Janus particle with materials that catalyze hydrogen peroxide over distinct wavelength ranges [75]. Furthermore, the integration of optical forces and torques with light-induced thermophoretic effects adds complexity and richness to the particle’s dynamics, as will be explored in Chapter 4.. Polarization of light has also been proposed as a tool to increase the level of control over active matter [63].

Chapter 2

Machine learning enhanced optical force calculations

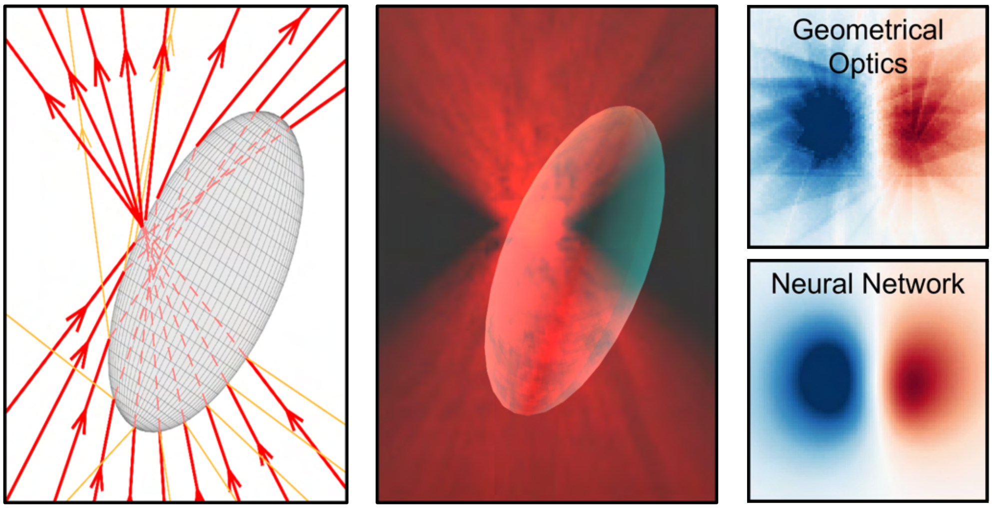

The calculation of optical forces traditionally faces a trade-off between speed and accuracy. In this chapter, we introduce machine learning to overcome this limitation, achieving both faster and more accurate results. We validate this approach in the geometrical optics regime using a spherical particle as an analytical ground truth. Thanks to the acceleration facilitated by neural networks, we are now able to study the dynamics of ellipsoidal particles and red blood cells in various optical trap configurations, a feat previously considered computationally unfeasible. Additionally, we explore the potential of machine learning with other approaches, such as T-matrix, with an emphasis on microplastics. The image showcases a comparison between the optical forces on a cylinder as calculated by traditional geometrical optics and those determined using neural networks, adapted from [76].

2.1 Machine learning for optical trapping

Several aspects of optical tweezers, which have been difficult to study theoretically due to computational costs or modeling complexity, are now being addressed with machine learning. This approach can enhance the calibration of optical tweezers [77] and improve particle tracking [33]. Moreover, recent advancements in machine learning are benefiting real-time control [78] and optimization in the design of optical tweezers setups [79]. In this chapter, our focus is on the application of machine learning specifically for optical force calculations.

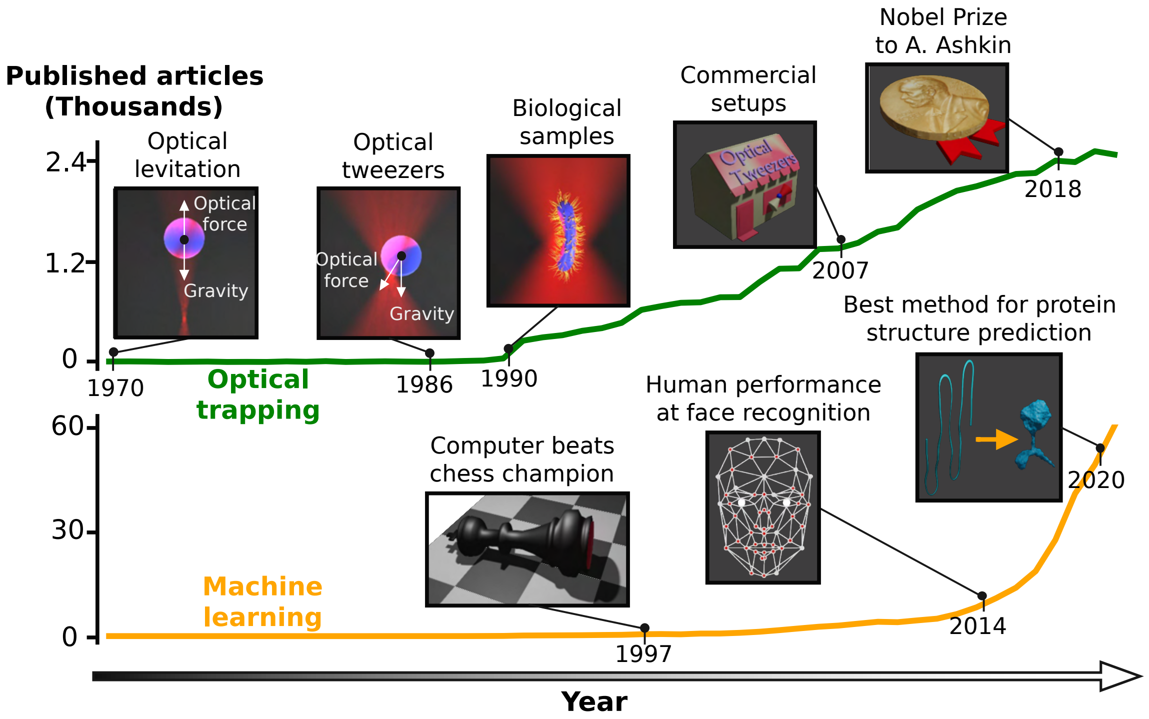

Fig. 2.1 Number of articles published per year that use “Optical trapping” (green line) or “Machine learning” (orange line) in their title, abstract, or keywords. Milestones in the development of both fields are marked and illustrated.

Due to its complexity, the calculation of the forces generated by optical tweezers often relies on approximations that depend on the size of the particle [4]. For particles larger than the light wavelength, such as cells [80, 49], micro-bubbles [81], micro-plastics [55], or metal-coated Janus micro-particles [82], these forces can be described using the geometrical optics (GO) approximation. In this approximation, the light field is represented as a collection of rays, and the momentum exchange between the rays and the particle is calculated via the laws of reflection and refraction [2], see section 1.1.1.

Even though GO force calculations are much faster than solving the full electromagnetic theory, they are still prohibitively slow for many applications. Often, multiple force calculations are required for a single numerical experiment studying the dynamics of a particle in an optical field. For example, to simulate the trajectory of a $2\,\mu$m ellipsoidal particle held by a double trap in water that is sufficiently long to estimate its Kramers' rates, one might require $\approx 10^7$ time steps and therefore force calculations. Since a single force calculation with sufficient accuracy (i.e., with a large enough number of rays) requires about $0.1\,$s, it would take several days to obtain one single meaningful trajectory. GO calculations can be sped up by decreasing the number of rays, but this compromises the accuracy.

There are alternatives to increase the speed of the calculation, but they come with their own limitations. The force generated by an optical trap can be approximated by a harmonic potential [83, 84]. However, while this is a good approximation for particles that remain close to the equilibrium point, there are plenty of situations where it is clearly insufficient, e.g., particles escaping an optical trap [85] or repelled by optical forces [86]. Another approach could be to avoid the sequential calculation imposed by the random Brownian motion by calculating the force in advance at different points in the parameter space and then interpolating the forces at intermediate points [87]. This improves the calculations for a sphere moving in 3 dimensions where a grid of 100^3 previously calculated points would suffice. However, the number of points that needs to be stored in memory grows exponentially with the number of degrees of freedom (DOF), and as we consider more complex shapes and configurations, the required grid points would easily surpass the current computer memory storage capabilities (e.g., the position, orientation, size and aspect ratio of an ellipsoid of revolution requires 7 DOF).

Recently, neural networks (NNs) have been demonstrated to be a promising approach to improve the speed of optical force calculation for spheres using the T-matrix method [88]. NNs are able to use data to adapt their solutions to specific problems [89]. These algorithms have proved to improve on the performance of conventional ones in tasks such as determining the scattering of nanoscopic particles [90], enhancing microscopy [91], tracking particles from digital video microscopy [92] or even epidemics containment [93].

In this chapter, we demonstrate that NNs can accelerate force calculations and, surprisingly, enhance the accuracy of GO. Initially, we validate this for a spherical particle with 3 Degrees of Freedom (DOF), corresponding to the particle's position, developing an analytical solution for optical force applied by a focused beam. We then extend the study to 9 DOF by encompassing relevant parameters for an optical tweezers experiment, such as refractive index, particle shape, position, and numerical aperture of the objective. We utilize NNs to accurately and efficiently map the dynamics of ellipsoidal particles in a double beam configuration, a task previously considered computationally unfeasible. Furthermore, we apply this strategy to train an NN for optical force calculations on red blood cells (RBC), enabling a detailed exploration of their Brownian dynamics in different trapping configurations. This is particularly promising as more efficient trapping reduces the risk of photo-damaging the cells. In the final section of the chapter, we employ NNs to enhance optical force calculations for micro and nanoplastics in the T-matrix regime. Although the use of optical tweezers for trapping microplastics is relatively new, the contactless study of single micro and nano particles makes this a promising tool. Rapid advancements in the theoretical understanding of optimal trapping configurations (wavelength, power, light pattern, etc.) for different microplastics are needed, and our work aims to contribute to this progress.

2.2 Modelling ellipsoid trapping

We employ NNs to calculate optical forces on ellipsoids in three different study cases. First, we compare the traditional GO calculation to the NNs approach in the simplest case of a sphere in an optical trap (3 DOF), where we have developed an analytical solution that we can employ as ground truth, based on Ashkin's original contribution but considering a continuous distribution of rays instead of a discrete set. Second, we expand this to the case of an ellipsoid (9 DOF), increasing the number of DOF to a value sufficient for most situations people encounter when working with optical tweezers. In these two study cases, we show how NNs are not only much faster but also more accurate than GO. Finally, we use this last NN to explore the dynamics of ellipsoids in a double beam optical tweezers, a problem that would have been computationally impossible to tackle with the conventional approach.

2.2.1 Sphere in a single trap

We start by studying the simplest case: we calculate the forces (F_x, F_y, F_z) applied by an optical tweezers on a sphere as a function of its position (x, y, z), see Fig. 2.2(a). We repeat this calculation with two different methods and compare them with the exact analytical calculation. First we employ the conventional GO approach considering 100 rays (Fig. 2.2(b)). Second, we use these data generated with GO to train a NN with 3 inputs, 3 outputs, and 5 hidden layers in between ($\approx 10^4$ trainable parameters, see Fig. 2.2(c)). The parameters of the system are typical of an optical tweezers experiment: $2\,\mu$m sphere with refractive index 1.5 in water, objective numerical aperture (NA) 1.3, and laser power 5 mW.

The NN provides more accurate results than GO for the same number of rays. Both GO and NN calculations show the expected equilibrium position close to the focus for both

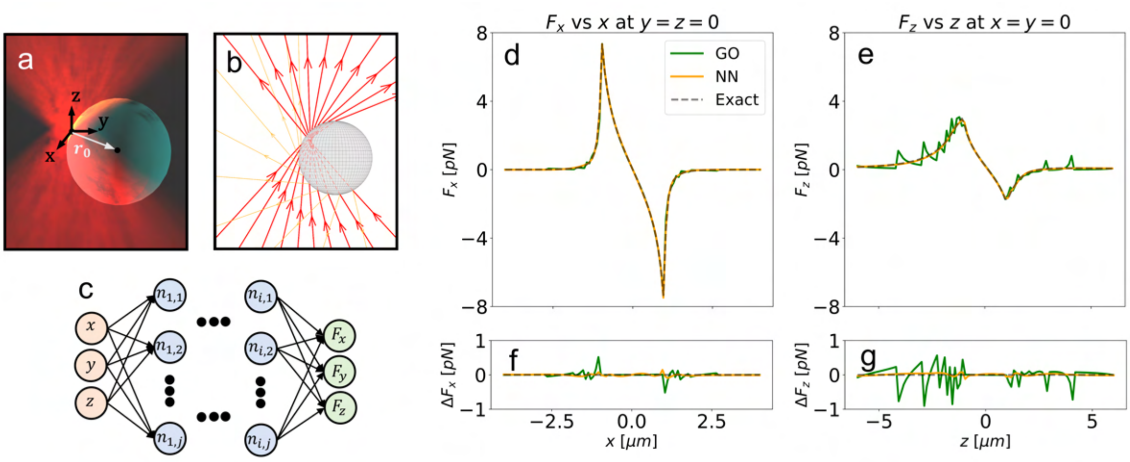

Fig. 2.2 Optical force calculations on a sphere. (a) 3D schematic of the sphere in an optical trap. (b) GO schematic of the rays reflected and transmitted by the sphere. (c) Architecture of a densely connected NN with an input layer (light red, particle position: x, y, z), an output layer (light green, optical force: F_x, F_y, F_z), and i hidden layers (light blue) in between. Each of the hidden layers has j neurons and all the neurons in each layer are connected to all the neurons in the previous and next layer. In the model trained with 100 rays, $i = 5$ and $j = 16$. (d,e) Optical force along the (d) x-axis and (e) z-axis calculated using GO (green solid line) and NN (orange solid line), as well as exact model (black dashed line) obtained using the analytical expression for spheres, see [76]. (f,g) The difference between the exact model and the GO (green lines) and NN (orange lines) calculations along the two axes shows that the NN is more accurate than GO, especially for F_z where the GO artifacts are more evident. Image adapted from [76]

transversal (x) and axial (z) directions, see Fig. 2.2(d,e). However, GO introduces artifacts due to the discretization of the continuous light beam into a finite number of rays, see Fig. 2.2(a,b). We manage to remove the artifacts by designing a NN that is complex enough to learn the smooth force profile, but not the superimposed fluctuating artifacts. This strategy allows the NN to achieve an accuracy higher than that of the training data, see Fig. 2.2(f,g).

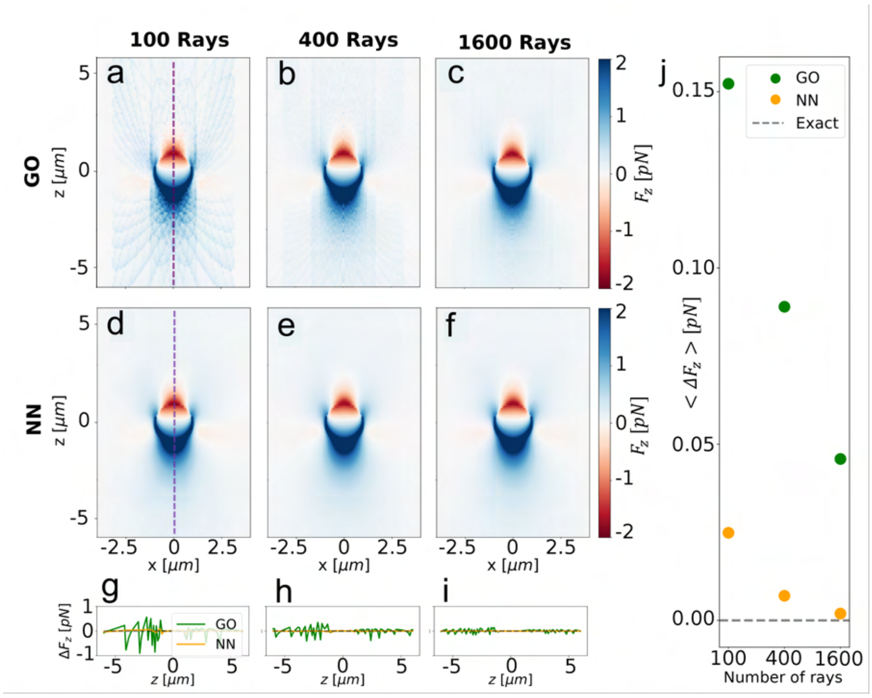

Fig. 2.3 Comparison of GO and NN for different numbers of rays. (a,b,c) GO calculation of F_z in the xz-plane. The number of rays considered for each calculation is 100, 400 and 1,600 respectively. (d,e,f) NN predictions when trained with data generated with 100, 400, and 1,600 rays, respectively. (g,h,i) Difference between GO and NN, and the exact model across the axis $y = x = 0$ (dashed region in (a) and (d)). (j) Average error of GO and NN with the exact model in the calculation of F_z across the axis $x = y = 0$ for 100, 400, and 1,600 rays. The NN is always more accurate than GO for an equivalent number of rays. Furthermore, even the NNs trained with the least amount of rays (100) are more accurate than GO with the most amount or rays (1,600). Image adapted from [76].

We can improve the accuracy of GO by increasing the number of rays. To illustrate this, we now focus on the axial force F_z (light going towards positive z) across the xz-plane. Fig. 2.3(a-c) shows the force calculation with GO for different number of rays. All the calculations retrieve the expected result of an equilibrium point close to the focus, positive force (blue) below the focus and negative force (red) over the focus. However, there are some artifacts that depend on the number of rays and that affect the accuracy of the calculation. Comparing the GO calculations with the analytical ground truth, see [76], we obtain the

Table 2.1 Calculations per second for the sphere with 3 DOF

	GO	NN (CPU)	NN (GPU)
100 rays	50.4 ± 0.5	407 ± 2	54100 ± 300
400 rays	32.1 ± 0.3	405 ± 2	54400 ± 200
1,600 rays	16.8 ± 0.1	532 ± 3	59700 ± 400

anticipated results: higher number of rays result in a lower error (see Fig. 2.3(g-i) where the solid green line corresponds to the error of GO against the exact analytical model). On the other hand, the NN (Fig. 2.3(d-f)) provides more accurate results than GO even when trained with data obtained with a lower number of rays (Fig. 2.3(g-i) where the solid orange line represents the error of the NN). Furthermore, compared with our exact solution across the z-axis, even the NN trained with 100 rays is more accurate than the GO considering 1,600 rays, see Fig. 2.3(j).

The NN is not only more accurate (Fig. 2.3), but also much faster than GO. GO reaches a calculation speed of around 50 calculations per second when considering 100 rays, and this speed decreases down to 17 calculations per second for 1,600 rays. The calculation speed by using our trained NN is between one and two orders of magnitude faster, see Table 2.1. The calculation speed of the NN does not depend on the number of rays used in the training set, but on the network architecture and on its number of trainable parameters. If we consider many particles, many beams, or we run many simulations at the same time, we can benefit from the straightforward implementation of the NN in the GPU to increase the speed by another two orders of magnitude.

2.2.2 Ellipsoid in a single trap

We now consider a more complex case with more DOF: We include different positions (x, y, z), orientations (θ and ϕ, corresponding to the angle of the major axis with the z direction and to the angle between the x direction and the projection of the major axis in the xy-plane), length of the major axis (c), aspect ratios (AR), refractive indices (n_p) of the particle, and different numerical apertures of the objective (NA), see Fig. 2.4(a). The forces and torques are computed using GO considering 400 and 1,600 rays, see Fig. 2.4(b). The data generated with GO is used to train a NN with 9 inputs (corresponding to the 9 DOF) and 6 outputs $(F_x, F_y, F_z, T_x, T_y, T_z)$, see Fig. 2.4(c). The architecture and the range of validity of the trained NN are defined in section 2.5. To account for the higher complexity of the problem, the training data is increased up to $2.5 \cdot 10^7$ points, a number larger than that for the sphere but much smaller than the prohibitive $\sim 100^9$ points that would have been required for the interpolation approach previously discussed. The NN trained with data generated with 1600 rays has more trainable parameters so it can benefit from the increased accuracy in the GO calculation.

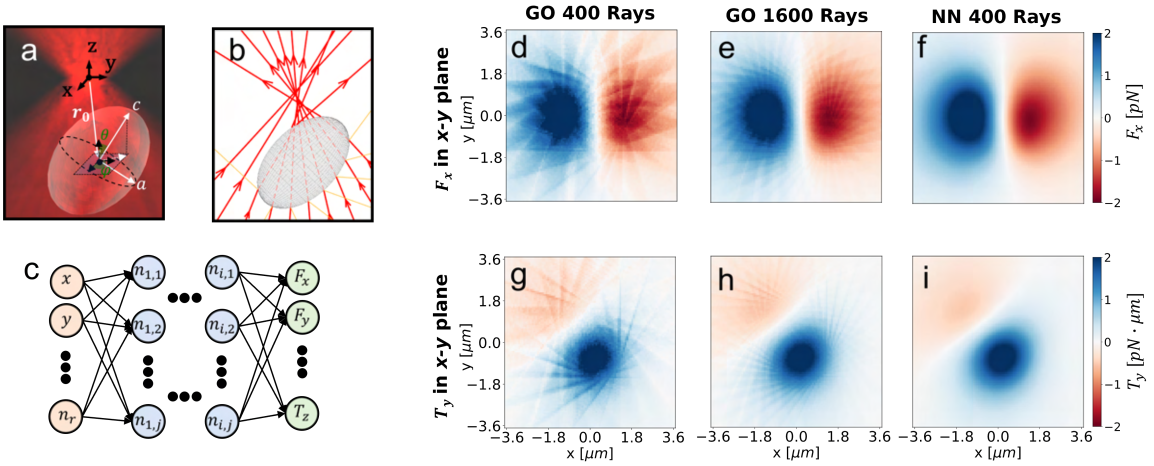

Fig. 2.4 Optical forces calculations for an ellipsoid. (a) 3D schematic of the ellipsoid in an optical trap. (b) GO schematic of the rays reflected and transmitted by an ellipsoid. (c) Architecture of a densely connected NN with an input layer (light red), an output layer (light green), and i hidden layers (light blue) in between. Each of the hidden layers has j neurons and all the neurons in each layer are connected to all the neurons in the previous and next layer. In both NNs $j = 384$ but the for the one trained with 400 rays $i = 5$ while in the one with 1,600 rays $i = 8$. (d-i) GO and NN calculations of F_x (d,e,f) and T_y (g,h,i) in the xy-plane at $z = -3.0\,\mu$m . The parameters chosen for the plots have been selected randomly across the space of parameters for which we have trained the NN. The major semiaxis (c) of the ellipsoid is 3.7 μm long, the aspect ratio (AR) is 1.5, and its orientation is determined by $\theta = 1.03$ rad and $\phi = 2.14$ rad. The refractive index (n_P) of the particle is 2.5 and the numerical aperture of the objective 1.2. Image adapted from [76].

Similarly to what we observed for the sphere, the NN improves the accuracy and drastically increases the speed when compared to GO. Even though in this situation we do have no ground truth to compare the accuracy of the different methods as there is no equivalent for ellipsoids of the analytical expression obtained in [76], we can compare the results with 400 rays against those with 1,600 rays. Differently from the case of the sphere, we can now explore all the 9 DOF. Selecting a random xy-plane in the 9 DOF space of parameters, the NN trained with 400 rays obtains the expected profile of the forces, see Fig. 2.4(d-f), and the torques, see Fig. 2.4(g-i), note that there is a non zero torque at $x = y = 0$ because the major axis of the ellipsoid is not aligned with the beam. The NN overcomes the accuracy of the training data even when trained with only 400 rays. Like in the previous example, the NN improves the calculation speed by 1-2 orders of magnitude when using the CPU and two more orders of magnitude when using the GPU (see Table 2.2).

Table 2.2 Calculations per second for the ellipsoid with 9 DOF

	GO	NN (CPU)	NN (GPU)
400 rays	9.62 ± 0.06	404 ± 1	50200 ± 300
1,600 rays	5.59 ± 0.02	297 ± 1	43400 ± 1400

2.2.3 Ellipsoid in a double trap

We can now explore the dynamics of an ellipsoid in a double trap by enhancing the calculation using the previously described NN. In a microscopic system, transitions between different equilibrium points can be induced by thermal fluctuations that allow the system to overcome the potential barrier. These transitions play a key role in electronics [94], physics [95] and biology [96], and optical tweezers have become an useful tool to study them [97–100]. While these previous studies have focused on spherical particles, considering different shapes could enrich the dynamics of these systems. However, these simulations often require a lot of repetitions of the force calculation, which with the conventional GO becomes prohibitively slow. In this situation, traditional approaches to speed up the calculation become unfeasible. We cannot consider the interpolation approach due to the high number of DOF of the system and we cannot use the harmonic approximation because of the broken assumption of small displacements around the equilibrium point. Therefore, we employ our trained NN to overcome these issues and achieve a fast and accurate calculation of optical forces. Since there are two focused beams, we first calculate the force and torque applied by each of them using the trained NN and then add both contributions to obtain the total effect on the particle. See section 2.5 for details about the simulation of the dynamics.

On the single-trajectory level, we observe the expected results for the dynamics of an ellipsoid in a double trap (Figs. 2.5(a,b)). The particle remains with its long axis aligned along the direction of the beam (color coding of Fig. 2.5(c)), which is typical for this kind of elongated structures [101, 102]. Apart from the focuses of the two traps, an additional equilibrium point emerges in between (densely explored region around $x = y = 0$ in Fig. 2.5(c)). Furthermore, when looking at the trajectories (Fig. 2.5(c-f)), the particle center remains confined around the origin of the x-axis (as expected), jumps between the two traps and an intermediate equilibrium point along the y-axis, and it is slightly displaced towards the positive values of z-axis due to the scattering force as it has already been observed experimentally [97].

Powered by the fast NN calculation, we can simulate many trajectories as the ones presented in Fig. 2.5 and explore the statistical properties of the dynamics. Exploring different configurations of parameters, we study how the equilibrium points and the Kramer's rate (ω_{K}) depend on the aspect ratio (AR) and on the distance between traps (d). We focus

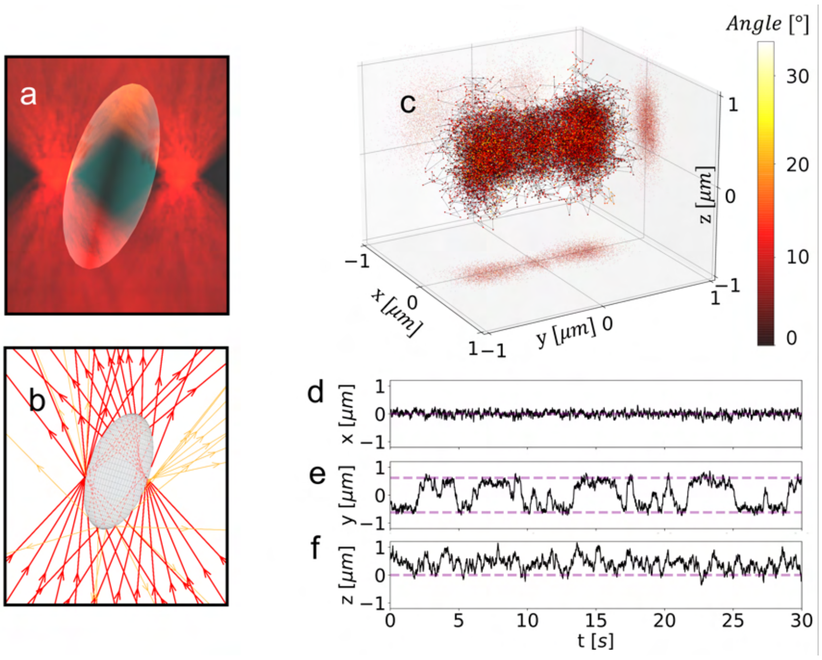

Fig. 2.5 Simulation of the dynamics of an ellipsoid in a double trap. (a) 3D schematic of an ellipsoid in a double trap (b) GO schematic of the rays reflected and transmitted by an ellipsoid in a double trap (c) Simulated 2-minute trajectory of an ellipsoid in a double trap. The color codes the orientation of the long axis of the ellipsoid with respect to the beam. The ellipsoid has a refractive index of 1.5, its major semiaxis is 4.2 μm, and its short semiaxis is 1.5 μm. The distance between the two beams is 1.24 μm, the intensity of each of them is 0.25 mW, and the *NA* of the objective focusing the light is 1.30. (d,e,f) show a 20-second trajectory of the center of mass along the x-, y-, and z-direction, respectively. The dashed purple lines correspond to the position of the focus of the beams in each of the axes. Image adapted from [76].

first on the dependence with d. Regarding the equilibrium points, in the state diagram we can distinguish three different regions, see Fig. 2.6(a). When the traps are close to each other they behave as a single one with the particle trapped in between. By increasing the separation between traps (d) the probability distribution starts widening until reaching a region with 3 equilibrium points. Separating even further the traps, the intermediate equilibrium position disappears and eventually the traps behave independently. The behaviour of the ellipsoids (Fig. 2.6(b)) is very similar to what was predicted and observed for spheres [98]. Regarding the dependence of ω_K with d, the transition rate reaches a maximum in the region where the system transits from three to two equilibrium points, see Fig. 2.6(c). We now focus on the dependence of the equilibrium points and ω_K on AR, i.e., understanding how the change in shape affects the dynamics of the particle. Fixing $d = 1.3\,\mu$m, the two farthest equilibrium points come closer to each other when increasing the length of the ellipsoid.

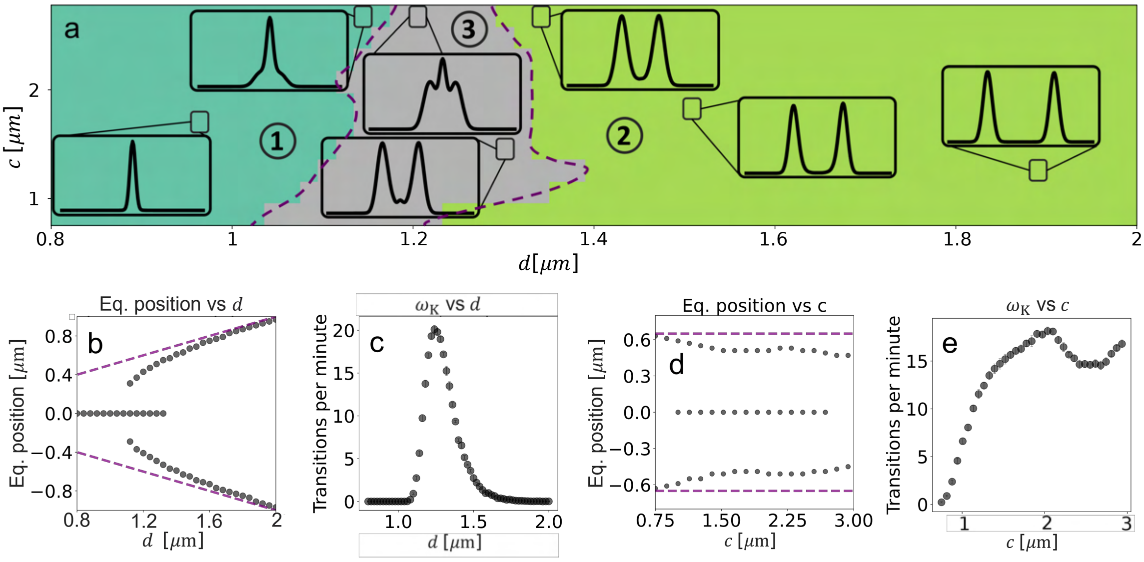

Fig. 2.6 Dynamics of an ellipsoid in a double trap changing its aspect ratio ($AR = c/a$) and the distance between traps (d). $NA = 1.3$, $n_P = 1.5$, $a = b = 0.75\,\mu$m are kept constant over the simulation, the particle is in water at 20°C and the intensity of each beam is 0.25 mW. Notice that while the length of the axes a and b is fixed, as we change c and the AR we also change the volume of the ellipsoid. (a) State diagram in the $AR - d$ parameter space. The parameter d samples the space from the situation where the two traps behave as one to the situation where the two traps are completely independent of each other. The AR ranges from 1 (a sphere) to 4 (ellipsoid). The three coloured regions correspond to 1 (blue), 3 (gray), and 2 (green) equilibrium points, the purple dashed line indicates the transitions between regions. The insets show the probability distribution averaged over 100 trajectories. In (b,c) we study the situation where AR is fixed to 2.8 and we change d while in (d,e) d is kept constant to 1.3 μm and we vary the AR. (b) Position of the equilibrium points vs d. The purple dashed line indicates the trap position. (c) Kramer's rate (ω_K) vs d. (d) Position of the equilibrium points vs AR. The purple dashed line indicates the trap position. (e) ω_K vs AR. Image adapted from [76].

Moreover, a third equilibrium point emerges for an intermediate region of lengths, see Fig. 2.6(d). Studying ω_K, it increases with the length of the ellipsoid until reaching a maximum and remaining approximately constant, see Fig. 2.6(e). It is known that the stiffness of the trap in the beam direction decreases with the length for elongated structures [103–105]. This decrease in the stiffness (see Supporting Information, “Trap stiffness dependence on the aspect ratio” in [76]) makes the particle more likely to reach the transition region as described for spheres in [97] and therefore the Kramer's rate increases.

It is worth noting that while a NN with many Degrees of Freedom (DOF) is valuable for approaching systems and studying their dependence on various parameters, the increase in generality can lead to a slight decrease in both accuracy and calculation speed (though it still outperforms GO), as well as requiring longer training (more data needed). In our study of the dynamics of the ellipsoid in a double trap, we did not employ the full potential of the NN as we kept certain input parameters of the NN constant (such as NA , a, and n_p). However, even in this non-optimal situation, we have demonstrated that it is possible to train a single NN that accounts for all the DOF of a typical OT experiment, enabling the study of new problems. If the reader wishes to explore specific situations where most of the DOF remain fixed, designing more tailored NNs might be beneficial. The trained NNs and a tutorial showing how to use them have been prepared and are available online: https://github.com/brontecir/Deep-Learning-for-Geometrical-Optics

2.3 Modelling red blood cell trapping

Red blood cells (RBCs), also known as erythrocytes, play a crucial role in delivering oxygen to tissues and organs in the human body. The elasticity of the RBC membrane is closely associated with the proper functioning of the microcirculation. When the membrane elasticity is compromised, it can lead to severe dysfunctions such as the blockage of capillaries, resulting in tissue necrosis, organ damage, and failure [106].

In recent decades, OT have emerged as a valuable tool in RBC research, allowing scientists to investigate the biochemical and biophysical properties of both healthy and unhealthy RBCs using single- or multi-beam OT techniques [107]. Since RBCs are significantly larger than the incident wavelength (typically infrared light around 1064 nm), the geometrical optics approximation effectively describes the interaction between the laser beam and the cell [108–110]. However, as in the case of the ellipsoids, this approximation poses a trade-off between calculation speed and accuracy.

In this section, we present a novel approach that utilizes a NN to enhance the speed and accuracy of optical force calculations for RBCs. This approach enables a more comprehensive exploration of the Brownian dynamics of RBCs, facilitating the study of various trapping configurations. By identifying more efficient trapping configurations, we can minimize the laser power required and, consequently, reduce the risk of photo damage to trapped cells—a critical concern when working with biological samples.

2.3.1 Single trap

To evaluate the effectiveness of our approach, we begin by testing the ability of the NN to predict the forces and torques acting on an RBC in a single beam OT (SBOT). We compare the NN predictions (trained with data generated using 4×10^2 rays) and the GO calculations considering 4 times more rays (1.6×10^3 rays) at 1×10^5 random positions and orientations. The 2D density plots shown in Fig. 2.7-c and -d illustrate the agreement between the NN and GO in predicting the optical forces (regression coefficient 0.998, $R^2 = 0.996$) and torques (regression coefficient 0.999, $R^2 = 0.996$), respectively. Although there is no ground truth for this situation, we can assess the accuracy of the NN by comparing the NN (trained with data generated with 4×10^2 rays) with the GO calculation (considering a greater number of rays). Fig. 2.2-e shows the normalised root mean squared error (NRMSE) between the predictions of the NN trained with 4×10^2 rays and the GO calculations with different numbers of rays (up to 5×10^3 rays). The NRMSE decreases as the number of rays increases. The forces and torques calculated with 5×10^3 rays result more similar to the NN output than to the forces obtained with a total of 4×10^2 rays, meaning that the NN is able to increase the accuracy of the force and torque prediction, even for an object with such a complex shape.

2.3.2 Double trap

Since the NN is trained for a SBOT, one may think it can only predict the optical forces and torques for a SBOT. However, similarly to what we did for the ellipsoid in the double beam configuration, the NN can be used multiple times to simulate multi-beam optical tweezers. In fact, the NN can predict the forces generated by a single beam on different locations on the cell, and the total force acting on the centre of mass of the cell may then be calculated as the vector sum of each contribution. The experimental implementation of a multi-beam OT setup presents greater challenges in the beam alignment, power balance and beam control compared to a single-beam configuration. However, recent advancements in the field of OT and beam shaping techniques have made it possible to realize the potential of multi-beam OT in experimental setups [112, 113, 4]. Here we consider a double-beam optical tweezers (DBOT) where the two beams geometric foci are positioned 5.06μm apart along the x-axis, similar to the experiments conducted by Agrawal et al. [49], Fig. 2.8(a). To the best of our knowledge, the cell configuration observed by Agrawal et al. is the only one observed experimentally when a DBOT is employed for trapping. Indeed, optical torques and forces are responsible to maintain the positional and orientational equilibrium of the cell. In fact, for any displacements from the equilibrium configuration restoring torques/forces act on the cell pushing it back to the equilibrium position and orientation.

Fig. 2.8(b-c) shows $T_\mathrm{x}(\alpha)$ and $F_\mathrm{x}(x)$ calculated with GO and predicted with the NN for a cell in its folded configuration (i.e., cell major axis parallel to the optical axis) trapped in a DBOT. In both cases, the NN predictions (solid line) agree well with the GO method (dots), demonstrating the possibility to use the NN for multi-beam optical traps. We therefore conclude that this approach can be extended to predict forces and torques generated by a

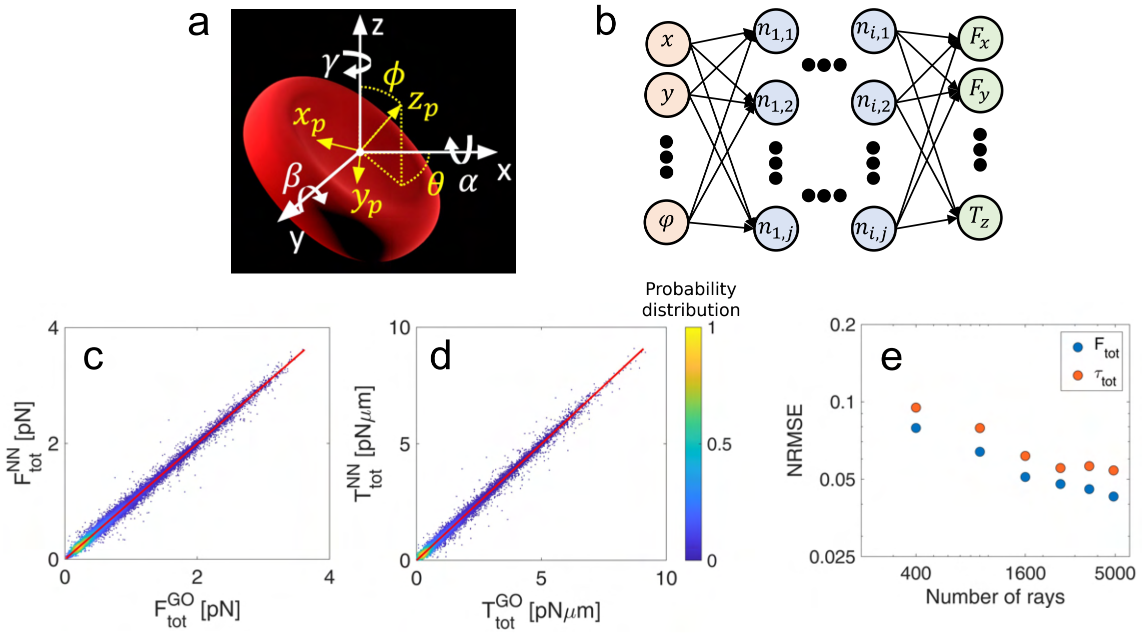

Fig. 2.7 Optical forces applied on a red blood cell by a single beam. a) Definition of particle (yellow) and laboratory (white) reference frames and rotation angles (α, β, γ) of the cell around the laboratory reference frame; b) schematic depiction of the neural network. The input layer contains six neurons describing the cell position and orientation, and the output layer has six neurons describing the components of force and torque acting on the cell. In between are seven hidden layers ($i = 7$), each of them with 256 neurons ($j = 256$). c-d) Density plots comparing the magnitude of the total force ($F^{\text{NN}}_{\text{tot}}$) and torque ($T^{\text{NN}}_{\text{tot}}$) predicted with NN with those calculated with the GO method ($F^{\text{GO}}_{\text{tot}}$) and ($T^{\text{GO}}_{\text{tot}}$). Regression lines are shown in red. e) Log-Log plot of the normalised root mean squared error (NRMSE) between $F^{\text{NN}}_{\text{tot}}$ and $F^{\text{GO}}_{\text{tot}}$, and $T^{\text{NN}}_{\text{tot}}$ and $T^{\text{GO}}_{\text{tot}}$ as a function of the number of rays used in the GO calculation. For each data point, the NN employed remains the same (trained with 4×10^2 rays). Image adapted from [111].

three- and four-beam OT, situations in which the GO calculation is considerably slower given the very large number of light rays required.

We now investigate the cell dynamics within a DBOT using both NN and GO to compute the optical forces. The simulation of the Brownian dynamics follows the strategy explained in the Methods section (Particle dynamics simulation) where now the force and torque considered is the sum of the contributions of each of the beams. Fig. 2.8(a)-(d) shows the probability distribution of the centre of mass of the cell for a total simulation time of 5s, while Fig. 2.8(e) shows the orientation of the cell with respect to the fixed reference frame as a function of the simulation time. It is important mentioning that in the current configuration a rotation around the y-axis (β) would be a rotation around the cell axis of symmetry and

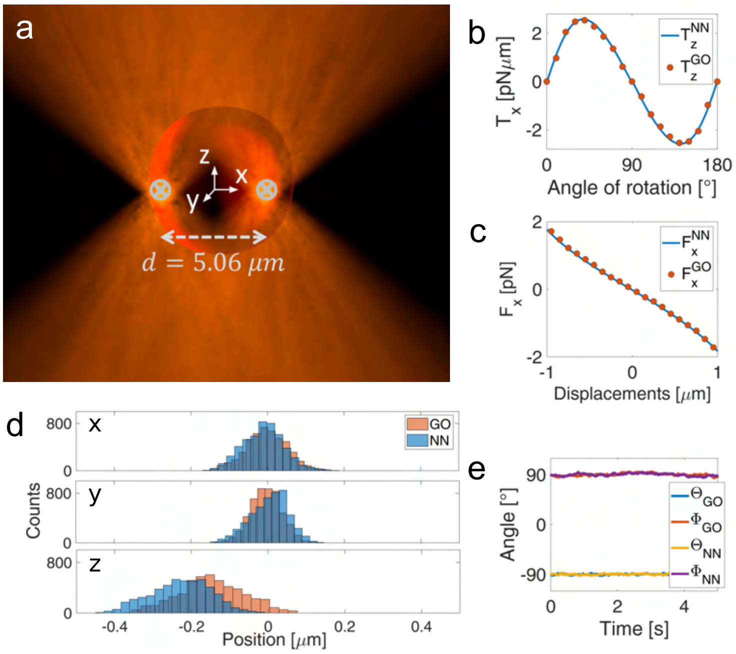

Fig. 2.8 Red blood cell trapped in a double beam configuration. a) Schematic depiction of an RBC trapped by a double-beam OT. b-c) Comparison between the GO calculation and the NN prediction for the b) torque-rotation curve for rotation around the x-axis and c) force-displacement curve along the x-direction. (d) Comparison of the probability distribution obtained with the GO calculation and with the NN prediction for a RBC in a DBOT. (e) Cell orientations in the numerical simulation for both GO and NN. Image adapted from [111].

therefore completely irrelevant. By extracting the average values for each degree of freedom, it is possible to compare the final equilibrium configuration obtained with the NN and with GO. Indeed, the average values obtained with the predictions of the NN match the ones obtained with GO methods and agree well with previously reported values [111], see Table 2.3.

Moreover, the biggest advantage of using the NN for numerical simulations is a consistent decrease in the simulation time required to achieve the same precision (the NN is two orders of magnitude faster). Since the NN shows a higher computational efficiency, hereafter, we make use of the NN prediction to simulate the Brownian dynamics of an optically trapped RBC.

We therefore move to extract quantitative information on the trap constants. Initially we analyse the hydrodynamics of the RBC, since non-spherical particle could have an intrinsic roto-translation coupling due to their peculiar shape [114]. In our case, the diffusion tensor **D** does not show any strong roto-translation coupling; therefore, we do not expect to find any strong correlation in the cell motion intrinsically due to the RBC hydrodynamic interactions.

Table 2.3 Equilibrium position and orientation for a RBC in a double-beam OT as found with GO and NN.

	GO	NN
$x_{2,eq}(\mu\text{m})$	0.01 ± 0.05	0.01 ± 0.05
$y_{2,eq}(\mu\text{m})$	0.00 ± 0.05	0.00 ± 0.04
$z_{2,eq}(\mu\text{m})$	-0.20 ± 0.08	-0.18 ± 0.08
$\phi_{2,eq}(^\circ)$	90.65 ± 2.11	90.27 ± 1.44
$\theta_{2,eq}(^\circ)$	-90.45 ± 1.06	-90.09 ± 0.92

Still, optically trapped non-spherical particles could show roto-translation coupling in their motion as previously observed by others. In this framework, the normalised auto-correlation function (ACF) has been successfully used to extract quantitative information about the trapping constants [115, 116].

We first evaluate the spatial ACFs $\left(C_{\mathrm{xx}}(\tau), C_{\mathrm{yy}}(\tau), C_{\mathrm{zz}}(\tau)\right)$ of the particle centre of mass trajectories. $C_{\mathrm{xx}}(\tau)$ and $C_{\mathrm{zz}}(\tau)$ decay as a single exponential with characteristic decay frequencies $\omega_{\mathrm{x}} = 28\ \mathrm{s}^{-1}$ and $\omega_{\mathrm{z}} = 6.4\ \mathrm{s}^{-1}$. Contrariwise, $C_{\mathrm{yy}}(\tau)$ is well fitted with a double exponential with characteristic frequencies $\omega_{y,1} = 42\ \mathrm{s}^{-1}$ and $\omega_{y,2} = 2.7\ \mathrm{s}^{-1}$, Fig. 2.8-a. We associate the fast decay rate to the translation, while the slower decay can be related to rotation around the x-axis (α) induced by a motion along the y-direction. The values of the normalized cross-correlation function between α and y at zero time lag ($C_{\alpha y}(0) = -0.368$) further confirm a roto-translation coupling, Fig. 2.9-c and see [117]. Fig. 2.9-b shows a density plot of the rotation around the x-axis (α) as function of the motion along the y-direction. Here it can be seen a moderate negative correlation which suggests that the RBC rotates as it moves away from $y_{\mathrm{eq},2}$, and undergoes to an "oscillating" motion about the equilibrium configuration where it is stably confined. To better comprehend this correlation we calculate $F_{\mathrm{y}}(\alpha)$ (Fig. 2.9-d) and $\tau_{\mathrm{x}}(y)$ (Fig. 2.9-e) which undoubtedly shows the coupling between the motion along y and α. Actually, the cell in its "folded" position (i.e. $\alpha = 90^\circ$) is constantly subjected to a force along the y-direction that moves the particle away from $y_{\mathrm{eq},2}$ which in turns induces a rotation around the x-direction. On the other hand, as extensively described by Tognato et al., the transverse forces and torques components confine the cell in its "folded" configuration [110]. The overall consequence of these stable and unstable equilibria is a "circulating motion" of the cell within the optical trap about the equilibrium configuration. This would suggest that the coupling is intrinsically due to particle shape and to the optical trap rather than to the hydrodynamic of the particle.

Lastly, we extract average values and the standard deviations for the force constants ($k_{2,x} = \frac{\omega_{\mathrm{x}} k_b T}{D_{\mathrm{xx}}} = 0.166 \pm 0.024 \frac{\mathrm{pN}}{\mu\mathrm{m}\cdot\mathrm{mW}}$, $k_{2,y} = \frac{\omega_{\mathrm{y}} k_b T}{D_{\mathrm{yy}}} = 0.218 \pm 0.025 \frac{\mathrm{pN}}{\mu\mathrm{m}\cdot\mathrm{mW}}$, $k_{2,z} = \frac{\omega_{z} k_b T}{D_{zz}} = 0.005 \pm 0.001 \frac{\mathrm{pN}}{\mu\mathrm{m}\cdot\mathrm{mW}}$). These values are in excellent agreement with a previously re-

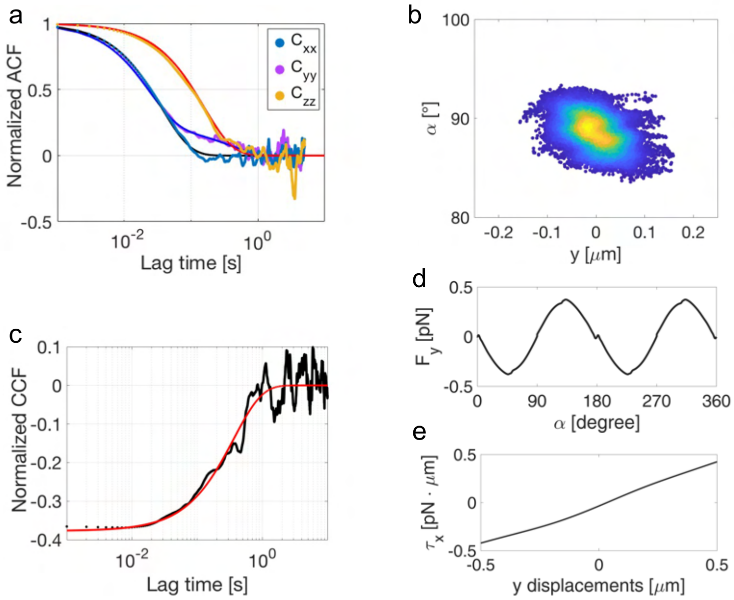

Fig. 2.9 Analysis of the double trap configuration. a) Translational autocorrelation function. The solid lines are exponential fits. $C_{xx}(t)$, $C_{zz}(t)$, decay as single exponential while $C_{yy}(t)$ as double exponential. b) $y-\alpha$ correlation shown as density plot. c) Normalised cross-correlation function between the rotation around the x-axis (α) and the y-displacement (red line exponential fit). Both $F_y(\alpha)$ d) and $T_x(y)$ e) reveal unstable equilibrium when the cell is tilted of 90° around the x-axis (i.e. RBC in its folded position). Image taken from [111].

ported work [110]. Similarly to the translational motion, we calculate $C_{\alpha\alpha}(\tau)$ and $C_{\gamma\gamma}(\tau)$. $C_{\alpha\alpha}(\tau)$ and $C_{\gamma\gamma}(\tau)$ decay as a single exponential and the respective trap constant are: $k_\alpha = \frac{\omega_\alpha k_b T}{D_{\alpha\alpha}} = 0.352 \pm 0.096\,\frac{\mathrm{pN}\cdot\mu\mathrm{m}}{\mathrm{rad}\cdot\mathrm{mW}}$ and $k_\gamma = \frac{\omega_\gamma k_b T}{D_{\gamma\gamma}} = 1.587 \pm 0.382\,\frac{\mathrm{pN}\cdot\mu\mathrm{m}}{\mathrm{rad}\cdot\mathrm{mW}}$. We do not analyse the dynamics around β since the cell is not confined about this axis.

2.3.3 Triple trap

As previously suggested, one of the greatest advantage of using a NN instead of GO is the significant lowered computation time, especially when a very high number of light rays is needed (e.g. a triple- or four beams optical tweezer). Now, we exploit this feature to investigate the equilibrium orientation and position of a RBC with a reconfigurable triple-beam OT.

If directly trapped, a healthy biconcave RBC can assume two different and alternative orientations within the optical trap depending on the number of beams used for trapping [107, 110]. In a double-beam OT, the major axis of a RBC is parallel to the optical axis and the beam foci are contained in the cell, known as “folded” configuration [49]. On the contrary, if three or four beams arranged in symmetric configurations are used (i.e. beams foci on the vertex of equilateral triangle or a square), the major axis of the cell is confined to be orthogonal to the optical axis (i.e. $\alpha = 0°$), configuration referred to as ‘flat’ configuration [118]. Here, we sought for alternative (and intermediate) RBC equilibrium configurations in respect to the well-known “folded” and “flat” ones.

We consider a trap configuration that is intermediate to those able to trap the cell in its “folded” or “flat” configuration. We consider a triple-beam optical tweezers (TBOT) composed by three identical and tightly focused Gaussian laser beams. Two beams are always arranged along the x-axis in a diametrically opposite location on the thickest portion of the cell (white crosses in Fig. 2.10-a). A third beam (yellow cross in Fig. 2.10-a) can be translated over the thickest portion of the cell and is used to counteract T_x generated by the two fixed beams. For simplicity, henceforth, the position of the moving beam is described by a polar co-ordinates system in the $x-y$ plane. Its location is defined by a single angle (ζ), and the distance from the origin is fixed and equal to the radius of the thickest portion of the cell (2.76μm), Fig. 2.10-a.

Next, we proceed with the identification of the positional and translational equilibria. As a first step in our investigation, we simulate a force-field acting on the cell for $\zeta = 45°$ to appreciate the effect of the potential landscape on the RBC. In this simulation, the cell is in its “flat” configuration and located at $z = 0$. It can be seen that the light pattern creates a very complex force-field (Fig. 2.10-b). Non-negligible optical forces act simultaneously along the $x-$ and y-direction for every location of the cell. The complexity of the force-field makes it extremely difficult to identify the equilibrium positions (i.e., point in space where a specific force component vanishes with negative slope). This process would require several reiterations for every degree of freedom, rendering the process labour intensive. However, we note that if a particle is subjected to an optical potential and it falls into the equilibrium position/orientation, it would be possible to identify the equilibrium configuration studying its dynamics as suggested by Cao et al [119].

From symmetry arguments, the effect of different locations of the third beam can be understood restricting ζ in the interval $[0°, 90°]$ as schematically depicted in Fig. 2.10-a. Moreover, since we are looking for alternative equilibrium configurations (or to a transition from a “flat-like” to “folded-like” configuration), it is also rational to disregard every position where two beams are too close to each other (i.e. $\zeta < 15°$), which should induce a “folded” configuration. Thus, the position of beam 3 can be restricted to $15° \leq \zeta \leq 90°$. To evaluate the effect of the reconfigurable optical trap, ζ is sampled every 15°, and for each ζ the Brownian dynamics are simulated for a 10 s trajectory starting from a RBC positioned in its ‘flat’ configuration ($\theta = 0°$ and $\phi = 0°$) centred at $(0,0,0)$. The simulation finishes once the cell equilibrates around a stable position and orientation. The final position and orientation

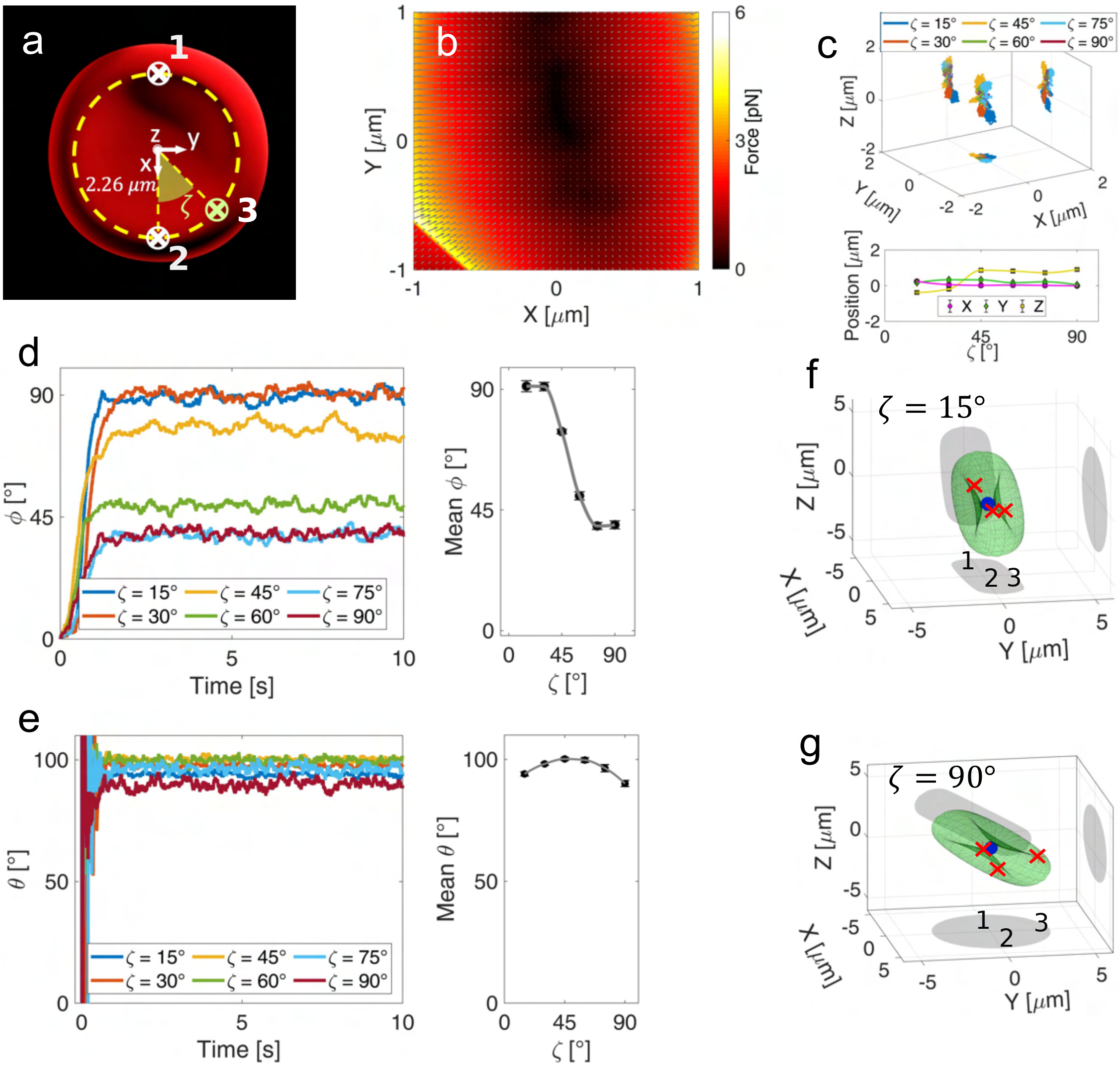

Fig. 2.10 Red blood cell trapped in a triple beam configuration. a) Schematic depiction of the triple-beam optical trap and the polar co-ordinates system used to identify the position of the moving beam, and respective beam definition as beam 1, 2 and 3. (b) Force-field acting on the RBC located on a grid of coordinates in the x-y plane for $\zeta = 45°$. The colour code indicates the total force acting on the x-y plane, while the grey arrows indicate the direction of the force. (c) Three-dimensional trajectories of the cell centre of mass over a simulation time of 10 s for different ζ, and the average values for the last second of simulation. d) Polar (ϕ) and e) azimuthal (θ) orientation of the RBC as a function of the simulation time. Average orientations are measured over the last second of the simulation. The error bar represents the standard deviation. f,g) Final equilibrium configuration for a RBC in the reconfigurable triple beam optical trap for $\zeta = 15°$ and $90°$ respectively. The blue dot indicates the center of mass of the RBC while the red stars indicates the beams' foci. The numbers indicate the position of each of the beams. Image taken from [111].

are then shown as the average position and orientation with the standard deviation of the last second of the simulation.

Fig. 2.10-c shows the 3D trajectories of the RBC's CM obtained from the simulations carried out for different ζ. Here, while x and y equilibrium positions remain close to the origin for different angles, the equilibrium in z does depend on ζ. In particular, for $\zeta < 30^\circ$, $z_{eq} < 0\mu$m and for $\zeta > 45^\circ$, $z_{eq} > 0\mu$m, Fig. 2.10-c. We anticipate that for $\zeta \leq 30^\circ$, the cell is in its "folded" configuration, Fig 4-d and Fig. 2.10-f. This is due to a combination of the light intensity distribution and the cell configuration within the trap. In fact, when the cell is in its "folded" position, the cell's major axes are parallel to the direction of propagation of the light beam. In this condition, more highly converging "light rays" strike the biggest faces of the RBC. This increases significantly the gradient force (F_g). Simultaneously, while in folded position, the scattering force (F_s) decreases appreciably because of the smaller geometrical cross-section of the cell. However, if ζ increases, this effect is less pronounced since the light rays strike the cell less symmetrically, and for $\zeta = 30^\circ$, $z_{eq} \sim -0.2\mu$m. Conversely, for $\zeta \geq 45^\circ$ a net shift in the axial position is evidenced ($z_{eq} \sim 0.8\mu$m), and this is due to a sequential shifting from the "folded-like" configuration to a "flat-like" configuration, Fig. 2.10-c and Fig. 2.10-d.

Much more interesting is the analysis of the rotational equilibrium. In Fig. 2.10-d are shown the polar orientation (ϕ) of the cell as a function of the simulation time for different locations of the moving beam (i.e. various ζ). It is evident that ζ strongly influences the final polar orientation of the cell, Fig. 2.10-d. In particular, as beam 3 approaches beam 2, the cell tilts more until it reaches the "folded" configuration (i.e. $\phi = 90^\circ$) for $\zeta = 30^\circ$. Analysing the final orientation of the cell in more detail, it is possible to discriminate between three different regions. When the two beams are close to each other, $\zeta \leq 30^\circ$, the cell is in the "folded" configuration. If $30^\circ \leq \zeta \leq 75^\circ$, the RBC's tilting seems to vary linearly with ζ, from a "folded-like" configuration to "flat-like" configuration. The last region is for $\zeta \geq 75^\circ$, where the cell tilting cannot be decreased further, Fig. 2.10-d. It is also interesting to note the minor effect that ζ has on θ. Here, we define $\theta = 0^\circ$ when z_p (defined in Figure 1-a) is pointing along the positive x-direction. For example, in the simple case of a double beam optical tweezers, the cell plane point towards the positive ($\theta = 90^\circ$) or negative ($\theta = 90^\circ$) y-axis. Either direction are equally plausible due to the symmetry of the cell. Therefore, in the case of a triple beam optical tweezers, the induced cell rotation around the z-axis is relatively small for different location of beam 3. In fact, the cell rotates at most of $\approx 10^\circ$. Yet, the rotation can be explained with the tendency of maximizing the overlapping volume between the trapped particle and the illuminating beam in order to minimize the energy of the system. This can be well understood in the discrete dipole approximation. In particular, for $\zeta = 45^\circ$ it is possible to obtain the highest cell's tilting around the z-axis, Fig. 2.10-e. For every other ζ, the tilting of the RBC around the z-direction decreases towards $\theta = 90^\circ$.

2.4 Microplastics trapping

Microplastics, defined as plastic particles with dimensions below 5 millimeters [51], pose a significant environmental threat due to their widespread distribution in various ecosystems, including oceans and freshwater bodies. The potential for transfer through the trophic chain [53] makes them a source of contamination at all trophic levels, raising concerns about potential impacts on human health. Thus, conducting a comprehensive study of microplastics is essential to assess their sources, distribution patterns, and ecological implications, as well as to formulate effective strategies for environmental protection and human well-being.

Notably, existing surveys have primarily focused on particles with sizes $\geq 20\mu$m [120–123], with limited reports addressing the sub-20μm fraction [124, 125]. Recently, Raman tweezers have emerged as an efficient tool to study small microplastics and nanoplastics [54, 55]. In this section, we utilize machine learning techniques to improve the calculation of trapping stiffness for microplastics with different refractive indices and radii ranging between 50 and 1000 nm. Given that the size of these particles is comparable to the wavelength (785 nm) of the trapping laser, we employ the T-matrix approach for the calculations [126]. Despite the fact that T-matrix provides accurate results, such calculations can be extremely computationally demanding.

In our study, we demonstrate the remarkable capability of NN to accurately predict trap stiffness values for microplastics with radius and refractive index values never encountered during training. The training dataset available to the NN is relatively small, comprising 156 data points (39 points for each of the four different refractive indices: 1.4, 1.5, 1.6, and 1.7, distributed between 50 and 1000 nm radius), as shown in Fig. 2.11(a). This data set is generated for a laser power of 1 mW and an objective with a NA of 1.3. Despite this limited dataset, the NN, see architecture in section 2.5, is able to effectively generalize and successfully predict trap stiffness values for different values of refractive indices (1.45, 1.55, and 1.65). As depicted in Fig. 2.11(b), the NN predictions (represented by the dashed line) align precisely with the exactly calculated data points (purple stars).

Moreover, it is noteworthy that the NN's prediction extends effectively to intermediate radii, as illustrated by the red data point in Fig. 2.11(b). The NN captures the intricate variations in the "fine" structure of the trap stiffness, outperforming traditional methods like linear interpolation. This ability of the NN to adapt to previously unseen data points

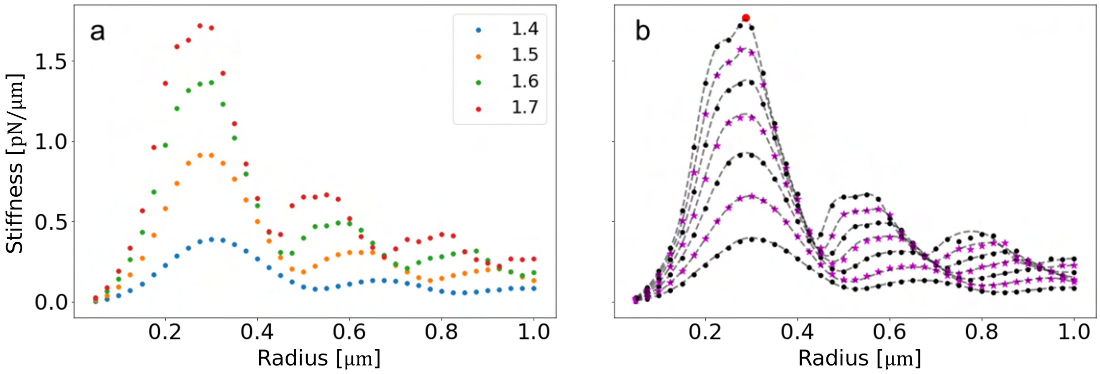

Fig. 2.11 Stiffness of microplastics trapping using a 785 nm laser with 1 mW power, focused through a 1.3 NA objective. (a) Transverse stiffness as a function of radius for different refractive indices, calculated using the T-matrix approach. This dataset represents all the available data used for training the NN. (b) The scatter points represent exact stiffness calculations for specific refractive indices and radii, while the dashed lines indicate the NN predictions. The black scatter points correspond to the data shown in panel (a), whereas the purple stars represent data that the NN has not encountered during training. Notably, the NN exhibits remarkable generalization ability. The NN prediction matching the red point obtained with the exact calculation at a radius of 0.3 μm and a refractive index of 1.7 illustrates the NN's superior performance compared to a simple linear interpolation method.

and interpolate complex relationships enhances the accuracy and reliability of trap stiffness predictions for a wide range of microplastic configurations.

Indeed, the NN's remarkable ability to generalize the calculation offers a broader perspective, as demonstrated in Fig. 2.12. The comprehensive map of the parameter space provides valuable new insights into the optical trapping of microplastics. Moreover, this approach paves the way for the inclusion of additional parameters, such as the trapping wavelength, to further enhance the optimization and study of small microplastics and nanoplastics using optical trapping techniques.

2.5 Methods

2.5.1 Neural Networks

Here, we discuss the training, architectures, data generation, range of validity, and the hardware and software utilized for the Neural Networks.

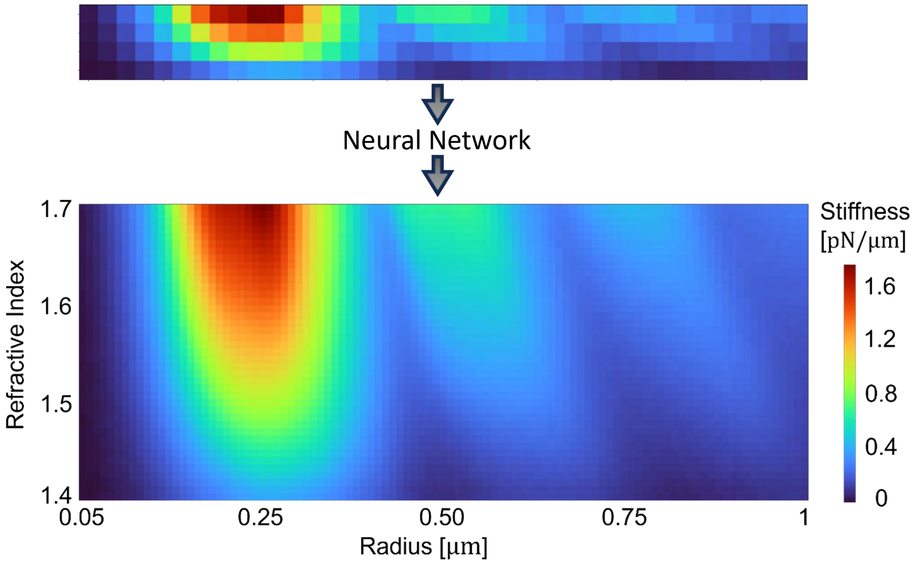

Fig. 2.12 Map of the stiffness as a function of radii and refractive index. The first map is the one obtained plotting the 156 training points computed with the T-matrix method during several days while the map below contains over 4000 points and is the one generated with the NN in a fraction of a second.

Training

The training procedure is composed of five main steps. These include defining the architecture and pre-processing the data (both executed just once), followed by data loading, the actual training phase, and performance evaluation (all of which are conducted iteratively). The architecture definition consists of choosing the number of layers and the number of neurons per layer. A schematic of the structure of this type of NN can be found in Fig. 2.2. The architecture is adjusted according to the complexity of the different studied problems. In general, a higher number of trainable parameters will produce a model that will be able to learn more from the training data. However, we must be careful; we do not want to learn the artifacts coming from GO. The training data is obtained by calculating the optical forces using GO for a given set of parameters. These parameters can be spread over very different scales, from around unity in the case of parameters like the aspect ratio or the refractive index, to $\sim 10^{-6}$ for the positions, $\sim 10^{-12}$ for the forces and $\sim 10^{-18}$ for the torques. To achieve an efficient training of the NN we need to apply a pre-processing step where the variables must be rescaled around unity and the angles are expressed in terms of sines and cosines to avoid inconsistencies around 2π. Shuffling the data and dividing them into a validating and training set is the final step of the pre-processing.

The iterative part of the training starts by loading a subset of the training data and applying the training step where the NN weights are optimized to minimize the loss function. We used the mean squared error as the loss function and the Keras implementation of the Adam optimizer with the default parameters [127]. When the weights of the NN have been updated, the training data is deleted from the RAM memory and another subset of the training data is loaded before repeating the same process. Dividing the training set in smaller subsets (instead of loading all the data at once) allows to use big training sets independently of the RAM memory of the computer. Once the training dataset has been fully explored through all the subsets, the error between the NN calculation and the validating dataset (defined as the mean square difference) is computed. The iterative step is repeated until this error stops decreasing. For the training data generated using for example 100 rays the artifacts are significant enough that a well trained NN could learn them. In order to prevent these artifacts from being acquired by the NN, the error between the NN calculations and the validating data generated with 1,600 rays is computed. The training stops when this value reaches its minimum. Fig. 2.13 shows how the NN starts to acquire the information of the artifacts present in the calculation with 100 rays. This is favoured by the fact that the architecture is more complex and by not using a validating data set generated with more rays to decide when to stop the training.

Architectures

- Spheres (3 Degrees of freedom): The NN architecure for 100 and 400 rays consists of 5 hidden layers with 16 neurons each of them ($\approx 1 \cdot 10^3$ trainable parameters) while for 1600 rays consists of 3 hidden layers with 64 neurons in each of them ($\approx 8 \cdot 10^3$ trainable parameters)

- Ellipsoids (9 Degrees of freedom): The NN architecture for 400 rays consists of 5 hidden layers with 384 neurons each of them ($\approx 6.0 \cdot 10^5$ trainable parameters) while for 1600 rays consists of 8 hidden layers with 384 neurons each ($\approx 1 \cdot 10^6$ trainable parameters)

- Red blood cells (5 Degrees of freedom): The NN architecture for 400 rays consists of 7 hidden layers with 256 neurons each of them ($\approx 4.0 \cdot 10^5$ trainable parameters).

- Microplastics (2 Degrees of freedom): The NN architecture for training with 156 data generated with the T-Matrix formalism consists of 3 hidden layers with 32 neurons each of them ($\approx 3.3 \cdot 10^3$ trainable parameters).

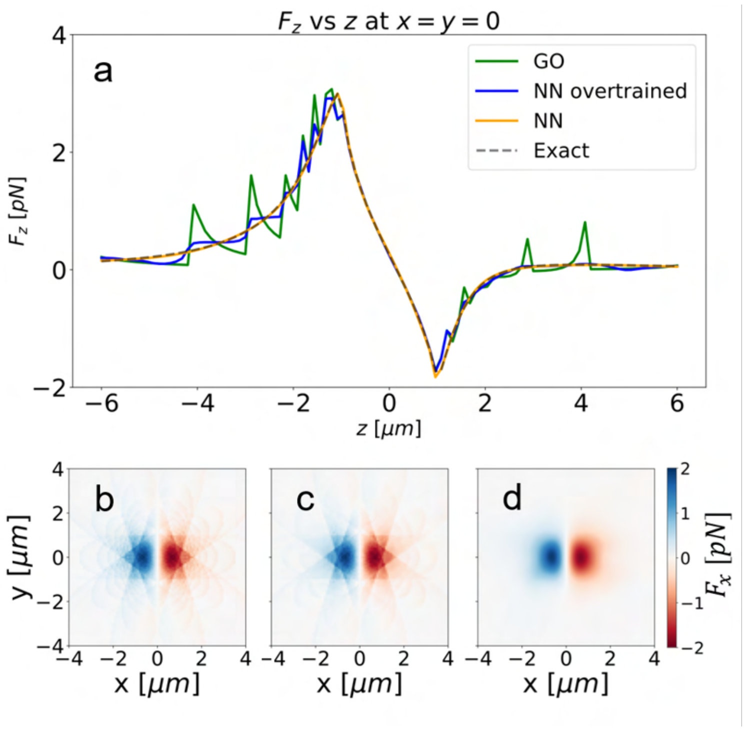

Fig. 2.13 Comparison between geometrical optics with 100 rays, the exact calculation, and two different NNs trained for 100 rays, one trained using a threshold and with a simple architecture (NN) and the other one trained without threshold and with a more complex architecture (NN overtrained). (a) Shows F_z in the axial direction with the different approaches. While the NN properly designed matches perfectly the exact calculation, the NN that is overtrained acquires the artifacts from geometrical optics. (b,c,d) show the force in the $x-y$ plane at $z = -1.2\mu$m calculated with geometrical optics, the overtrained NN, and the properly trained NN respectively. While the overtrained NN (c) keeps the overall structure of the artifacts, the properly trained NN (d) is able to remove them. Image taken from [76].

Data generation

The data for training the NN is generated with the GO method. The optical forces calculation is computed with different numbers of rays, allowing to compare the machine learning and the traditional approaches in different situations. The data points are randomly selected from the parameter space of interest. Since the force profile changes faster close to the focus, the position parameters (x,y,z) are chosen according to a normal distribution centered in the beam focus. To get an uniform probability of orientations of the non-spherical particles in the case of the ellipsoids and the red blood cells, the probability of generating an orientation angle θ is proportional to $\sin\theta$. The rest of the values of the parameters are equally probable.

Table 2.4 Parameters space for the sphere (3 DOF), general ellipsoid (9 DOF), the red blood cell (5 DOF), and the microplastics (2 DOF). l is defined as the maximum between dimensions a and c

	Sphere	Ellipsoid	Red blood cell	Microplastics
a	$1\mu\mathrm{m}$	$[0.5\mu\mathrm{m}, 3\mu\mathrm{m}]$	$3.91\,\mu\mathrm{m}$	$[50\mathrm{nm}, 1\mu\mathrm{m}]$
c	$1\mu\mathrm{m}$	$[0.5\mu\mathrm{m}, 3\mu\mathrm{m}]$	$1.26\,\mu\mathrm{m}$	
θ		$[0, \pi/2]$	$[0, \pi/2]$	
ϕ		$[0, 2\pi]$	$[0, 2\pi]$	
NA	1.3	$[0.25, 1.3]$	1.3	1.3
n	1.5	$[1, 4]$	$[1.4, 1.7]$	
$\mathbf{r}$	$r_i \in [-4\mu\mathrm{m}, 4\mu\mathrm{m}]$	$x, y \in [-4l, 4l]; z \in [-6l, 6l]$	$r_i \in [-4\mu\mathrm{m}, 4\mu\mathrm{m}]$	

Training region and range of validity of the NN

The validity of the Neural Network (NN) to compute optical forces is constrained to a specific training region, defined by a set of parameters. In Table 2.4, the range of validity for the various NNs utilized in our study is detailed. While certain networks (e.g., those designed for spheres, RBCs, and microplastics) have been tailored to specific problems, we recognize that the majority of experiments likely fall within the general parameter region defined for the ellipsoid. It is important to note that if there is a need to employ the NN outside this established validity region, additional training within that specific region will be necessary.

Hardware and software

The NNs are modelled and trained in Python using Keras (version 2.2.4-tf) [127] with TensorFlow backend (version 2.1.0). The training of the NN is done in a GPU type NVIDIA GeForce RTX 2060 with 16 GB of memory. The processor of the computer is an Intel Core i7-10700 and it has 16 GB of RAM.

2.5.2 Brownian dynamics simulation

The particle dynamics simulation consists on the integration of the Langevin equations considering the Brownian motion, the optical force and torque contribution, and the non spherical shape. Since we will be considering microscopic particles in water, we can safely consider the overdamped regime [128]. For simplicity, we start by considering a sphere moving in 2D. In the overdamped regime, the Langevin equations can be written as:

$$\frac{dx}{dt} = \frac{F_x}{\gamma_t} + \sqrt{2D_t}\,\xi_x(t) \tag{2.1}$$

$$\frac{dy}{dt} = \frac{F_y}{\gamma_t} + \sqrt{2D_t}\,\xi_y(t) \tag{2.2}$$

$$\frac{d\theta}{dt} = \frac{T_\theta}{\gamma_r} + \sqrt{2D_r}\,\xi_\theta(t) \tag{2.3}$$

where $D = k_B T/\gamma$ and where γ_t and γ_r are $6\pi\eta R$ and $8\pi\eta R^3$ respectively. η is the viscosity of the fluid. When simulating more complex shapes, the diffusion tensor, which depends only on the shape of the particle, becomes slightly more complicated. In the case of the ellipsoids we can use the analytical solution for ellipsoids derived by Perrin [129, 130]. In the case of the RBCs, the morphology is more complex and requires numerical methods for its determination. Here, we used the bead model technique developed by De La Torre et al., exploiting the widely used software winHYDRO++[131, 132]. In the bead model, a series of spheres are used to approximate the size and the total volume of the RBC. From the bead model, winHYDRO++ calculates the 6x6 tensor (Ξ) encoding the hydrodynamic resistance of the non-spherical particle. We then obtain the diffusion tensor $\mathbf{D}$ via the generalised Einstein relationship [133]:

$$\mathbf{D} = k_B T \Xi^{-1} \tag{2.4}$$

where k_B is the Boltzmann constant, and T is the temperature of the system. While the tensor needs to be computed only once per simulation, the rest of the steps need to be computed iteratively.

In each time step we compute the contribution to the motion of the optical force and torque (lab frame of reference) and of the Brownian noise (particle frame of reference). Since both contributions are computed in different frames of reference, we need to continuously build the matrices that allow us to switch from one to another. While generating the Brownian motion contribution and computing the matrices can be fast, the optical contribution to the force and torque used to be the bottle neck of the process and is the one now being optimized by the NN. Once the contributions to the rotation and displacement are computed, we relocate and reorient the particle. To implement correctly the rotation of the axes of the particle reference frame we used the Rodrigues formula [134, 128]. Repeating this process for each time step allows to construct the trajectories from where we can obtain statistical properties like the probability distribution or the Kramer's rate of the ellipsoid in a double beam OT.

2.6 Conclusions

Employing NNs, the compromise between speed and accuracy for the calculation of optical forces on microscopic sized particles with complex shapes is no longer a limitation. By computing the optical forces using GO, it is possible to train a NN that predicts the forces not only faster but also with higher accuracy. The NN can enhance the accuracy of the training data, allowing us to train it with faster, less precise data. We only need a small amount of more accurate data to know when to stop the training.

The NN approach works not just for spheres, but also for more complex shapes. Even a single NN that considers all the key factors in an optical tweezers experiment is faster and more accurate than the traditional GO method. This improvement allows us to study the behavior of ellipsoids in double beam optical tweezers, including the balance points and changes related to trap distance and ellipsoid shape. With GO, we could have studied one specific point, but mapping the whole area was not possible. Now, we can even extend our study to complex shapes like red blood cells, exploring different trapping setups, and map the trapping stiffness for microplastics using T-matrix data.

While training a Neural Network (NN) can be time-consuming, the resulting advantages are substantial. The lengthiest part of the process is generating the training data, but this can be accelerated by parallelizing the calculation. Once the NN is trained, two primary benefits are realized. Firstly, the increase in computational speed enables the exploration of scenarios that were previously beyond the reach of the Geometrical Optics (GO) approach. Secondly, a trained NN is more straightforward to utilize and integrate with other software compared to existing GO methods. We have prepared a tutorial, including the trained NNs, demonstrating how to use them (see https://github.com/brontecir/Deep-Learning-for-Geometrical-Optics).This approach can be adapted to various trapping configurations, beam profiles, or particle shapes without additional complexity (unless the DOF are increased). We believe that NNs could democratize the ability to perform optical forces calculations, allowing for a further development of the optical manipulation field pushed by numerical simulations.

Chapter 3

Optical trapping for space applications

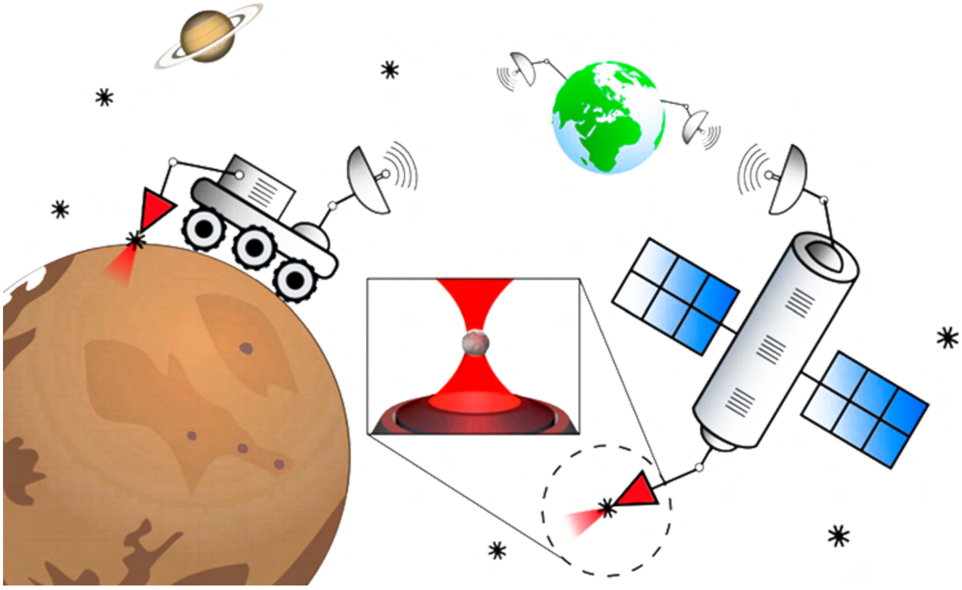

Dust pervades the universe, but until the mid-20th century it was merely seen as a nuisance that obscured starlight. Today, we recognize the vital role of dust in processes such as planetary, star, and galaxy formation and the ignition of a potentially life-bearing chemistry. In this chapter, we delve into the exploration of cosmic dust using optical tweezers. By characterizing dust particles in water with standard and Raman tweezers, we can determine their mineral composition and response to light. This opens up possibilities for using optical tweezers in sample return missions and extraterrestrial environments. In the accompanying image, optical tweezers are depicted as a potential tool for space exploration, underscoring their promise for analyzing cosmic dust beyond our planet. Image credits: Alessandro Magazzù from CNR-IPCF Messina [56].

3.1 Investigation of cosmic dust with optical tweezers

Cosmic dust has become a subject of interest in astrophysical science and related technology due to its role in cycling processes active in the universe. The term cosmic dust refers to small solid particles ranging in size from a few nanometers to tenths of millimeters that are present in the interstellar medium (interstellar dust) or in the interplanetary space of the solar system (interplanetary dust). Interstellar dust is mainly generated by the lifecycles of many generations of stars: it is released by radiation pressure and solar wind or ejected during the end-time explosion of stars or during the blowing off of their outer layers [135–137]. Interplanetary dust is formed through collisions between solid bodies (e.g asteroids, planets and their satellites) or evaporation of icy bodies (e.g. comets [138]). Remote observations are mostly used to study interstellar dust [139, 140], whereas interplanetary dust is available through sample-return space missions from interplanetary medium, planets, and minor bodies [141–143], or by collecting particles from the Earth's stratosphere [144–147] and micrometeorites from its surface (e.g., [148–150]). These collected samples are then analyzed at terrestrial facilities using state-of-the-art analytical techniques since some instruments are too large to be flown into space [151–153].

The physico-chemical properties of cosmic dust can be examined through techniques such as X-ray diffraction [154], Transmission Electron Microscopy [155], Raman spectroscopy [156, 157], and mass spectroscopy [158]. However, these traditional methods can encounter complications, such as unwanted effects from substrate shielding or interference from other particles. To overcome these challenges, we have adopted optical tweezers, a contactless and non-destructive approach, and employed standard and Raman tweezers to investigate individual grains of cosmic dust [159, 56]. By focusing a laser beam with great precision, optical tweezers enable the trapping and manipulation of dust particles without physical contact, as they exchange momentum with the particles. This allows for tracking and analyzing the particle dynamics within the optical trap, thereby facilitating the characterization of the response of dust partiles to optical forces and torques. In addition to this, the mineralogical composition of the dust particles can be identified using Raman tweezers.

Our Raman tweezers have trapped and characterized a diverse range of samples, focusing on those with known textures and mineralogic compositions. Our goal is to validate the application of optical manipulation techniques to cosmic dust by reproducing the well-known compositions of these trapped particles. We have analyzed samples of both terrestrial and extraterrestrial origin, including: (1) a quartzarenite (M-26) from the Kamil Crater in Egypt [160], (2) a hawaiite from the Etna volcano in Italy (HE-1), (3) the CV3-OxA carbonaceous chondrite Allende (A-1), and (4) a lunar meteorite (polymict regolith breccia) found in Antarctica (DEW 12007) [161]. Previously, mineral grains used to calibrate the dust analyzer

Giada on board the Rosetta space mission [162] were used as the simplest possible starting material (monomineralic, uniform size range). In this work, we have purposely chosen more complex, non-uniform samples to make our investigations more representative of the range of materials found in the solar system. The terrestrial rocks M-26 and HE-1 are considered analogues of planetary materials and contain both mono and polymineralic components. Meanwhile, the extraterrestrial rocks, representing primitive (A-1) and differentiated (DEW 12007) bodies within the solar system, offer valuable insights into the diversity of cosmic dust.

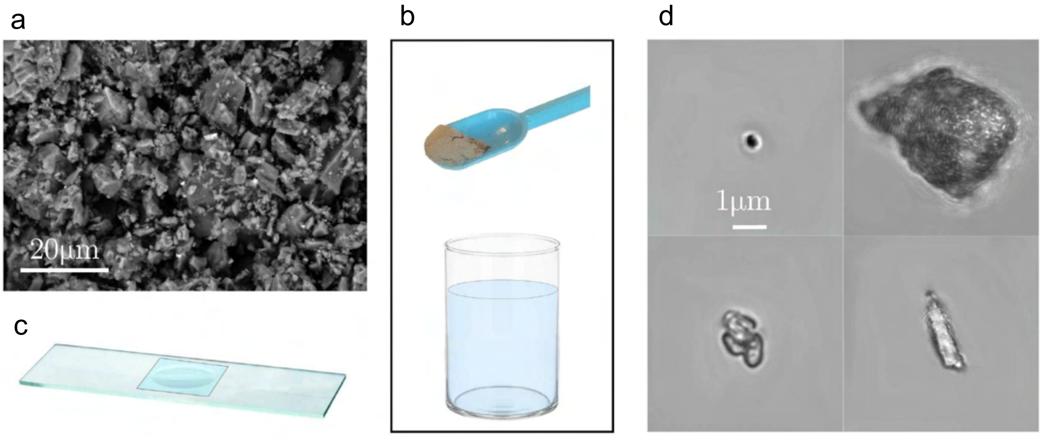

Fig. 3.1 Sample preparation and sketch of the experimental setups. a) SEM image of DEW 12007 lunar meteorite powdered sample showing the poly-crystalline nature of each of the individual grains. b) Dust samples are dispersed in distilled water by ultrasound sonication and c) the solution is placed within a cavity glass slide and sealed with a coverglass. d) Screenshots of four different 3D optically trapped grains of cosmic dust in water solution having different sizes and morphology. Image taken from [56].

Before studying them with optical tweezers, the samples are powdered and analyzed using scanning electron microscopy to characterize their texture, including shape and grain size. X-ray powder diffraction is employed to determine the samples' mineralogy. These characterizations are conducted at the Dipartimento di Scienze della Terra and the Center for Instrument Sharing of the University of Pisa (CISUP). All the optically trapped samples were initially provided as dried powder, with grains displaying a non-homogeneous size and shape distribution, as shown in Fig. 3.1(a,d). The first step in sample preparation for optical trapping involved dispersing the powder in distilled water through ultrasound sonication to achieve an appropriate concentration for optical trapping (e.g., a few particles per microliter). The water-dust solution was sealed in a glass cavity slide, as depicted in Fig. 3.1(b,c), and placed on the sample holder of our optical tweezers for investigation, see Fig. 3.1(c). To study individual dust grain particles dispersed in water, we used both standard and Raman optical tweezers. With standard optical tweezers, we tracked the motion of the trapped particle using a quadrant photodiode (QPD) and analyzed the trajectory to calculate optical forces and rotations resulting from its interaction with light. For Raman tweezers, backscattered light from the particle was collected through the same focusing objective and directed to a Raman spectrometer for phase identification.

3.2 Optical forces and torques on dust particles

By studying the force and torque applied to the particle, we can retrieve information about the light-matter interaction. The configuration of the standard optical tweezers is as explained in Chapter 1 and depicted in Fig. 1.3. Specific details about the configuration can be found in section 3.4.

The output signals from the QPD, proportional to the particle displacement from its equilibrium position, are analyzed to calculate both the trap stiffness and to detect particle rotation in the perpendicular $x-y$ plane. We utilize autocorrelation function (ACF) and power spectral density (PSD) calibration methods [4, 163], see section 1.3, to obtain the relaxation frequencies of the trapped particles as fitted parameters. These parameters enable the calculation of the trap stiffness, as illustrated in Fig. 3.2(a). An observed increase in the stiffness of an optically trapped grain of the lunar meteorite DEW 12007 corresponds with increased laser power, as shown in Fig. 3.2(c). Notably, the three components of the stiffness, κ_x, κ_y and κ_z, increase almost linearly with laser power. Differences in stiffness along the x and y directions may be attributed to a possible asymmetry of the trapped grain with respect to the propagation axis z. The comparatively lower values of the stiffness κ_z relative to κ_x and κ_y result from the longer extension of the Gaussian beam along the z axis [4].

The linearity of stiffness with power enables the determination of the stiffness efficiency, denoted as $q_i = k_i/\mathrm{P}$ (with $i = x, y, z$) by fitting the values of κ_i shown in Fig. 3.2(c), where P is the laser power at the objective output. Specifically, through linear fitting, we obtain $q_x = 1.38$ pNμm^{-1}mW^{-1}, $q_y = 1.104$ pNμm^{-1}mW^{-1},and $q_z = 0.536$ pNμm^{-1}mW^{-1}, respectively. Radiation pressure on complex shaped or absorbing particles can also have a destabilizing effect by pushing the trapped particles in regions of lower intensity along the z axis. For example, grains from Allende meteorite are difficult to trap in 3D and were investigated in 2D when pushed against the wall of the cell.

Rotations of a trapped particle induce a correlation between its x and y trajectories. In such scenarios, optical tweezers can be utilized for *photonic torque microscopy* to quantify these rotational motion [117]. Specifically, rotations occurring in the $x-y$ plane can be highlighted by evaluating the differential cross correlations $\mathrm{DCCF}_{xy}(\tau) = \langle x(t)y(t+\tau)\rangle - \langle y(t)x(t+\tau)\rangle$

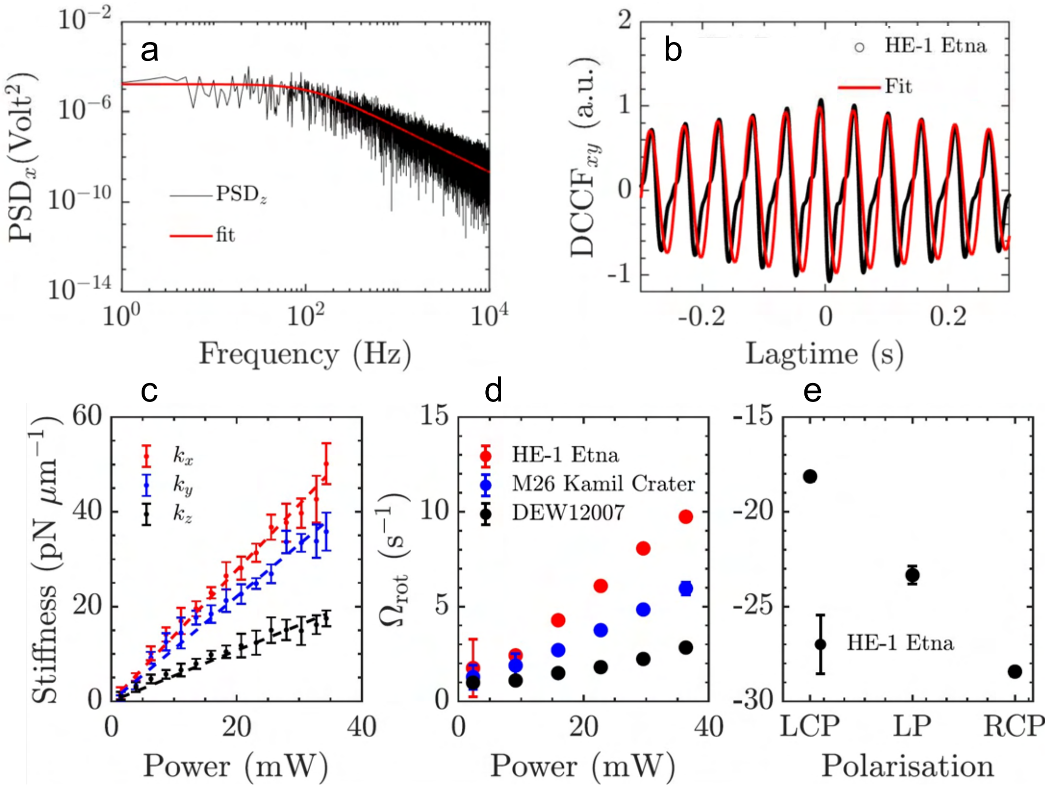

Fig. 3.2 Effects of the laser light on trapped particles. a) The black line represents the power spectrum density (PSD) of the trajectory along the z direction for a trapped dust grain from the lunar meteorite DEW 12007. The red line corresponds to a Lorentzian fit of the calculated PSD, from which the relaxation frequency of the trapped grain is obtained as a fitted parameter. b) The black scatter plot represents the experimental data of the differential cross correlation function $\mathrm{DCCF}_{xy}(\tau)$ of the sample HE-1 from Etna. Discrepancies between the experimental data and the fit (red line) arise due to the presence of a second rotational or vibrational motion caused by the non-spherical geometry and anisotropy of the trapped particle [116]. c) Trap stiffnesses κ_x , κ_y and κ_z as a function of the laser power measured at the objective for a single trapped grain of the lunar meteorite DEW 12007. d) Rotational frequencies Ω_{rot} of different samples as a function of the laser power measured at the objective. e) Rotational frequencies, Ω_{rot}, of an optically trapped single dust grains of HE-1 for different polarised light: left circular polarised (LCP), linear polarised (LP) and right circular polarised (RCP) light. Negative frequency values correspond to an anticlockwise rotation, while positive values correspond to a clockwise rotation, both with respect to the z-axis. Image adapted from [56].

of the signals acquired from the QPD, as illustrated in Fig. 3.2(b), for varying lag times τ. The rotational frequency $\Omega_{\rm rot}$ can be determined as a fitting parameter of the DCCF$_{xy}$ using a sinusoidal model [164, 116]. In Fig. 3.2(d) we show the rotational frequencies $\Omega_{\rm rot}$ of three distinct trapped samples, demonstrating an increase in $\Omega_{\rm rot}$ with higher laser power. It is noteworthy that the polarisation employed for trapping the samples listed in Fig. 3.2(d) is linear and does not possess any spin-angular momentum. Consequently, the observed rotations are solely attributed to the radiation torque exerted by the light on the particles because their asymmetric shape (referred to as the windmill effect).

In the presence of circular polarised light, an additional spin angular torque can be induced by a laser beam, depending on the absorption properties of the particle [165, 4]. When a laser beam is circularly polarized, each photon carries a spin angular momentum of $+h$ for left circularly polarized light (LCP) and $-h$ for right circularly polarized light (RCP). Consequently, the total torque acting on a non-spherical particle comprises various contributions, including a radiation torque (windmill effect) associated with the particle's shape and the transferred spin angular momentum. Specifically, the spin angular momentum augments the "windmill effect" if they go in the same direction, while it diminishes this effect if they go in opposite direction [4].

In Fig. 3.2(e) we report the rotational frequencies $\Omega_{\rm rot}$ of an optically trapped grain from the terrestrial samples HE-1 from Etna volcano for various light polarizations. In this case, $\Omega_{\rm rot}$ decreases from -18 s^{-1} for LCP to -28 s^{-1} for RCP with a central value of -23 s^{-1} for linearly polarized light (LP). These values indicate that the trapped particle absorbs circular polarized light with a spin angular momentum $+h$ for LCP light and $-h$ for RCP light. Thus, negative frequency values correspond to anticlockwise rotation with respect to the z axis, while positive frequency values indicate clockwise rotation with respect to the z axis. The rotational frequency $\Omega_{\rm rot}$ presented in Fig. 3.2(e) is the result of the combined effect of the total torque acting on the sample. The radiation pressure torque, which is independent of the light polarisation, results in a particle rotation frequency of -23 s^{-1}. However, the spin angular momentum torque either adds or subtracts depending on the light's helicity. For LCP light, the contribution of the spin angular momentum torque is positive, augmenting the radiation torque and increasing the particle's rotational frequency to -18 s^{-1}. Conversely, for RCP light, the contribution is negative, reducing the rotational frequency of the particle to -28 s^{-1}. This observation demonstrates that the overall optomechanical interaction between particles and light relies on both the particle's shape and the helicity of the laser beam.

3.3 Spectroscopic analysis of cosmic dust

We utilize Raman tweezers to examine the mineralogical compositions of terrestrial and extraterrestrial dust grains, focusing on various shapes and sizes. These samples are optically trapped in either three dimensions (3D) or two dimensions (2D) when the radiation pressure exceeds the axial gradient force. When 3D optical trapping is impractical due to radiation pressure pushing the particle along the z direction (aligned with the laser beam propagation), we apply an alternative approach. The particle is constrained against the wall of a glass slide, effectively restricting it in the z direction, while the optical gradient forces confine it in the x-y plane, defining the optical potential. The setup of the Raman optical tweezers is the one explained in Chapter 1 and illustrated in Fig. 1.3. Further information regarding the configuration is provided in section 3.4.

For every sample, we acquire a reference background spectrum in the absence of any trapped particle. This spectrum is utilized to eliminate unwanted signals originating from the glass slide and the surrounding media (such as water or immersion oil). Thereafter, a fitting routine is employed to identify and compare the peaks of each spectrum with reference spectra, enabling us to determine the constituent phases present in the trapped samples. In the initial analysis, we focus on the standard samples M26, HE-1, and A-1, aiming to match their mineral compositions with those reported in the existing literature [160, 166–168].

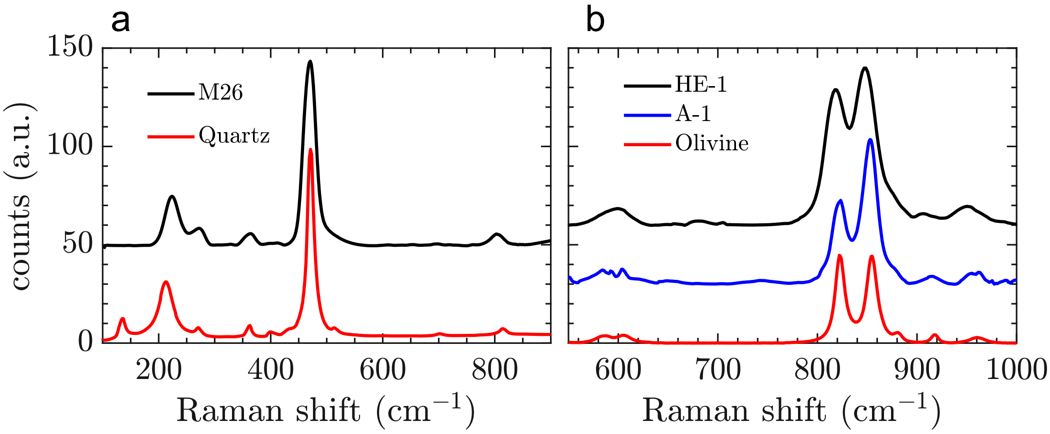

Fig. 3.3 Raman spectra of optically trapped single dust model particles. a) M26 from Kamil crater (black line), red line represents the Raman spectrum of quartz used as reference (RRUFF R150074). b) HE-1 from Etna (black line) and A-1 from Allende meteorite (blue line). Red line represents the Raman spectrum of olivine used as standard reference (RRUFF X050088). Please note that the spectra are offset for clarity. Image adapted from [56].

In Fig. 3.3(a), we report a Raman spectrum (illustrated by the black line) of a single optically trapped grain from sample M26. Quartz, represented by the red line in the figure, is the main constituent identified in this sample, corroborating findings in the literature [160]. Fig. 3.3(b) presents the Raman spectra of two distinctive grains: one from the HE-1 sample collected from Etna volcano (black line) and another from the A-1 sample from the Allende meteorite (blue line). Both meteorites have been previously recognized to contain olivine [168], denoted by the red line in the figure. Notably, the experimental spectra depicted in Fig. 3.3(a,b) align closely with the reference spectra for the identified mineral compositions, validating the accuracy of our measurements.

After testing our Raman tweezers on terrestrial and extraterrestrial standard grains, we investigate cosmic dust from the lunar meteorite DEW 12007. In particular, we trap about 70 different particles in 2D and 3D, following a specific protocol to avoid trapping the same grains multiple times, trapping them in both 2D and 3D configurations. Fig. 3.4(a-e) presents the Raman spectra of four distinct trapped grains of DEW 12007, indicated by the black lines, along with the reference Raman spectra of some of their constituent minerals as reported in the literature [161]. Speficically, in Fig. 3.4(a-e) we observe that the trapped grains contain the following minerals: plagioclase (labradorite); pyroxene (augite and pigeonite); olivine (forsterite and fayalite); ilmenite. The colored lines in the figure represent the reference Raman spectra of these minerals. We identified both monomineralic (Fig. 3.4(a-d)) and polymineralic grains (Fig. 3.4(e)), as expected for a rock in which the grain-size is highly variable.

The mineralogical composition of the lunar meteorite DEW 12007 has been examined through the analysis of over 70 dust grains, and the findings are illustrated in Fig. 3.4(f). The assessment identifies plagioclase as the predominant mineral constituent, constituting 50.5% of the observed occurrences. Following plagioclase, pyroxene appears as the next most abundant mineral, accounting for 27.8% of occurrences. Olivine and ilmenite are present in lower proportions, with abundances of 11.3% and 10.4%, respectively. These observations are consistent with mineral abundance data found in existing literature [161]. It is important to recognize that the grinding process used in preparing the samples may introduce variations in the homogeneity of the cosmic dust. Consequently, some grains may contain multiple mineral components or might not have a distinct mineral identification.

3.4 Methods

The light source of the standard optical tweezers used for the investigation of cosmic dust is a laser diode (LD) generating a linear polarised laser beam with a wavelength of 830 nm. The laser beam is expanded by a two lenses telescope system and reflected by a dichroic mirror towards the back aperture of a high numerical aperture (NA) oil immersion objective,

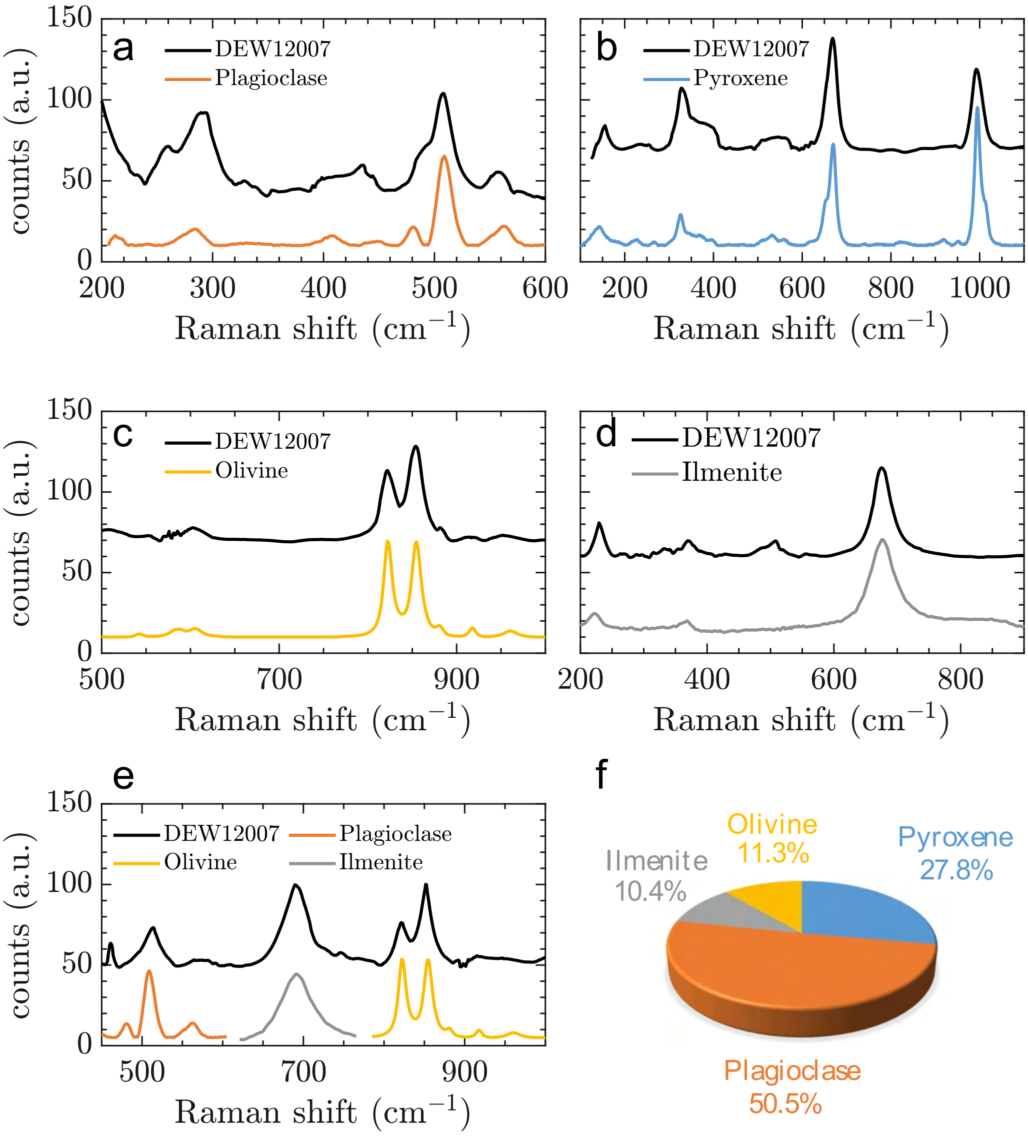

Fig. 3.4 Raman spectra and mineralogical composition of optically trapped dust particles of the lunar meteorite DEW 12007. Black lines represent the Raman spectra of the trapped samples, while colored lines represent the reference Raman spectra from the RRUFF database of: a) plagioclase (RRUFF X050108), b) pyroxene (RRUFF R200002), c) olivine (RRUFF X050088) and d) ilmenite (RRUFF R060149), used for the mineral identification of the trapped single grains. All spectra are offset for clarity. e) Raman spectra of a single grain of DEW 12007 (black line) containing several mineral components (colored lines). f) Mineral occurrence of the mineral constituents over 70 trapped grains of the lunar meteorite DEW 12007. Image taken from [56].

which was also used to imagine the sample on a CMOS camera, see Fig. 1.3. Thanks to the telescope system, the beam overfills the back aperture of the objective giving rise to a highly focused laser beam that maximizes the optical field gradient in the focal spot, resulting in a more efficient trapping. A sample holder is equipped with a 3D translation piezo-stage to move the focal spot within the cavity glass slide containing the sample solution. The dichroic mirror used to reflect the laser beam to the objective acts like a short pass filter, it reflects the laser light towards the objective and transmits the visible light to a CMOS camera, preventing the saturation of the detector and allowing a clear view of the sample on a monitor. The polarisation of the trapping beam can be tuned by a waveplate to investigate the optical response of cosmic dust for different light polarisations. In particular, changing the light polarisation from linear to right- or left-circular, the occurrence of spin-angular momentum transfer from light to the dust can be investigated [169, 4].

The forward-scattered light from a trapped particle, containing information about the particle position, is collected together with the transmitted light by a condenser. The superposition of these two beams generates an interferometric pattern, which is reflected by a second dichroic mirror towards a quadrant photo diode (QPD) through a lens (l_3), see Fig. 1.3[170, 4]. A QPD converts the interferometric pattern collected by a condenser in analogical voltage signals, proportional to the displacement of the particle from its equilibrium position [171, 4, 172]. The signals from the QPD were acquired at a sampling frequency of 50 kHz for time intervals of 2 seconds. The sampled signals were then analysed providing information about the opto-mechanical interaction between light and a single grain of cosmic dust. In order to characterize the optical trapping forces on a single dust grain, we apply the power spectrum method and the autocorrelation function analysis, see section 1.3.

The Raman tweezers used for the identification of the minerals constituents of our samples is a customised setup obtained by coupling a homemade optical tweezers with a commercial Raman spectrometer (Horiba TRIAX 190) through a notch filter, see Fig. 1.3. This filter reflects the laser light, from a laser diode having a wavelength of 780 nm, to the back aperture of an oil immersion objective, similarly to the case of the dichroic mirror previously described in the standard optical tweezers setup, see Fig. 1.3. The notch filter reflects only the single wavelength of the laser beam, and it is transparent to all the other wavelengths. In such a way, the elastic component of the scattering is cut out by the notch filter and only the Raman signal is transmitted to the spectrometer, which is equipped with a grating having a spectral resolution of 8 cm^{-1} and coupled to a silicon Peltier-cooled CCD camera to acquire the spectra. The Raman spectra of our investigated samples were obtained with a laser power of about 7 mW at the sample and acquired with an integration time of few tens of seconds.

3.5 Conclusions

3.5.1 Challenges

Challenges associated with the application of optical tweezers in space applications encompass both theoretical and experimental aspects. From a computational standpoint, the diversity of dust particles in an astrophysical context implies a richness of models that need to be developed to calculate the optical forces. While exact electromagnetic solutions exist for calculating forces on model spherical particles [4], realistic dust grains possess complex and irregular shapes, as depicted in Fig. 3.1(a,d). In order to capture the scattering properties of real dust, several model particles have been proposed, including aggregates, stratified structures [173], agglomerate debris [174], and Gaussian random particles [175]. While these sophisticated models provide a closer representation of physical reality, the increased complexity in morphology necessitates higher computational power, thereby limiting the number of configurations that can be thoroughly explored numerically.

From an experimental perspective, optical tweezers (OT) have been predominantly utilized for trapping and manipulating micron-sized objects in liquid environments rather than in air or vacuum. The preference for liquid media stems from several inherent advantages. Firstly, liquid environments are compatible with living biological samples, facilitating the study of biological systems [4]. Secondly, the liquid medium dampens the motion of trapped particles, enhancing trapping stability and minimizing the effects of external perturbations and inertia on the particle dynamics [4, 163]. Thirdly, liquid media offer the advantage of suspending particles for extended periods, allowing specific single particles to be selected and trapped from a multitude.

In contrast, trapping stability in air or vacuum can be compromised by various external factors including airflows, acoustic shocks, thermal drift, mechanical vibrations, and the intensity noise of the trapping laser [176–178]. Air tweezers require launching a large number of particles, with passive trapping occurring as particles naturally approach the laser focus under the effect of gravity. This lack of control over particle selection, along with the difficulties in precise positioning and storing of trapped particles, represents significant drawbacks in air trapping setups [176, 178, 179]. Furthermore, in air OT, the numerical aperture of the focusing objective cannot exceed unity [180], leading to substantial scattering forces that might overcome trapping forces. The utilization of long working distance objectives and lenses with lower numerical apertures is often mandated in air trapping setups to prevent contamination of the objective lens. Additionally, since air is less efficient in dissipating heat compared to liquid, trapping absorbing particles in air may enhance photophoretic and convective forces. Such forces, generated by airflows, can often destabilize the trapped particle dynamics [176, 181, 182].

3.5.2 Recent progress

In recent years, significant efforts have been made to model optical forces on complex-shaped particles in order to accurately compute the forces applied to real particles in different position and orientations [4]. However, there is always a trade-off between calculation accuracy and speed. When studying particle dynamics in systems where inertia plays a role, such as in air or vacuum, the equations of motion must be integrated using very short time steps, and the optical force needs to be computed at each of these time steps [83]. While traditional methods of force calculation can be prohibitively slow for exploring these systems, recent advances in machine learning techniques have significantly enhanced the speed at which optical forces can be computed [88, 76]. This enhanced calculation speed is crucial for accurately modeling particles with complex shape. Furthermore, the improved calculation time opens up possibilities for real-time adjustments of light intensity and beam shape to optimize trapping conditions for specific particles in optical tweezers experiments. By rapidly adjusting these parameters based on the calculated optical forces, researchers can enhance the trapping efficiency and stability of a given particle in real-time.

From the experimental standpoint, various configurations have been developed to achieve stable three-dimensional trapping in air or vacuum. One approach is to use setups with counter-propagating beams, which help balance the effect of radiation pressure on the trapped particle [176, 183]. Another technique involves employing structured light beams, such as Bessel, hollow, or vortex beams, instead of Gaussian beams, either in horizontal or vertical configurations [176, 184–186, 179]. Furthermore, configurations having a single beam, such as the confocal-beam trap, combine the simplicity of a single beam and the robustness of a dual beam trap. In this configuration a spherical concave mirror reflects back the incident focused beam, forming a symmetric counter propagating beam [176, 184]. In addition to these techniques, the stability of a single beam trap can be increased also by a feedback device, that by controlling the laser power improves the trapping stability [187] and can even enable laser cooling of the particle motion [163].

3.5.3 Concluding remarks

Space tweezers have emerged as a valuable tool for the trapping and characterization of extraterrestrial particulate matter. Theoretical studies have utilized scattering theory to calculate optical forces on complex particles of astrophysical interest, simulating atmospheric and planetary environments. In parallel, significant progress has been made in the development of versatile, stable, and more compact setups that can be used to trap micro and nanoscopic particles in controlled laboratory experiments. These advancements have contributed to the advancement of space tweezers applications, providing a non-destructive, non-contact, and non-contaminating means of investigating extraterrestrial particles. The use of space tweezers opens up new possibilities for the study of space materials that are currently inaccessible using traditional instrumentation employed in space missions.

However, many different challenges still need to be faced . While perspectives for optical trapping and optical manipulation of particles in space and on planetary bodies surface might still need some key improvements in experimental setups, applications in curation facilities designed for the uncontaminated handling and preliminary characterization of extra-terrestrial samples returned by space probes appear at hand.

Chapter 4

Optically driven Janus micro engine with full Orbital motion control

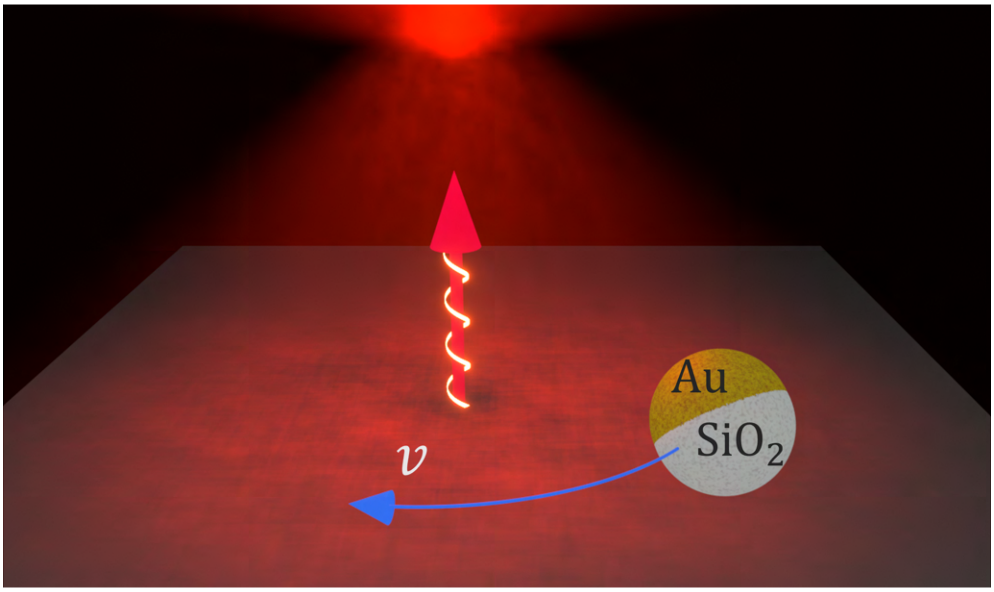

Microengines are poised to revolutionize nanotechnology, microfluidics, and nanomedicine, but achieving precise control over their dynamics has been a substantial obstacle. In this chapter, we introduce a microengine that overcomes this challenge by exploiting both optical and thermal effects to attain a high degree of controllability. The demonstrated enhanced flexibility in guiding microengines paves the way for their application in various domains, including microscale transport, sensing, and actuation. The accompanying image presents an artistic depiction of a Janus particle orbiting the center of a focused beam, exemplifying the innovative approaches discussed in this chapter to control microengine dynamics [188].

4.1 Introduction to light-driven microengines

Microengines have steadily gained popularity and become prevalent as effective tools for controlling processes on small scales [189]. Their ability to convert energy into active motion makes them essential for nanotechnology applications such as generating precise fluid flows in microfluidic chips [190–192], delivering drugs more efficiently in nanomedicine [193, 194, 69], or for environmental remediation [195, 196]. Janus particles [197], characterized by two distinct hemispheres with different physical properties, are the most widely used model system for microengines. Their inherently asymmetric design allows them to self-propel under various conditions. For instance, dielectric Janus particles can be designed with a metallic cap that generates a local, asymmetric heat profile under light exposure, resulting in its directed motion [198–202]. While microengines are able to overcome random thermal fluctuations and exhibit directed motion, the lack of control over their dynamics is a significant limitation for their broader application.

Light is one of the most efficient approaches to induce and control the motion of micro-engines [203–205]. Although non-optical electric [206] and magnetic fields [207] are also promising alternatives, light has distinct advantages such as high energy density, precise control over its position and time, and the ability to effectively transfer both linear and angular momentum [4]. Specifically, a highly focused laser beam can confine particles around the focal point through the exchange of momentum between light and particles, see Chapter 1. Once confined, by transferring momentum to the particle, there are two main strategies for turning the trapped particle into a rotating microengine. Firstly, spin [208–210] and/or orbital [211, 209, 30] angular momentum can be transferred to the particle, generating a polarization or phase-dependent torque that drives orbital rotations. The direction of rotation can be controlled by adjusting the polarization or phase gradients of the beam. Secondly, for asymmetric particles the scattering generates an optical torque [212, 213, 4, 56] where the direction of rotation is fixed by the scattering pattern (windmill effect) and determined by the shape of the particle. This effect has also been observed for metal-dielectric Janus particles [198, 214], highlighting the relevance of both light scattering and thermal effects [198].

Indeed, for light absorbing particles, not only momentum transfer but also energy absorption and consequent heating plays a key role in their dynamics, giving rise to more complex behaviours [215, 216, 201, 200, 198, 217, 192, 199, 218, 219, 18]. Because of the combination of optical and thermal effects, microengines can show elevator-like motion [200], elliptical [218], trochoidal [199] and circular orbits [198, 217, 192, 18], reach high rotation velocities [216], and present reconfigurable assemblies of multiple particles [220]. This shows that the integration of optical and thermal effects can induce a diverse range of dynamic behaviours. However, the controllability over these dynamics is very limited. For instance, unless the beam is continuously repositioned [215], the direction of rotation is either fixed by a previously designed geometry of the particle [216] or is erratic and influenced by random thermal fluctuations [217, 192, 198, 218]. Thus, a more sophisticated scheme is required to simultaneously manipulate the direction of rotation and the angular velocity in order to enhance the control of microengines.

In this chapter, we combine the precise control obtainable via optical forces with the strong driving forces of thermal effects to realize a microengine that allows simultaneous control of its speed, radius, and direction of rotation using a single beam of light. Specifically, we investigate a gold-silica Janus particle trapped by a linearly polarized Gaussian beam at a distance from the beam center where the opposing optical and thermal forces balance. By employing circularly polarized light, the transfer of the light spin angular momentum to the particle induces a tilt in the particle orientation. This tilt breaks the symmetry between the optical and thermal forces acting on the particle, leading to simultaneous rotations around the beam axis and around the particle axis (the particle rotates with the gold side always pointing inwards). We control the particle direction of rotation and angular velocity by tuning the beam ellipticity, showing that transitions between rotational and stationary states can be achieved within the same system. The experimental results are in agreement with an extended geometrical optics phenomenological model that also considers the polarization of the light beam and enables the calculation of the optical power absorbed in the particle cap. Our findings delve into the complexities of light-matter interactions in thermally driven microengines, presenting new insights and paving the way for enhanced control and manipulation in the field of nanotechnology.

4.2 Experimental realization

In this chapter, we investigate a microengine driven by both optical and thermal effects and whose motion we can precisely control by adjusting the power and polarization of the incident light beam. The microengine consists of a gold-capped silica Janus particle fabricated by sputtering a 10 nm-thick gold layer on top of a $3\,\mu$m diameter silica particle (Fig. 4.1(b)). The gold facet of the particle is optically thin enough not to significantly alter its optical properties and, consequently, its trapping capabilities. However, it is thick enough to induce thermal temperature gradients under light illumination (see Methods-Numerical Model). The beam shines from below (red arrow in Fig. 4.1(a)) and the focal spot is located at a distance $h = 8\,\mu$m above the particle (bright spot at the top of Fig. 4.1(a)). When the beam is circularly polarized (white spiral in Fig. 4.1(a)), the Janus particle performs orbital rotations at almost constant speed v around the center or the beam. The particle motion is recorded via digital video microscopy at 20 fps and tracked with customized Python routines. During its motion, the gold-cap always faces inwards (vector $\vec{n}$ pointing away from the cap in Fig. 4.1) and in the presence of circular polarization is misaligned (θ) with the local Poynting vector ($\vec{S}$) of the laser beam, see angle θ between the xy-projections of $\vec{n}$ and $\vec{S}$ (yellow and green dashed lines respectively). We observe this behaviour for various distances between particle and focal spot in the range $6 \leq h \leq 10\,\mu$m, whereas the particle can not be trapped for $h \leq 6\,\mu$m or does not rotate for $h \geq 10\,\mu$m. We find that the microengine is driven by both optical and thermal effects, and can be precisely controlled by adjusting the power and polarization of the incident light beam. Through both experimental and numerical analysis, we explore the dynamics of the microengine under varying light power and polarization conditions.

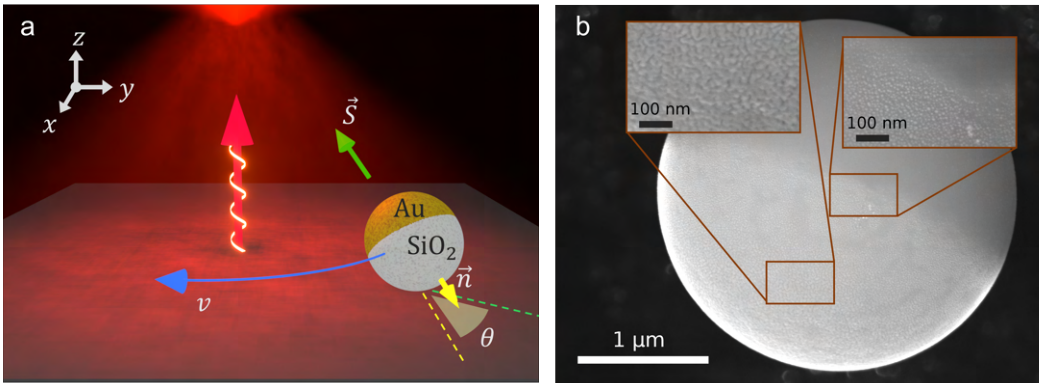

Fig. 4.1 Orbital motion of Janus particle under circularly polarized light. a) Schematic of the orbital motion of a gold-capped Janus particle made of SiO_2 under a circularly polarized focused beam (red arrow with white spiral illustrating the direction and polarization of the light beam). The particle is constantly rotating at speed v (blue arrow) around the center of the beam $8\,\mu$m below its focal point (red spot on the top). The particle orientation is sligthly tilted at angle θ, which indicates the misalignment between the xy-projections of the cap orientation (yellow arrow, $\vec{n}$) and the local Poynting vector (green arrow, $\vec{S}$). b) SEM images of the fabricated Janus particles. Insets show specific regions of the particle, where the left inset show deposited gold layer and the right inset the transition from the gold cap to the SiO_2 particle. Image taken from [188].

4.2.1 Motion as a function of laser power

When the light is circularly polarized, the Janus particle performs continuous circular orbits (Fig. 4.2(a)). Upon increasing the power of the light beam we observe that both the orbital radius (ρ) and the confinement of the particle are increasing (Fig. 4.2(b)). At low power ($P = 6\,$mW) the Janus particle is mostly located in close proximity to the beam center ($\rho = 2.4 \pm 0.6\,\mu$m) and the distribution of radial positions has a large standard deviation. At intermediate powers ($P = 16\,\mathrm{mW}$) the radius of motion increases and the radial confinement is enhanced, resulting in a narrower radial distribution. The average radial position peaks at the maximum power of our laser $P = 34\,\mathrm{mW}$ with $\rho = 7.5 \pm 0.4\,\mu\mathrm{m}$, showing a well defined circular trajectory. Note that a fundamental difference between our experiment and other works on active colloids in optical potentials [204, 221] lays on the fact that in our case the orientation of the particle does depend on its position (gold always faces inwards).

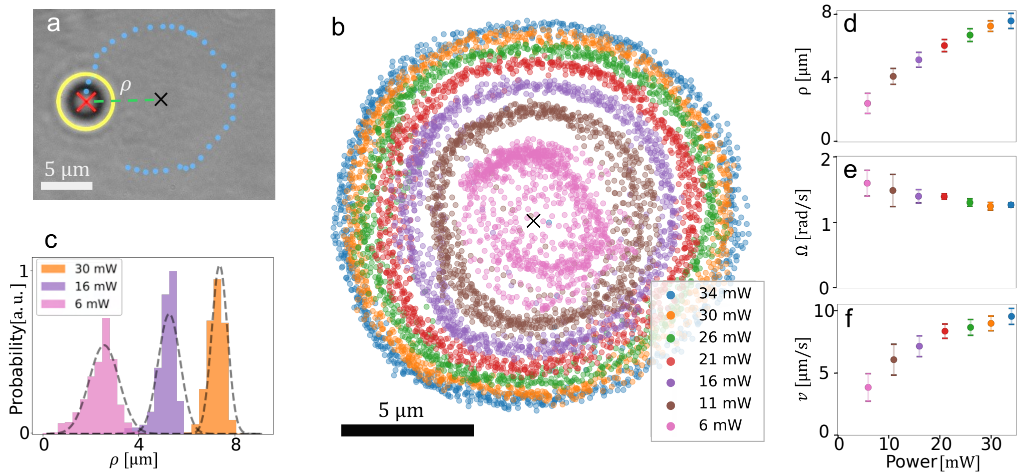

Fig. 4.2 Janus particle motion dependence on laser power. a) Bright-field image of a tracked Janus particle (yellow outline) with center-of-mass position (red cross) rotating around the center of the beam (marked by black cross) at a distance ρ (green dashed line) with its circular trajectory (blue dotted line) during 3.5 s. b) Recorded positions of the particle orbiting around the center of the beam (black cross) for different incident powers P for 50 s-long trajectories. c) Probability distribution of ρ for three different powers ($P = 6, 16$ and $30\,\mathrm{mW}$) and fitted with a Gaussian function (dashed grey line). From the standard deviation of the radii distribution we can quantify the particle's radial confinement. d) Average radius ρ, e) average angular velocity Ω, and f) average linear velocity v of the trajectories as a function of laser power. The error bars correspond to the standard deviation for 5 measurements of 10 s each. Image taken from [188].

Next, we fully characterize the dependence of the particle motion on laser power for its change in orbital radius ρ, angular speed Ω, and linear speed v. We find that ρ increases non-linearly reaching the maximum radius at the maximum power ($P = 34\,\mathrm{mW}$, Fig. 4.2(d)). Although Ω decreases slightly (between 1.6 ± 0.2 and $1.3 \pm 0.1\,\mathrm{rad/s}$, Fig. 4.2(e)) the linear speed v increases significantly (from 3.8 ± 1.2 to $9.5 \pm 0.6\,\mu\mathrm{m/s}$) with increasing laser power (Fig. 4.2(f)). While the decrease in angular velocity with laser power is modest, the strong power dependence of the radial distance is ultimately responsible for the observed increase in linear velocity.

Similarly shaped orbits such as the ones exhibited by our proposed microengine have been previously reported in the literature [198, 200, 217]. However, our microengine offers distinct advantages in terms of controllability. While previous systems with Janus particles in water showed sudden jumps in equilibrium position when varying laser power for circular orbits [198] as well as for elevator-like motion [200] our microengine exhibits a smooth dependence of the orbital radius ρ with power. A similar power dependence of ρ has been reported for optically heated spheres at a water-air interface (ranging between 3 and 11 μm) [217]. Moreover, an advantage of our system is the presence of continuous and predictable rotations, which contrasts with the orbiting microengines reported in previous studies [217, 198] that rotate in unpredictable directions and can change the direction of rotation randomly. Interestingly, a comparable behavior has been reported for a silica particle optically trapped in vacuum [18] using transverse spin forces [222, 170] instead of a combination between thermal forces and transfer of angular momentum. They found that an increase in power results in an increase in the value of ρ (ranging between 0.2 and 1.4, μm) and enhanced radial confinement of the particle [18]. Similarly to our system, they also obtain a better defined rotation frequency for higher powers. We can achieve this not only by increasing the power but also by increasing the ellipticity, see Fig. 4.3 showing the analysis of the power spectral density of the particle trajectories. However, unlike our system, V. Svack et al. reported an increase of the angular velocity of the particle with power, exploiting the low-viscosity environment to achieve rotation frequencies of up to 15 kHz [18].

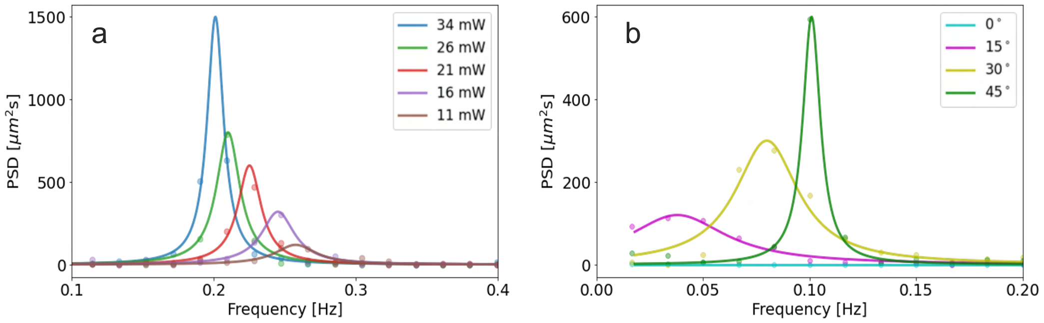

Fig. 4.3 Power spectral density of the trajectories of the microengine. a) Light circularly polarized and with different powers. b) Light with constant power (34 mW) and different degrees of ellipticity of the incoming light.

4.2.2 Motion as a function of light polarization

Transfer of angular momentum can induce rotation of particles around their own axis [210]. In our experiment, circularly polarized light induces a spinning rotation of the particle around its z-axis that breaks the symmetry between optical and thermal forces acting on it and thus induces its directional orbital motion. This motion can be stopped or reversed by changing the polarization state of the light, see Fig. 4.4(a-c). When exposed to linearly polarized light, the particle remains confined to a specific distance ρ from the center of the beam where it diffuses randomly (around the circle of radius ρ) due to Brownian motion, see Fig. 4.4(b). Note that for linearly polarized light, the only acting torque is the one that orients the particle such that its gold cap ($\vec{n}$) is aligned along the local Poynting vector of the beam impinging on the particle ($\vec{S}$), see Fig. 4.4(a-c) and Fig. 4.5, similarly to what has been reported for a Janus particle [200]. This alignment prevents random rotational diffusion of the particle orientation and distinguishes our microengine from other examples in the literature where the particle rotates in random orientations [198, 217].

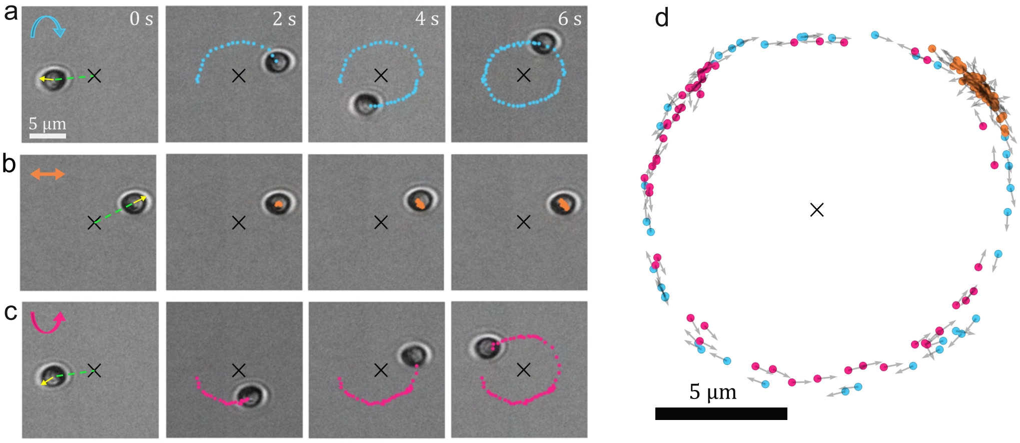

Fig. 4.4 Motion of a Janus particle as a function of light polarization. a-c) The particle is shown at $t = 0, 2, 4$ and 6 s, the plotted points correspond to previous positions at 0.1 seconds intervals. The black cross indicates the centre of the beam and the yellow arrows in the initial frame represent the orientation vector $\vec{n}$ as illustrated in Fig. 4.1(a). The green dashed lines show the direction of the local Poynting vector. a) Light circularly polarized clockwise induces clockwise rotation with more than a full orbit completed after 6 s. b) Light linearly polarized keeps the particle at the same radius difussing with no directed motion. c) Light circularly polarized anticlockwise induces anticlockwise rotation with almost a full orbit completed after 6 s. d) Positions (points) and direction of motion (arrows) of the particle for linearly polarized light (orange), circularly polarized light in clockwise (blue), and anticlockwise directions (pink). Positions are plotted every second for a 60 s-long trajectory. Image taken from [188].

When applying circularly polarized light, the direction of rotation is entirely determined by the polarization direction of the circularly polarized light, and can be reversed by switching between clockwise and anticlockwise circular polarization (Figs. 4.4(a,c)). From the recorded video frames in Figs. 4.4(a-c) we observe the gold-coated side of the Janus particle (the darkest region in transmission microscopy) facing always radially inwards to the center of the beam (yellow arrows represent the orientation vector $\vec{n}$ in Fig. 4.1(a)). Even though the thin gold coating (10 nm) does not offer sufficient contrast to precisely quantify the exact orientation of the Janus particle, note that for circular polarization the orientation vector $\vec{n}$ is not aligned with the position vector (green dashed line in Figs. 4.4(a,c)) but is slightly tilted, which results in the breaking of symmetry that generates the tangential force ($\mathbf{F}_{\text{tan}}$) responsible for its motion. See Fig. 4.5 for a more detailed view of the gold-coated side and the non-coated side of the Janus particle.

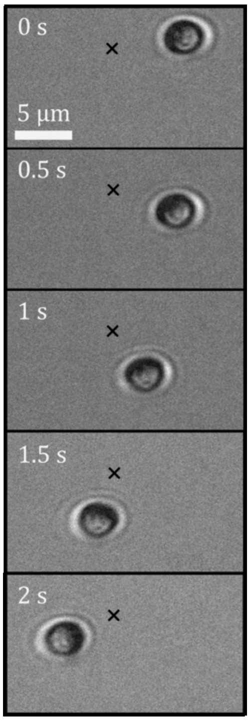

Fig. 4.5 Orientation of the Janus particle under circularly polarized light. Janus particle rotating under light circularly polarized clockwise. The particle is shown at $t = 0, 0.5, 1, 1.5$ and 2 s. The black cross indicates the centre of the beam. The gold-coated side of the Janus particle (the darkest region in transmission microscopy) faces always radially inwards to the center of the beam while the silica particle (lightest region) faces outwards. Image adapted from [188].

Although the direction of rotation of the particle is determined by the polarization of the beam, the orbit and radius of motion are independent of polarization and are solely determined by the power (as discussed in the previous section). Fig. 4.4(d) shows the particle positions and the direction of motion for 60 s trajectories (each point represents 1 s time steps). Pink and blue points represent different senses of circularly polarized light whereas orange points indicate linearly polarized light. The particle is located at a distance ρ of around 7 μm and eventually closes a loop in approximately 6 s. The erratic Brownian motion observed for linear polarization (orange points in the upper right corner) where the particle remains at the same location and diffusing due to Brownian motion, stands in contrast to the well-defined directional motion observed for circular polarization (blue and pink points).

Additional control can be gained by also adjusting the velocity and direction of rotation using elliptical polarization, as demonstrated in Fig. 4.6. We have previously shown that changing laser power affects, both, the microengine's velocity and the radius of rotation, see Fig. 4.2(d,f). However, adjusting the ellipticity of the light allows further velocity tuning without affecting the radius. Completely circularly polarized light yields the highest values of the angular velocity (Ω), see $\phi = \pm\pi/4$ in Fig. 4.6, where ϕ is the angle between the polarization plane of the linearly polarized and the fast axis of the $\lambda/4$ wave plate. Furthermore, the experimental velocities match the theoretical dependence on $\sin(2\phi)$, see Fig. 4.6. Note that the standard deviations of the angular velocities are three times larger for intermediate elliptical polarizations than for circular polarization. We attribute this to asymmetries in the beam profile profile (arising from misalignment or from the highly focused nature of the beam [223, 224]) that create energy barriers that are more difficult to overcome when the tangential force $\mathbf{F}_{\mathrm{tan}}$ is lower, resulting in a less homogeneous motion. The difference (30%) between the experimental maximum velocity for clockwise and anticlockwise polarization is likely due to differences in the transmission of optical elements such as mirrors and dichroic beam splitters that result in slightly lower power for clockwise polarization.

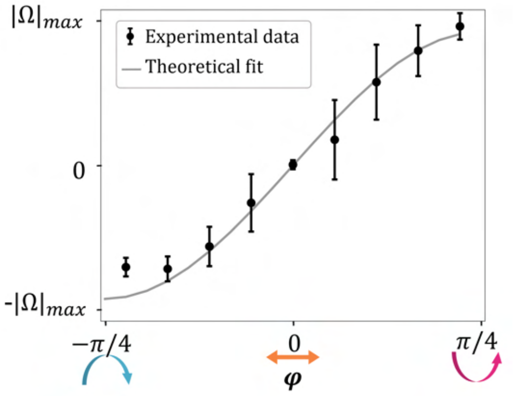

Fig. 4.6 Angular velocity as a function of the ellipticity of the light. The solid line indicates the theoretical dependence on $\sin(2\phi)$. The experimental error bars correspond to the standard deviation for 5 measurements of 10 seconds each. Image taken from [188].

Although there exist other microengines capable of producing closed orbits [217, 198, 192], they are unable to be stopped at a specific location within their trajectory without minimizing the power and returning to the center of the beam. Our microengine, in contrast, offers complete flexibility in terms of orbital direction, the ability to halt at any distance, and even reverse its trajectory, therefore setting a new standard in controlling microsystems that are typically dominated by random fluctuations. The precision of control demonstrated by our proposed microengine, achieved through the ellipticity of the incoming beam, is only comparable to microengines that rely on transferring angular momentum between particles and light [225, 211, 209]. However, our microengine distinguishes itself by enabling control at various distances from the beam center, rather than being limited to a single focal point.

4.3 Numerical study

The presented micro engine is governed by a series of intricate physical phenomena. While these mechanisms possess a high level of complexity, our objective is to establish a comprehensive understanding of the driving mechanism of the system through the utilization of a simplified phenomenological model. This model incorporates three key elements. Firstly, the mechanical effects of light, which serve to attract the particle towards the center and maintain its orientation. Secondly, the light-induced heating of the particle that results in a propelling swimming force from the hot region (gold cap) to the cold region (silica part). Lastly, polarization-dependent torques that change the orientation of the particle when the light is circularly polarized. Even though our simplified phenomenological model comes with some limitations (not considering the effect of the surface in the hydrodynamics flow, assuming the gold coating to be homogeneous, not considering possible plasmonic modes...), see Methods-Numerical Model, it effectively captures the fundamental aspects of the experimentally studied microengine.

The model, by considering the geometrical optics approximation [2], computes both the exchange of momentum between light and particle (generating optical forces [4]) and the absorption and consequent heating of the gold cap (generating thermal forces [226]). While the optical force draws the particle towards the center, the thermal force, caused by the difference in temperature between the gold (inner part) and silica (outer part), pushes the particle away. The combined effect of the opposing forces creates a force that cancels out at a distance ρ, see Fig. 4.7(a). Furthermore, the total force has a negative slope at the point where the opposing optical and thermal forces are balanced, see the inset of Fig. 4.7(a), leading to the formation of a stable stationary point. If the particle moves further away, it will experience a negative force that will attract the particle back towards the stable stationary position. On the contrary, if the particle approaches the center, it will experience a positive force pushing it away. For small radial displacements from the stationary position, the total radial force F_{tot} can be approximated as a Hookean force ($F_{\text{tot}} = -k_\rho \rho$), with the stiffness k_ρ being determined by the slope of the force in the proximity of the stationary point, see dashed red line in Fig. 4.7(a).

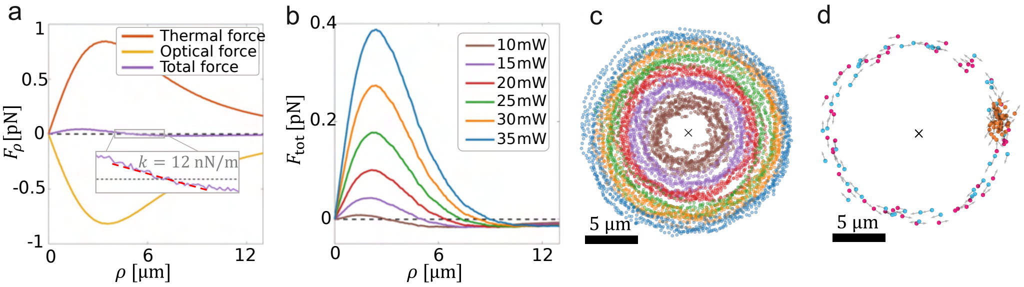

Fig. 4.7 Numerical study of the microengine. a) Thermal, optical, and total force in the radial direction as a function of the radius for a power of 15 mW. The stationary point is at $\rho = 5.1 \pm 0.6\,\mu$m and the stiffness is 12 nN/m. b) Total force exerted on the particle as a function of ρ for different powers. Both the stationary position and the stiffness increase with the power. c) Simulation of the dynamics of the Janus particle for a 50 seconds trajectory when illuminated with different powers and d) simulation of the dynamics of the particle under anticlockwise circularly polarized light (pink), linearly polarized light (orange) and clockwise circularly polarized light (blue). The black crosses represent the center of the beam. The parameters of the plots c) and d) are identical to the ones of Fig. 4.2 and Fig. 4.4. Image taken from [188].

We find that our numerical analysis is consistent with our experimental results demonstrating that the orbital radius of the Janus particle increases with power, see Fig. 4.7(b). While the forces are increasing with power, their dependence is non-linear thereby shifting the stationary position. If, both optical and thermal forces grew linearly with the power, the stiffness would increase linearly but the stationary position wouldn't shift, as the forces would still balance at the same point, which is in contrast to experimental observations. In our model, optical forces are considered to scale linearly with the power whereas the thermal force introduces non-linearities, see Eq.4.4 and Eq.4.9. In our simulations, we observe a change in stationary position from $3.0 \pm 0.7\,\mu$m at 10 mW to $9.0 \pm 0.5\,\mu$m at 35 mW (experiments show ranges from 2.4 ± 0.6 to $7.5 \pm 0.4\,\mu$m). Higher powers push the particle further away while increasing its radial confinement, consistently with experimental observations.

Under circularly polarized light, the transfer of spin angular momentum causes the particle to change orientation around its own z-axis. The force acting in the tangential direction $\mathbf{F}_{\text{tan}}$ is due to the symmetry breaking between the optical and thermal forces (the optical force pulling the particle towards the center of the beam and the thermal force pushing it from the gold to the silica part). More precisely, in the presence of circularly polarized

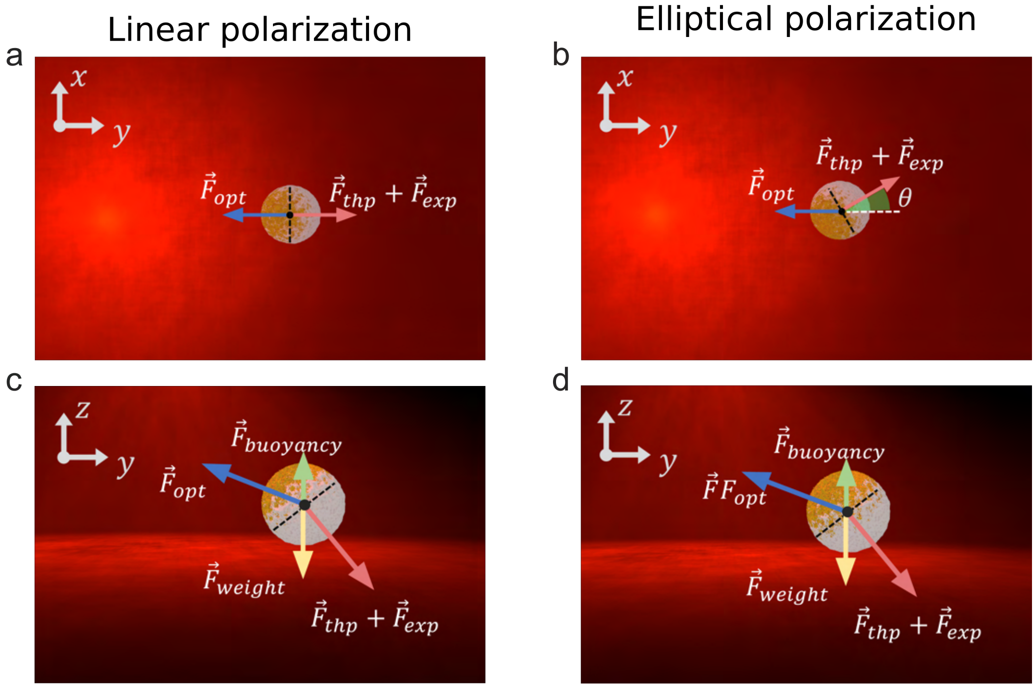

Fig. 4.8 Forces acting on the Janus particle under different laser polarizations. Forces acting on the Janus particle under linearly polarized light (a,c) and elliptically polarized light (b,d). The optical force acting on the particle can be decomposed into two components: a gradient part that directs the particle towards the center, and a scattering part in the z direction, which pushes the particle away from the cover slip. In (b), θ is the angle between the direction of the optical force (towards the center of the beam) and the direction of the thermal force (from gold to silica) that gives rise to the tangential force that drives the orbital motion. Image taken from [188].

light, the orientation of the cap $\vec{n}$ does not exactly align with the local Poynting vector $\vec{S}$, but is tilted. This tilt is due to an additional small azimuthal rotation by the transfer of angular momentum, which breaks the mirror symmetry of the configuration. This creates a steady tangential force $\mathbf{F}_{\text{tan}}$ that keeps the particle rotating in its circular orbit. As we observe continuous rotations, we know that the tangential component of the thermal force should be equal to the drag force: $F_{\text{tan}} = \gamma v$, where γ is the viscous coefficient and v is the speed of the particle (we obtain the maximum value of F_{tan} for maximum power and circular polarization being approximately 0.2pN). The numerical model allows us to also determine the radial component of the thermal force (as the radius remains constant, it must have the same magnitude and opposite direction to the optical force which in this situation is approximately 1pN). Knowing both, radial and tangential components of the thermal force, we can estimate the required tilting θ of the particle around the vertical direction (due to the torque applied by the circularly polarized light) to give the expected tangential force. We find this angle θ to be around 10 degrees for circularly polarized light. On the other hand, when the polarization is linear (see Fig. 4.8), the cap is aligned with the local Poynting vector such that the absence of the tangential force does not induce steady rotation but yields an equilibrium distance ρ at which the particle is confined.

Our Brownian dynamics simulations (see Methods-Numerical Model) also confirm that the particle remains confined at a given radius ρ that increases with power from $3.3 \pm 0.9\,\mu$m at 10 mW up to $9.1 \pm 0.6\,\mu$m at 35 mW, see Fig. 4.7(c), which is consistent with both experimental and theoretical results. Additionally, the simulations verify that the radial confinement does also depend on the power, with the trajectory for higher powers being less spread than that for lower ones, see Fig. 4.7(c). In Fig. 4.7(d) we show simulations where different ellipticities of the incoming light such as in experiments have been considered. In particular, we plot the results for circularly polarized light in both orientations (blue and pink points) and for linearly polarized light (orange points). As for our experimental results (see Fig. 4.4(d)), in the case of linear polarization the particle remains around the same location and only diffuses, which stands in contrast to the well-defined directional motion observed for circular polarization.

4.4 Methods

4.4.1 Janus particles

The fabrication of the Janus particles (diameter $3\,\mu$m) made of silica (SiO_2) and half coated with gold (Au) splits into three different steps. The first one consists of obtaining a crystalline monolayer of silica spheres on the glass surface. Starting from a solution of silica spheres in water, we deposit the droplet on the glass, and when the solvent evaporates we obtain a monolayer of particles on the substrate. We find the best structures when covering the substrate with a Petri-dish and keeping it at a temperature of 19°C until the sample dries. The second step consists of coating one half of the particles' surface with a 10-nm thick layer of gold. For this, we employ the thermal evaporation technique, which evaporates the metal and condenses it on the particles surface at high vacuum conditions. To improve the adhesion of gold to silica, we added a 2 nm layer of Titanium before adding gold. Third and last, to release the particles in solution, we immerse the substrate in water and sonicate for 5 seconds (SONICA, 1200M). SEM micrographs were collected by a Quanta 450 (FEI, Hillsboro, OR, USA) with a large-field detector (LFD) and an accelerating voltage of 20 kV in high vacuum (1^{-6} mbar).

4.4.2 Experimental setup

To prepare the sample chamber, a small amount of Janus particles in aqueous suspension ($15-20\,\mu$l) is drop casted on a clean microscope slide and then covered with a coverslip. The obtained chamber is sealed with nail polish to avoid evaporation during measurements. The light source for the optical tweezers is a laser diode source (Thorlabs DL8142-201) at 830 nm wavelength. After passing through a couple of anamorphic prisms and an optical isolator, the laser beam is expanded to overfill the back aperture of a high numerical aperture objective (Olympus, Uplan FLN 100X, NA=1.3), aiming at obtaining a diffraction-limited spot approximately 600 nm in diameter. Laser power at the objective is varied in the range between 5 and 35 mW. A $\lambda/4$ wave plate, placed in the beam path, is used to control the light polarization state. The relative position between the chamber and the focus of the beam is controlled using a piezoelectric stage (Mad City Labs NANO-LP200). The focal spot is located $8\,\mu$m above the substrate while the motion of the particle takes place directly on top of the substrate. The particle images are taken in transmission with a CCD camera and are calibrated by imaging a microscope slide ruler. Tracking of the particle dynamics follows standardized digital video microscopy techniques and has been implemented in home-made Python codes. See Fig. 4.9 for a schematic of the experimental set up.

4.4.3 Numerical model

The interaction of the Janus particle with the focused Gaussian optical beam is described in the geometrical optics approximation [2, 76]: the beam is represented by an appropriate set of rays that, impinging on the Janus particle surface, are reflected, transmitted, and, when

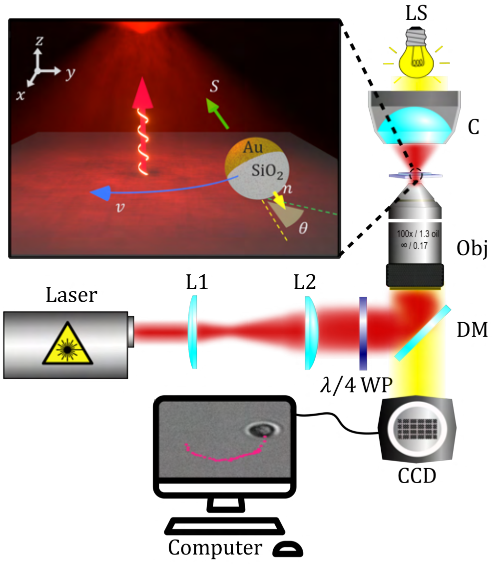

Fig. 4.9 Schematic of the experimental set up. The schematic includes the laser source, the two lenses (L1 and L2) that expand the beam, the $\lambda/4$ waveplate, the dicroic mirror (DM) that reflects the beam into the objective (Obj), the condenser (C), the illumination source (LS), and the computer that analyzes the images. Image taken from [188].

hitting the gold-coated spherical cap, also partially absorbed, see Fig. 4.10. While each ray is undergoing this infinite series of scattering events, it exchanges linear and angular momentum with the particle and therefore applies an optical force and torque. Additionally, the metallic cap absorbs some of the incident light thereby increasing its temperature locally around the stationary point $\approx 5-10$ K. Given that the gold cap is largely continuous and gold exhibits excellent thermal conductivity, we assume the gold cap being isothermal. As the particle is immersed in solution, the temperature of the water in close proximity to the cap increases too: this asymmetry induces a temperature gradient across the particle. As fluids typically move from cold to hot regions, the particle experiences a slip flow in the opposite direction, inducing thermophoretic ($\mathbf{F}_{\text{thp}}$) motion of the particle [202]. Moreover, the temperature increase in the volume of water close to the particle induces a volume expansion of the water ($\mathbf{F}_{\text{exp}}$). This causes an unbalanced force towards the non-expanding volume region (i.e. the "cold" side of the Janus particle). In practice, the particle feels a force proportional to the increased water volume, propelling the particle towards its cold end, see Fig. 4.11.

Our experimental observations regarding the orientation of the particle, as depicted in Fig. 4.4(a-c) and Fig. 4.5, are in line with previous studies [200] and with symmetry arguments. Based on these findings, we make the assumption that for a Janus particle with a thin gold layer, the optical torque resulting from geometrical scattering stably orients the particle in a manner where its gold cap aligns with the local Poynting vector $\vec{S}$ of the beam

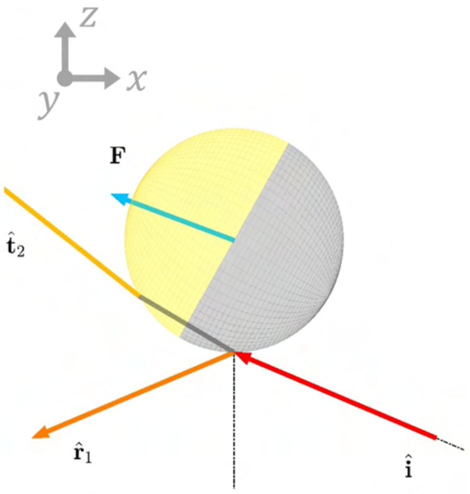

Fig. 4.10 Schematic of a ray impinging on a Janus particle. The ray $\hat{\mathbf{i}}$ reaches the particle and divides into a scattered ray $\hat{\mathbf{r}}_1$ and a transmitted ray $\hat{\mathbf{t}}_2$. The change in linear momentum results in an applied force on the particle $\mathbf{F}$. Image taken from [188].

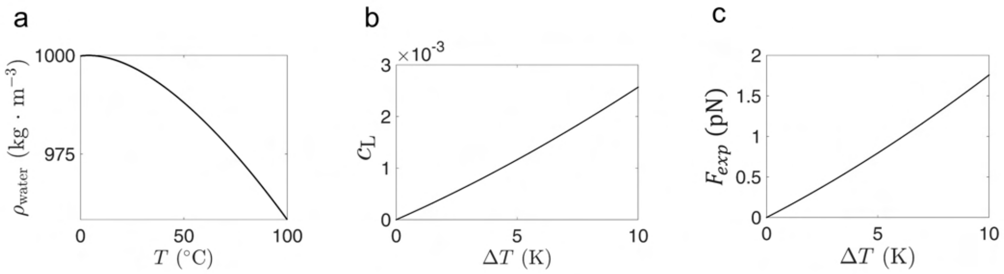

Fig. 4.11 Parameters as a function of temperature. Density of water (ρ_{water}), linear expansion coefficient of water (c_L) and volume expansion force (F_{exp}) as a function of temperature. Image taken from [188].

impinging on the particle, see Fig. 4.1(a). While our model assumes an isothermal gold cap, the presence of small isolated grains along the borders of the cap in combination with the inhomogeneous illumination induces a thermophoretic torque. This torque, similarly to the optical torque resulting from geometrical scattering, would act to align the gold cap with the local Poynting vector in the horizontal plane, thereby preserving radial symmetry. Although we did not explicitly incorporate this phenomenon into our model due to its complexity, we acknowledge its potential influence on the behavior of the system. Also, the combination of particle size ($3\,\mu$m) with the proximity to a planar boundary determines that the orientation of the particle is not very much affected by the Brownian noise, as the relaxation time of the rotational dynamics is significantly longer than the one in bulk in the order of magnitude of about 20 s. In our dynamics simulation, hence, we consider the degrees of freedom related to the position of the particle center only, the orientation in each point is defined by the local Poynting vector $\vec{S}$, Fig. 4.12.

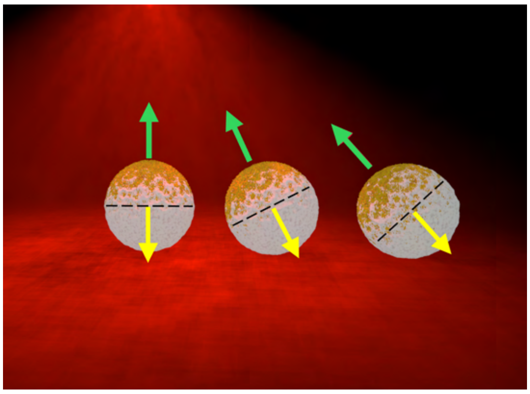

Fig. 4.12 Orientation of the Janus particle for different radial positions under linearly polarized light. The local Poynting vector of the focused beam ($\vec{S}$, in green) is perpendicular toplane that contains the border between gold and silica and goes in the opposite direction to the orientation vector ($\vec{n}$, in yellow). Image taken from [188].

From our main experimental observations we saw that elliptically polarized light induces orbital motion of the particle around the beam axis. We can simulate this by introducing a polarization dependent torque in our model. The Brownian dynamics equations for our particle, transposed already in the finite difference formalism, read as:

$$\begin{cases} \Delta\rho = \dfrac{D_{\mathrm{transl}}}{k_{\mathrm{B}}T} F_{\rho,\mathrm{tot}}\,\Delta t + \sqrt{2D_{\mathrm{transl}}\,\Delta t}\, W_{\rho}, \\[2ex] \Delta s = \dfrac{D_{\mathrm{transl}}}{k_{\mathrm{B}}T} F_{s,\mathrm{tot}}\,\Delta t + \sqrt{2D_{\mathrm{transl}}\,\Delta t}\, W_{s}, \\[2ex] \Delta\psi = \dfrac{D_{\mathrm{rot}}}{k_{\mathrm{B}}T} T_{z,\mathrm{pol}}\,\Delta t, \end{cases} \tag{4.1}$$

where ρ is the radial coordinate from the center of the beam and $\vec{S}$ is the coordinate in the tangential direction, oriented in the sense of positive angles (i.e., obtained from $\hat{\rho}$ and the direction of the beam propagation axis $\hat{\mathbf{z}}$ via $\hat{\mathbf{s}} = \hat{\mathbf{z}} \times \hat{\rho}$), and ψ is the azimuthal angle describing the orientation vector of the particle in the standard lab reference frame with basis unit vectors: $\hat{\mathbf{x}}$, $\hat{\mathbf{y}}$, $\hat{\mathbf{z}}$.

The term $F_{\rho,\mathrm{tot}}$ is the total force component along the radial direction $\hat{\rho}$, $F_{s,\mathrm{tot}}$ is the component along the tangential direction $\hat{\mathbf{s}}$, and $T_{z,\mathrm{pol}}$ is the torque along the beam propagation axis direction $\hat{\mathbf{z}}$ due to the amount of circular polarization of the light. The diffusion constants are D_{transl} and D_{rot}, which are related to the components $D_{||}$, $D_{\mathrm{rot},\perp}$ of the diffusion matrix of a spherical particle[219]. W_ρ and W_s are Gaussian white noise terms related to the random Brownian fluctuations. Both terms have zero mean and unit variance.

The total force is calculated as:

$$\mathbf{F}_{\mathrm{tot}} = \mathbf{F}_{\mathrm{opt}} + \mathbf{F}_{\mathrm{thph}} + \mathbf{F}_{\mathrm{exp}} + \mathbf{F}_{\mathrm{weight}} + \mathbf{F}_{\mathrm{buoyancy}} + \mathbf{F}_{\mathrm{int}} \tag{4.2}$$

where $\mathbf{F}_{\mathrm{opt}}$ is the optical force due to the scattering of the rays on the particles, $\mathbf{F}_{\mathrm{thph}}$ is the thermophoretic force due to the slip flow of the thin layer of fluid in the proximity of the particle surface induced by the temperature gradient along the particle diameter (direction metallic cap-uncoated end), $\mathbf{F}_{\mathrm{exp}}$ is the force due to the volume expansion of the water caused by the temperature increase in the region near the cap, $\mathbf{F}_{\mathrm{weight}}$ is the weight of the particle, $\mathbf{F}_{\mathrm{buoyancy}}$ is the upwards force that the fluid applies to the particle because of its mass density, and $\mathbf{F}_{\mathrm{int}}$ is the interaction force with the bottom slide, that we assume to be short range and repulsive, representing a colloidal electrostatic interaction which decays exponentially with increasing distance between the particle and bottom slide preventing sticking. As the cap is oriented in the direction of the local Poynting vector, i.e., the coated cap faces the beam focus, while the uncoated particle hemisphere faces downwards and thus the bottom slide, the vertical component of the sum of all forces except for the electrostatic interaction with the substrate is directed downwards. Therefore, we assume that the substrate must always compensate the vertical forces with the right amount of repulsion, and the particle always remains close to the substrate at a given minimal distance from it ($\approx 50\,\mathrm{nm}$). For this reason, we do not include an explicit equation for the particle position in the vertical direction, see Fig. 4.8 for a schematic of the direction of the forces under different polarization conditions. Note that the presence of a surface, such as a bottom slide, can alter the hydrodynamic flows and impact the propulsion of the particle [227]. Although this factor may have a significant role in certain systems and the interaction between particles, we did not account for this effect in our numerical model. Instead, we deliberately developed the simplest numerical model that accurately captures the experimental observations.

The expression for the different forces are given here below. The optical force is calculated in the standard way from the scattering, summing the contribution of the force due to the single rays [2]:

$$\mathbf{F}_{\mathrm{opt}} = \sum_m \mathbf{F}_{\mathrm{ray}}^{(m)} \tag{4.3}$$

with

$$\mathbf{F}_{\mathrm{ray}} = \frac{n_{\mathrm{m}} P_{\mathrm{i}}}{c}\hat{\mathbf{i}} - \frac{n_{\mathrm{m}} P_{\mathrm{r}}^{(1)}}{c}\hat{\mathbf{r}}_1 - \sum_{j=2}^{\infty} \frac{n_{\mathrm{m}} P_{\mathrm{t}}^{(j)}}{c}\hat{\mathbf{t}}_j, \tag{4.4}$$

The temperature increase is calculated while calculating the scattering, calculating the power absorbed by each single ray and summing it:

$$P_{\mathrm{abs}} = \sum_m \mathbf{P}_{\mathrm{cap,ray}}^{(m)} \tag{4.5}$$

If we consider the cap isothermal, the temperature increase ΔT_{cap} is

$$\Delta T_{cap} = \frac{P_{\mathrm{abs}}}{(2\pi + 4)\kappa_{\mathrm{m}} R}, \tag{4.6}$$

where κ_{m} is the thermal conductivity of the medium and we can define a temperature gradient across the particle given by:

$$\nabla T = \frac{\Delta T_{cap}}{\pi R}. \tag{4.7}$$

The thermophoretic velocity is expressed as $v_{\mathrm{ph}} = -D_{\mathrm{T}} \nabla T$ where D_{T} is the thermal diffusion coefficient [226]. From v_{ph} we obtain $F_{\mathrm{thph}} = \frac{k_{\mathrm{B}} T}{D_{\mathrm{transl}}} v_{\mathrm{ph}}$. This force is assumed to push the particle in the $\vec{n}$ direction, from its coated cap to its uncoated end.

The magnitude force related to the volume expansion of the water when the temperature is increased (F_{exp}) is modelled as follows. We estimate a linear expansion coefficient c_{L} for the water between the base temperature (T) and the increased value of the temperature

$(T+\Delta T)$ as:

$$c_\mathrm{L} = \frac{\rho_\mathrm{water}(T)}{\rho_\mathrm{water}(T+\Delta T)} - 1, \tag{4.8}$$

where $\rho_\mathrm{water}(T)$ indicates the mass density of water at temperature T and we write:

$$F_\mathrm{exp} = \alpha\, p_\mathrm{water}\, c_\mathrm{L} R^2, \tag{4.9}$$

where R is the radius of the particle, p_water is the hydrostatic pressure in the fluid, that we assume equal to the atmospheric pressure at sea level, and $\alpha = 0.003$ is a proportionality constant. This is a phenomenological, simplified model of the complex fluid dynamics occurring inside the fluid chamber, that are normally modelled using the Navier-Stokes equations. $\mathbf{F}_{exp}$ results from a force unbalance between the expanded water region (i.e., close to the gold cap) and the unexpanded water region (i.e., close to the silica half) and it is assumed to push the particle along the direction from its coated cap to its uncoated end.

The polarization torque is calculated summing the contribution of each ray impinging on the particle as:

$$T_\mathrm{pol} = \sum_m \mathbf{T}^{(m)}_\mathrm{pol,ray} \tag{4.10}$$

The contribution of each ray is modelled as proportional to the power absorbed on the first scattering event that involves the cap:

$$\mathbf{T}^{(m)}_\mathrm{pol,ray} = \sigma \frac{P^{(m)}_\mathrm{1,abs,ray}}{\omega} \hat{\mathbf{r}}^{(m)}_\mathrm{1,abs,ray} \tag{4.11}$$

In the equation above, $\omega = 2\pi\nu$ is the angular frequency of the optical wavelength used for the laser beam, σ is a parameter between -1 and 1 describing the amount of circular polarization transported by each ray (where 0 corresponds to linear polarization), $P^{(m)}_\mathrm{1,abs,ray}$ is the power that the m^th ray deposits on the cap the first time it hits the cap, and $\hat{\mathbf{r}}^{(m)}_\mathrm{1,abs,ray}$ is the direction of the m^th ray when this event happens.

4.5 Conclusions

In this study, we have introduced a highly controllable microengine by combining both optical and thermal effects. We demonstrated that a $3\,\mu$m gold-silica Janus particle can be confined at a specific distance from the center of a highly focused beam, with the gold side facing inwards. The balance between optical forces, which pull the particle towards the high intensity region, and thermal forces, which push it away from the same region, is responsible for this confinement. Remarkably, the stationary position can be fine-tuned by adjusting the beam power. Furthermore, we showed that circularly polarized light can transfer spin angular momentum from the light to the particle, breaking the mirror-symmetry of the system and inducing a moon-like rotation (orbital motion of the particle around the beam axis with the gold side towards the center of the beam). The speed and the orientation of this rotation can be precisely controlled by varying the ellipticity of the light. Our experimental findings have been validated by a phenomenological numerical model based on the geometrical optics approximation that matches our observations and provides further insights into the intrinsic properties of the system. Overall, the high degree of control we have achieved with this microengine opens up new possibilities in a wide range of applications, from microscale transport to sensing and actuation.

Chapter 5

Propulsion of capped elongated microparticles via optical forces

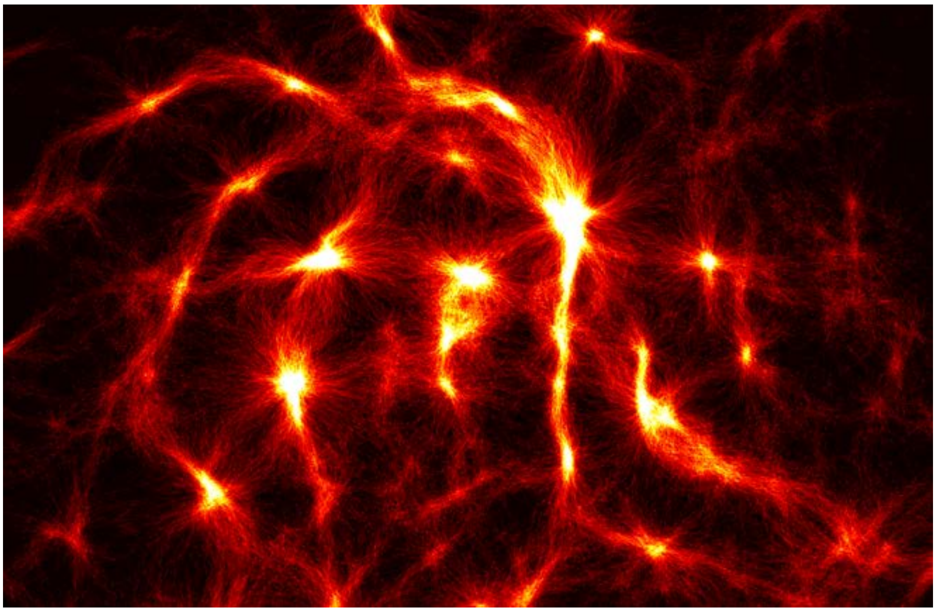

Optical forces can control and manipulate particles, with their full potential in active matter still under exploration. This chapter demonstrates self-propulsion in shape-asymmetric particles due to momentum transfer via transverse optical forces, amplified by thermophoretic effects from a light-absorbing coating. Exposing these particles to complex optical fields creates a web of dynamic trajectories influenced by particle size and light intensity. Supported by a numerical model in line with experiments, our findings enhance understanding of motion determinants and have implications across various scientific domains. The image depicts the probability distribution of a capped elongated particle navigating a speckle light profile, highlighting the intricate motion patterns discussed in this chapter

5.1 Introduction

In the realm of active matter, where systems are capable of autonomous work, controlling particle motion presents a significant challenge. Light has emerged as a uniquely advantageous tool for this purpose, offering precise spatiotemporal control that surpasses alternative actuation methods such as electric fields [206], magnetic fields [207], and chemical reactions [228]. Specifically, the modulation of light intensity has become the prevailing strategy for external control, finding applications in a diverse range of systems including molecular motors [229], colloidal particles [230], bacteria [68], and even macroscopic robots [231]. However, many properties of light, such as polarization, wavelength, and momentum transfer, remain largely underexplored [63].

We demonstrate that asymmetric particles can self-propel due to transverse optical forces induced by momentum transfer [20, 8]. This extends the traditional applications of optical forces beyond mere trapping or confinement to induce propulsion. Importantly, these particles can be made from a single material, simplifying the fabrication process compared to more complex designs such as nanostructured light scatterers [65, 66] or chiral plasmonic nanoantennas [66]. Propulsion efficiency can be further enhanced through thermophoretic effects, achievable with a partial coating of light-absorbing material.

The sensitive nature of optical forces combined with particle asymmetry makes the self-propelled motion responsive to features in a complex optical landscape. When exposed to a speckle light pattern—created via the interference of light waves in a multimode optical fiber—these particles not only experience propulsion but also follow complex, directionally-biased trajectories due to forces that both attract and reorient them. Remarkably, these intricate motions can be precisely modeled and predicted through our numerical simulations. This approach offers a compelling alternative to traditional optical manipulation techniques that require continuous monitoring for precise control. In sum, our approach offers a simplified, yet powerful and scalable, strategy to light-based particle manipulation in the microscale, possibly enabling advances in various fields from targeted drug delivery to environmental remediation.

5.2 Results and discussion

In our quest to uncover the underlying principles of light-driven microparticle motion, we explore two distinct particle geometries: simple cylinders and capped cylinders. Both particle types measure 8 µm in length and have a diameter of 2 µm. For the asymmetrical variety, one end of the cylinder is replaced with a cone-shaped “cap” featuring a 4 µm top diameter and forming an angle of approximately 30° with the cylindrical body. These particles are fabricated using two-photon polymerization and placed under three different lighting scenarios: the absence of light, a stable Gaussian optical landscape, and a speckle optical landscape. The speckle optical landscape, see Fig. 5.1(c), is fabricated through a Speckle tweezers setup utilizing the multimode optical fiber (the fiber remains static) [232], see the experimental set-up in Fig. 5.7. On the other hand, the Gaussian landscape, see Fig. 5.1(b), is achieved by rapidly rotating the multimode optical fiber (contrary to the previous case where it remained static), generating an average, out-of-focus Gaussian light profile. The cylinders have predictable behaviors such as Brownian diffusion both without light and under a homogeneous Gaussian profile [114], contrasting with trapping in high-intensity spots in the speckle case [233, 76]. Capped particles particles, on the other hand, exhibit more complex yet predictable and controllable responses. Specifically, they manifest active propulsion in the latter two scenarios, and under speckle illumination, their paths are sculpted by the speckle, weaving a complex network of trajectories, see Fig. 5.1. The subsequent sections embark on a comprehensive examination of these phenomena, dissecting the findings from both experimental and numerical perspectives, and unraveling the intricate interplay between shape, light, and motion.

5.2.1 Experimental study

Under no illumination, see Fig. 5.1(a), both types of particles - simple and capped cylinders - exhibit similar behaviors, as depicted in Fig. 5.1(d,g). They undergo Brownian motion showing random diffusion in both position and orientation without any discernible bias [114]. As expected, the Mean Square Displacement (MSD) of their trajectories exhibits ballistic behavior (MSD $\propto t^2$) at very short time intervals, transitioning to a diffusive regime (MSD $\propto t$) at longer durations [234].

A substantial shift in behavior occurs when the particles are subjected to Gaussian-like profile illumination, as seen in Fig. 5.1(e,h). Simple cylinders continue their pattern of random diffusion; notably, the Gaussian-like profile is sufficiently broad to preclude any significant gradient forces that might attract particles toward the beam center. Conversely, capped cylinders exhibit a distinct behavior, they display active, directed motion, advancing from the cap toward the cylinder at speeds around 3 µm/s for an average light intensity of 1.6 mW/µm². Their MSD, as observed in Fig. 5.1(k), remains ballistic throughout (MSD $\propto t^2$), in contrast to the simple cylinders which revert to a diffusive state (MSD $\propto t$). Importantly, the orientation of the capped cylinders continues to fluctuate randomly, akin to the behavior observed in simple cylinders.

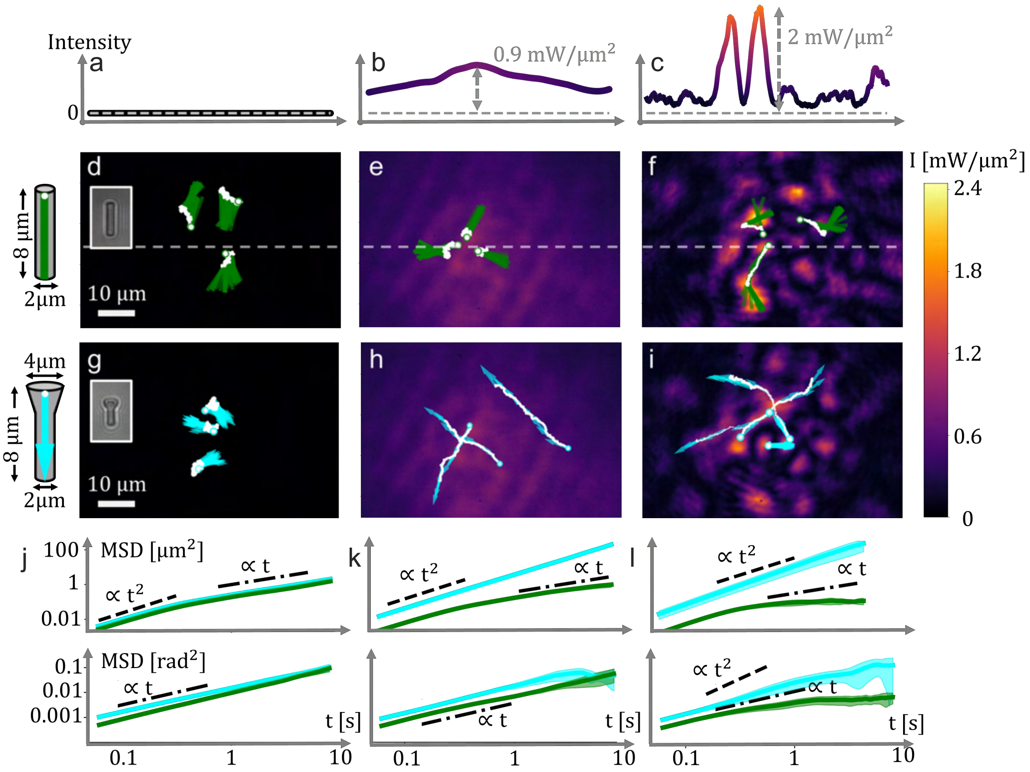

Fig. 5.1 Panels (a-c) display the light intensity profiles of the three distinct optical landscapes along the x-axis, as indicated by the dashed line in plots (d-f). A schematic on the left delineates the two unique particle geometries and is complemented by digital video microscopy insets in (d) and (g). The white dots together with the green rectangles and blue arrows in (d-i) are plotted according to the schematic on the left. Plots (d-f) spotlight the cylindrical particle's behavior under three conditions: absence of illumination (d), Gaussian illumination (e), and speckle illumination (f). Conversely, panels (g-i) offer a parallel analysis for the capped particle. The Mean Square Displacement (MSD) of both position and orientation are quantified in plots (j-l), in green the cylindrical particle and in blue the capped one. In the absence of illumination (d, g), both particle types manifest similar random diffusion, characterized by an MSD (j) that is linearly proportional to time t—except at very short times, where it becomes ballistic and proportional to t^2. Under Gaussian illumination, the capped particle exhibits active directed motion (h), whereas the cylindrical particle maintains random diffusion in both position and orientations, as quantified in the MSD plot (k). The divergence in behavior becomes more pronounced under speckle illumination: the cylindrical particles become confined in both angle and orientation due to gradient optical forces and torques, as seen in plot (l), while capped particles continue to exhibit active propulsion (i), influenced by a blend of these optical forces and torques, the MSD in (l) supports this analysis.

When exposed to a speckle light pattern, as shown in Fig. 5.1(f,i), the dynamics become markedly more complex. Rather than engaging in random diffusion, the simple cylinders are confined to high-intensity zones due to gradient optical forces and torques, resulting in stabilized positions and orientations. Contrarily, capped cylinders that are propelled sufficiently to evade these high-intensity traps, largely maintain their active, directed motion as depicted in Fig. 5.1(i). This speckle-patterned environment contrasts significantly with uniform illumination settings. In this case, propulsion is no longer homogeneous (depends on the local intensity) and the orientation is no longer randomly diffusive but is influenced by gradient forces in high-intensity areas, exerting a torque (the same that impacts the orientation of simple cylinders). Due to this torque, the MSD of the orientation increases at a rate that is faster than linear growth (diffusive) but less than quadratic (ballistic), as noted in Fig. 5.1(l). A rare exception to this active propulsion for the capped cylinders occurs when a particle is anchored near a high-intensity zone due to insufficient propulsive force to counteract the gradient force. In the following section we will add a new effect to prevent this from happening. With this qualitative overview, the subsequent sections will delve into a more detailed analysis of the propulsion mechanisms at play, as well as the unique dynamics of capped particles under speckle light patterns.

Shape-driven propulsion by light

We commence our exploration with the Gaussian illumination condition, approximated as flat within a 20 μm radius from the center. Under this illumination, cylindrical particles maintain their random diffusion, akin to the no-light scenario, see Fig. 5.1(e,k). In contrast, capped particles reveal active motion from the cap towards the cylinder (Fig. 5.1(h,k)). These dynamics are analyzed across a range of average intensities (0 to 2.1 mW/μm²), showing a positive correlation between intensity and trajectory length, thus higher speeds at higher intensities, see Fig. 5.2(a).

The relationship between speed and light intensity displays a linear dependency where the speed in μm/s can be expressed as $v = 1.9 \cdot I + 0.1$. The minor offset of $0.1\,$μm/s is in accordance with the notion that the absence of light eliminates propulsion, as shown in Fig. 5.2(b). The speed is calculated considering 0.25 seconds intervals. At the maximum average intensity available (2.1 mW/μm²), a peak speed of $4.1 \pm 0.5\,$μm/s was observed, indicating that the particle moves about half its body length per second.

Given the particles' uniform composition, propulsion cannot stem from compositional asymmetry, as is the case in many active motion systems [235, 236]. Instead, our side-by-side comparison of the behaviors of cylindrical and capped particles under Gaussian illumination highlights shape as the critical determinant of propulsion. This observation aligns with the notion of a shape-induced transverse component of the optical force, which arises due to the non-symmetric redistribution of light momenta when scattering from non-spherical particles, as shown in Fig. 5.2(b). This transverse optical force [20] has been used to lift and drive non-spherical particles in a homogeneous light field similar to our expanded Gaussian beam [237, 7]. The linear correlation between particle speed and light intensity agrees with the theory of momentum exchange in optical forces. An increase in photon flux through the particle corresponds to an upswing in momentum exchange, which, in turn, leads to a proportional acceleration of the particle's speed.

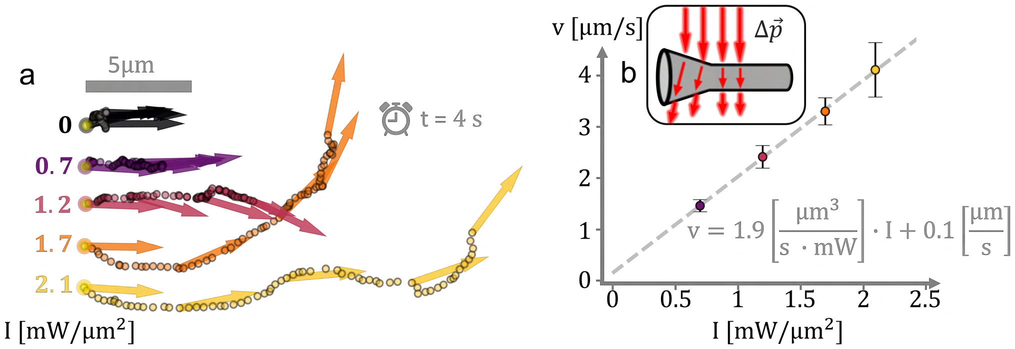

Fig. 5.2 Capped particles under Gaussian illumination at various light intensities. (a) Depicts one representative 4-second trajectory for five different intensities ranging from 0 mW/μm² to 2.1 mW/μm², with arrows indicating the orientation of the particle plotted every second. (b) A scatter plot represents the particle's average speed as a function of light intensity. The dashed gray line is the best-fit straight line to the experimental data, with the corresponding expression shown in gray. The inset illustrates the redistribution of momentum resulting in the propelling force. The change of momentum of light (equal magnitude and opposite direction to the momentum of the particle) is represented as $\Delta\vec{p}$

Dynamics of capped particles under different light patterns

Building on our previous work, where we established that the particle's asymmetrical shape is the key factor driving its propulsion (see previous subsection and Figs.5.1 and 5.2), we now introduce an additional modification to enhance the propulsion. We coat one end of the particle with a light-absorbing material (Platinium, refer to Methods section). This coating introduces a temperature gradient, thereby inducing thermophoresis [238]. This modification qualitatively affects the dynamics in speckle fields, where particles could otherwise become immobilized due to an equilibrium between propelling and gradient forces. The modified design combines both propulsion mechanisms (transverse optical forces and thermophoresis) for enhanced propulsion. To substantiate the impact of thermophoresis, we conducted experiments with Pt-coated cylinders (non capped particles) under Gaussian light (no optical forces, only thermophoresis). The observed propulsion speeds ranged from 1.4 ± 0.4µm/s at 1 mW/µm² to 10.9 ± 4.3µm/s at 2 mW/µm². Notably, these speeds are in the same order of magnitude as the speeds induced by optical forces we previously investigated. Upon confirming the effectiveness of thermophoresis, we proceeded to evaluate the dynamics of the capped, coated particles under three specific lighting environments: no light, Gaussian, and speckle fields.

The intricate behavior of these particles unfolds as we study the probability distribution of linear velocities (v) over 0.25-second intervals (Fig. 5.3(a)). Gaussian illumination yields the highest mean velocity of 4.7 ± 1.4 µm/s, characterized by a normal distribution around this value. As expected, this value is larger than the one we obtained for the non coated particles (2.1 ± 0.2 µm/s). A notably broad spectrum of velocities (not Gaussian) manifests in the speckle case (2.3 ± 2.7 µm/s), attributable to the heterogeneous light profile containing regions of both low and high intensity, with the highest intensities leading to the most elevated velocities. This results in the capability of propelling the particle to speeds as high as 15 µm/s.

Shifting our focus to angular velocities (ω), see Fig. 5.3(b), we observe that both the no-light and Gaussian scenarios, lacking gradient forces, present the lower angular velocities. Here ω is defined as the rate of change of the orientation angle of the particle. Intriguingly, Gaussian illumination results in slightly higher average angular velocities ($14 \pm 10^\circ/\mathrm{s}$) compared to the no-light situation ($9 \pm 7^\circ/\mathrm{s}$). This stems from the non-perfect revolution symmetry of the particles (around the plane that contains the normal vector to the surface and the direction vector of the particle), inducing a coupling between linear and angular speed, thereby introducing chirality and causing propulsion that deviates from a straight path. Although the average angular velocity in the speckle case ($12 \pm 11^\circ/\mathrm{s}$) is slightly lower than the Gaussian scenario, peaks of up to $100^\circ/\mathrm{s}$ are reached, reflecting the influence of gradient forces that exert torque on the particle (similar to observations with cylindrical particles in Fig. 5.1(f)).

In analyzing the mean square displacement (MSD), see Fig. 5.3(c), the Gaussian case stands out, revealing almost ballistic movement over a 5-second observation period. A rapid transition from ballistic motion ($\mathrm{MSD} \propto t^2$) to diffusion ($\mathrm{MSD} \propto t$) is discernible in the absence of illumination, occurring more gradually in the speckle case but earlier than in the Gaussian scenario. This complex behavior for the speckle can be ascribed to the torque from the gradient force, that reorients the particle's direction.

In a meticulous examination of an individual particle's trajectory within the speckle field (Fig.5.3(d)), the particle's alignment with high-intensity regions is evident, with the particle trying to maximize its volume under high intensity regions. Acceleration observed when the cap is positioned in such high intensity areas. This behavior can be understood through the interaction between light and the particle, broken down into three distinct forces, as depicted in Fig.5.1(a). The first force pushes the particle along its length: it is produced by the light reaching the cap, and comes from the combination of the optical forces and thermophoresis; the second pulls it toward bright areas and it is caused by optical forces; the third turns it in the direction of these bright areas due to optical torques. These findings uncover a fascinating mechanism where the light pattern actively guides the particle's path, reinforcing the central thesis that both the particle's shape and the speckle light intensity are the collaborative conductors in the dynamics of capped particles.

Speckle illumination: networked paths

Expanding from our previous examination of individual trajectories, we now turn our focus to the spatial distribution of these paths. Specifically, we explore how an individual particle navigates through space across up to 45 trajectories within the same speckle field. Far from a random exploration, a well-defined network of paths emerges, influenced by the optical torque that reorients the particles, as illustrated in Fig. 5.4(a). The thicker green line labeled with an asterisk represents the trajectory previously depicted in Fig. 5.3(b), underscoring that the rules governing each trajectory remain consistent across the network.

By plotting the position of the capped end, we observe that the particle moves faster in bright regions (marked by more widely separated scatter plot points) compared to dark regions (where scatter plot points are tightly clustered). This insight aligns with the conclusions drawn in the preceding analysis that the particles speed is proportional to the intensity. Delving further into the orientations of the particles reveals additional intriguing properties, as displayed in Fig. 5.4(b). The paths tend to be unidirectional, breaking the directional symmetry and suggesting a preferential exploration in one direction. This characteristic is attributed to the random positioning and shape of the speckle's high-intensity regions, which reorient the particle. Since these regions are not symmetrically distributed, they disrupt the symmetry in the particle's orientation along the paths, enforcing a preferred motion direction. This aspect is further discussed in Supporting Information.

Moreover, the interplay of Brownian noise introduces a stochastic component, allowing paths to both merge and bifurcate. For example, particles 1 and 2 in Fig. 5.4(b), initially sharing a path, separate, resulting in bifurcation (paths of particles 1 and 2 are the ones that have the same colour as the numbers). While particle 2 maintains a horizontal trajectory,

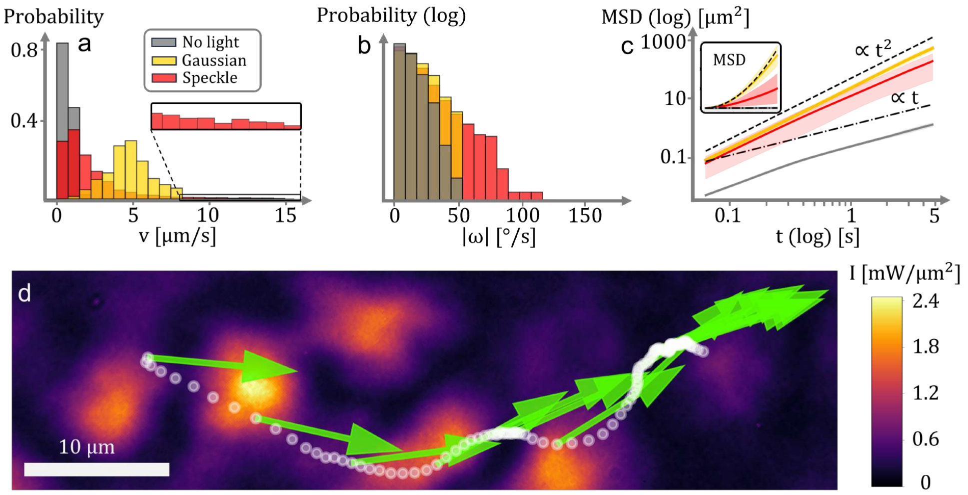

Fig. 5.3 Comparison of the dynamics of the capped particles under different light patterns. (a,b) Show the normalized probability of linear (a) and angular (b) velocities over 0.25-second time intervals; (b) is presented with the probability axis in log scale for clarity. The situation with no light (gray) corresponds with the lower v and ω of the particle. When we use Gaussian illumination (yellow), the average v reaches its maximum value 4.7 ± 1.4,µm/s. Even though Speckle illumination (red) provides a lower v (2.3 ± 2.7,µm/s), it also gives rise to the highest instantaneous velocities (up to 15µm/s). This is also true for ω; the high-intensity spots of the speckle pattern apply a torque that reorients the particles, resulting in the highest values of ω, reaching values of $\omega = 100°/s$. (c) Depicts the Mean Squared Displacement (MSD) for the particles over 5-second trajectories, with dashed lines indicating the slope of a trajectory with ballistic motion ($\propto t^2$) and one with only random diffusion ($\propto t$). (d) Illustrates a representative particle under Speckle illumination, with arrows (plotted every 0.5 seconds) indicating orientation, pointing from the capped end towards the cylinder with the same length as the particle. The white points show the position of the capped end of the particle, which moves faster in the high-intensity regions and is reoriented in these spots.

particle 1 shifts to an almost perpendicular vertical path. In contrast, the trajectory of particle 3 converges with that of particle 2. The considerable length of our particle lowers its rotational diffusion time, making it more prone to follow deterministic trajectories defined by the intensity pattern.

Analyzing how the paths distribute, we observe that the particles tend to follow paths through the high intensity regions. While the average intensity of the speckle is 0.36 mW/µm², the average intensity of the speckle at the particle paths is 0.51 mW/µm². This indicates a preference of the particle to cross these regions. This is explained by the gradient optical force that both attracts and reorients the particles.

Our observations lead us to hypothesize the existence of an optimal size for this network-like motion to manifest. If the particle is too small, it would diffuse before reaching the next high-intensity region. Conversely, if overly large, the particle would not only have a lower rotational diffusion coefficient but would also perceive the cumulative effect of several high-intensity spots, rendering the whole area nearly homogeneous and making it more difficult to reorient, resembling the conditions of a homogeneous illumination case. This discussion will be further detailed in the next section.

5.2.2 Numerical study

After analyzing the dynamics of the particles from our experiments, we introduce a numerical model, encapsulating the minimal essential factors, to successfully reproduce the observed experimental results. Our formulation is built on the Brownian dynamics of a cylindrical particle in a 2D space, governed by the non-inertial Langevin equations. The interaction between light and particle is dissected into three distinct forces: the first, arising from the exchange of linear momentum induced by the particle's asymmetry (presence of the cap) and boosted by the thermophoresis due to the heating of the particle, propels it along its long axis; the second, mediated by the optical gradient force, draws the particle towards areas of high intensity; and the third, also linked to the gradient force, applies a torque, steering it towards the high-intensity regions. A more comprehensive elucidation of the numerical model can be found in the methods section.

Our simulations, guided by these principles, yield results congruent with the experimental observations. Utilizing the same light pattern as in the experiments, we simulate the trajectories of particles with random starting positions and orientations, unveiling the emergence of paths as depicted in Fig. 5.5(a). A composite of 2,500 simulated trajectories, contrasted against colored experimental data, reveals a close alignment, as illustrated in Fig. 5.5(b). Both experimental and simulated results uncover a network of paths with certain areas more densely explored. The congruence between experimental and numerical analyses in the

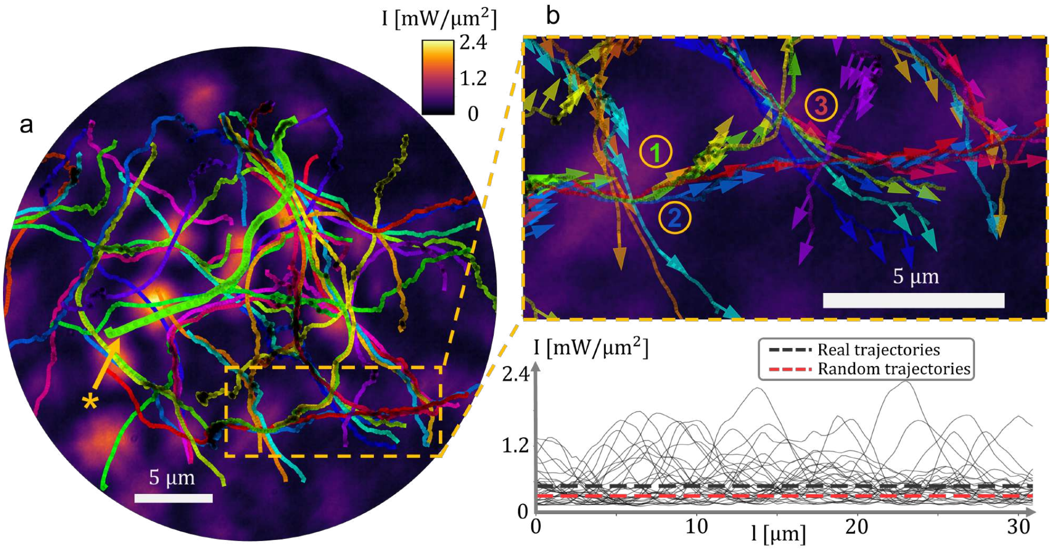

Fig. 5.4 Collection of trajectories of capped particles in the speckle field. (a) Network of trajectories for this specific speckle field, with each color representing one of 45 different trajectories. The thicker green line, marked with an asterisk, corresponds to the same trajectory as in Fig. 5.4(d). (b) Zoomed-in region of the network, illustrating the particle orientations. Arrows indicate the direction from the capped end to the cylindrical end but are intentionally shorter than the particles themselves. The unidirectionality of the paths is evident, with three specific trajectories labeled to highlight the bifurcation and merging of paths. The labeled paths are the ones that have the same colour as the numeric label. (c) Shows the light intensity at the particle position as a function of the travelled distance. The continuous plots show the data for individual trajectories while the dashed black line shows the average intensity at the particle trajectories (0.51 mW/µm²) and the dashed red line shows the average intensity of the region (0.36 mW/µm²).

locations of paths validates our numerical approach and its capacity to provide insights into our system.

Lastly, we leverage our numerical model to investigate the interdependence of network structure and particle length, a relationship graphically represented in Fig. 5.5(c). Our analysis brings to light a captivating phenomenon that was previously hypothesized, the network structure vanishes for both extremely short and long particles. Shorter particles, with their tendency for rapid reorientation and susceptibility to the gradient force, create more densely explored regions around high-intensity spots. Longer particles, on the other hand, constrained by their limited ability to reorient, pursue more linear paths until the gradient torque's influence wanes. This observed dichotomy unveils an absorbing perspective on the nuanced interplay between speckle size ratio, particle length, and network structure, suggesting a rich area for further exploration.

Symmetry-breaking analysis

To deepen our understanding of the system, we now turn our focus to the directionality symmetry-breaking phenomenon. Employing simulations with two distinct light pattern distributions, we analyze the behavior of particle trajectories across three different particle lengths, considering particles starting with opposite positions and orientations.

In the first scenario, we place three elliptical regions of high intensity (Fig. 5.6(a-c)). The particle trajectories depend on the starting position and on the direction in which they exit the high-intensity spots, which are responsible for attracting and reorienting the particles. Particularly, particles with a length of seven microns demonstrate a pronounced difference for opposite cases, as illustrated in Fig. 5.6(b). While all the particles starting from the bottom reach the last high-intensity region, none starting from the top is able to do so. Shorter particles, due to a higher rotational diffusion coefficient, reorient more rapidly, losing their orientation upon exiting the high-intensity regions (Fig. 5.6(a)). Conversely, longer particles may fail to reorient sufficiently within the high-intensity spot due to a lower rotational diffusion coefficient, leading to the possibility of missing subsequent spots (Fig. 5.6(c)).

In the second scenario, we examine two high-intensity spots, each with different brightness and elliptical characteristics (Fig. 5.6(d-f)). The more pronounced spot, with its greater intensity, acts as a stabilizing agent for the orientation of particles. Should the particles first encounter this brighter spot, they exit with a well-defined orientation. In contrast, when particles initially interact with the dimmer spot, their paths exhibit greater variability, as shown in Fig. 5.6(e-f). This difference in behavior leads to a notable observation: for particles of all lengths, completing the path (passing through both spots) is more likely if the trajectory begins with an encounter with the brighter spot.

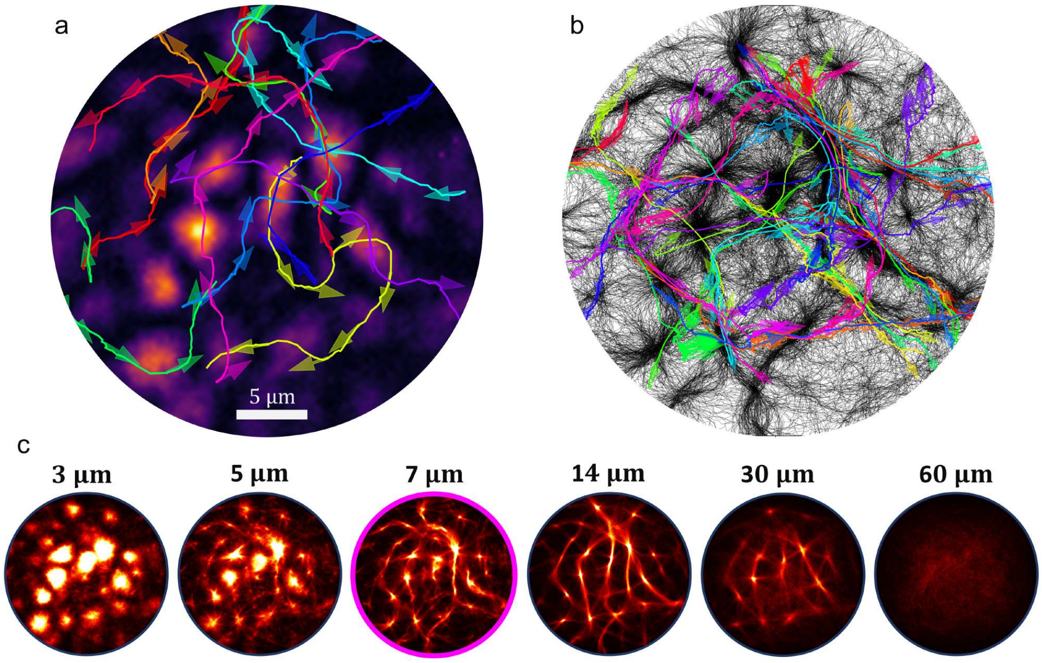

Fig. 5.5 Numerical results of elongated particles traversing a speckle field. (a) Eight-second simulated trajectories for a 7-micron particle within the experimental speckle landscape. Different colors denote distinct simulated trajectories, with arrows marking orientation at 1-second intervals. These simulations reveal behavior akin to the experimental findings, with particles influenced by the high-intensity regions. Notably, even with a limited number of trajectories, recurring paths become evident. (b) A black-and-white plot illustrates 2,500 simulated trajectories for a 7-micron particle in the same speckle field, highlighting the network-like structure. Colored overlays represent experimental trajectories, demonstrating substantial agreement between the simulations and experiments, with paths appearing in nearly identical positions. (c) A comparative examination of the 2D-histogram of the distribution of trajectories within the same speckle field but for particles of varying lengths, ranging from 3 to 60 µm.

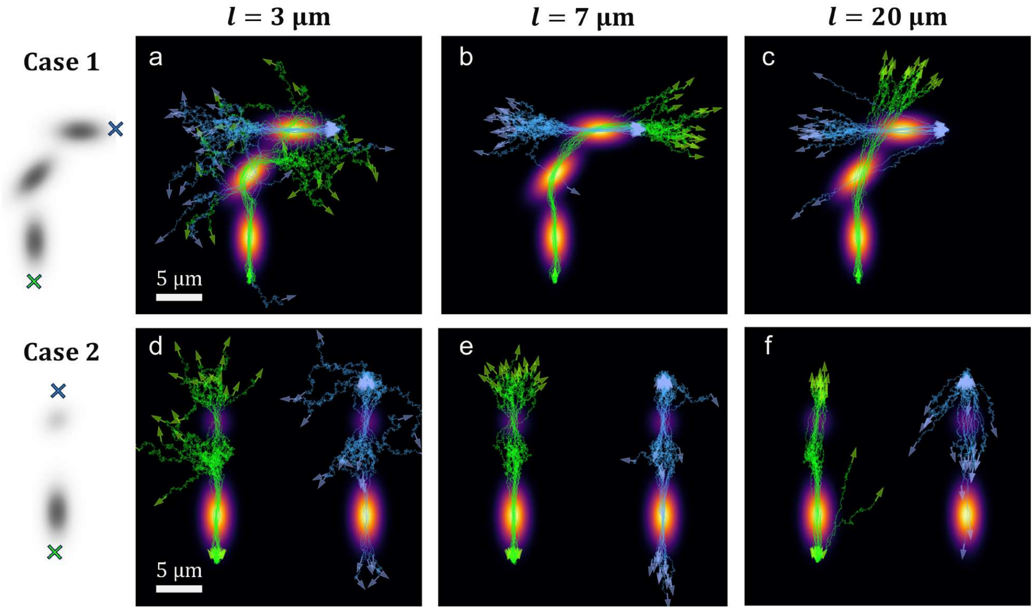

Fig. 5.6 Trajectories of particles starting from opposite positions and orientations in two different light patterns. (a-c) Trajectories of particles in a landscape of three high-intensity elliptical spots. (a) Short particles ($l = 3\,\mu\text{m}$) that reorient and disperse quickly, failing to follow a well-defined path. (b) Particles with the same length as the ones used in the experiments ($l = 7\,\mu\text{m}$); those starting from the bottom align with the bright spots' path, whereas the blue trajectories only cross the first high-intensity spot due to the speckle's light distribution. (c) Larger particles ($l = 20\,\mu\text{m}$) experiencing the gradient force but unable to fully reorient, thus not adhering to well-defined paths. (d-f) Trajectories of particles in an optical landscape with two bright spots, one being brighter and more elliptical. The particles starting from the bottom are illustrated in green, while those moving in the opposite direction are in blue. Across all particle lengths (d-f), those encountering the brighter spot first are more likely to complete the full path and reach the end of the other spot.

5.3 Methods

5.3.1 Particles

Particles were fabricated using a 3D printing process, constructing cylindrical features with a total height of 8 µm and a diameter of 2 µm on a fused SiO_2 substrate using a photosensitive resin (Nanoscribe Photonic Professional GT2, IP-Dip) with a refractive index of 1.54 at the laser's wavelength. For the asymmetrical capped cylinders, the cap was introduced by replacing the top 2 µm of the cylinder with a cone-shaped "cap." This tail featured a top diameter of 4 µm and an angle of approximately 30° with the cylindrical part.

After the 3D printing and development stages, some of the samples were given a thin metalic coating. This was achieved by sputter coating a thin layer of Pt (4 nm) on top at a 90° incidence angle. The particles were released from the substrate through a process of ultrasonication for 20 minutes in 5 mL of Milli-Q water. This procedure yielded a suspension of the particles in liquid, ready for further experimentation.

5.3.2 Experimental setup

Speckle tweezers utilize a multimode (MM) fiber to create a complex interference pattern, or speckle, originating from a laser light source. This speckle pattern is frequently employed to trap or filter particles at specific positions. In our experimental setup, see Fig. 5.1(b), we use a Nd:YAG solid-state laser with a wavelength of 1064 nm and a maximum output power of 2W. The laser light is combined with the illumination light through a dichroic mirror and then focused into the fiber. To maximize the amount of power injected into the fiber, we arrange two lenses in a telescope configuration at the laser's output, thereby increasing the beam's size. We utilize a 0.1 NA multimode fiber, where the numerical aperture determines our speckle's dimensions. As the light beam traverses the fiber, interference occurs due to the overlapping of multiple wave modes. After exiting the fiber, the beam is directed to a microscope set up with a 10x objective lens for focusing and a 60x objective lens for imaging. This assembly is positioned vertically so that the light's propagation direction aligns with gravity's force direction. After propagating through the sample on the stage, a filter is placed to remove the laser light, and the system is imaged using a CMOS camera (Thorlabs DCC1645C).

5.3.3 Numerical model

Our numerical model accounts for three degrees of freedom in the elongated particle, representing its position in the plane (x and y) and its orientation (θ). For the sake of simplicity,

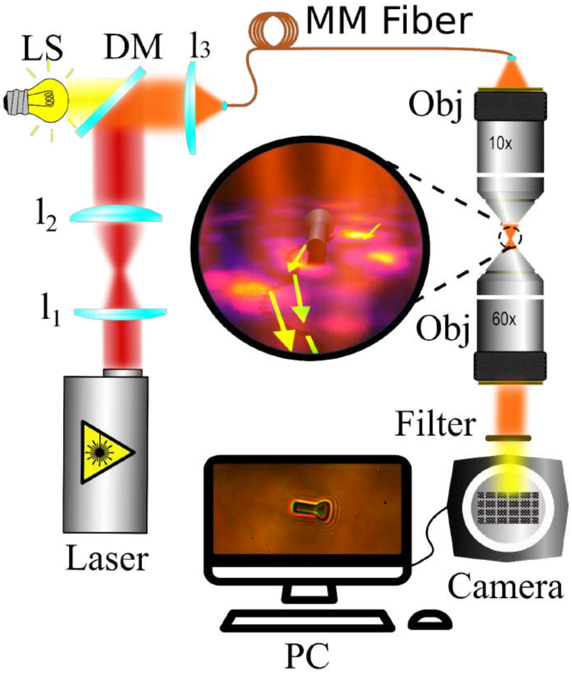

Fig. 5.7 Schematic of the experimental arrangement, encompassing the laser, telescope (lenses l1 and l2), light source, and dichroic mirror to couple the laser with the illumination. Included also are the focusing lens (l3) for the multimode optical fiber (MM Fiber), the two objective lenses for light focusing and sample imaging, the filter to eliminate the laser wavelength, and the camera for system visualization.

we establish our frame of reference within the particle itself, allowing for transformations between the lab frame of reference and the particle frame of reference as needed. Due to the small size of the particles, we employ the non-inertial version of the overdamped Langevin equation, adapting it to the particle's frame of reference. Thus, we can model the particle's motion through changes in its position along the long ($\Delta r_{\parallel}$) and short ($\Delta r_{\perp}$) axes, and changes in orientation ($\Delta\theta$):

$$\Delta r_{\parallel} = \frac{D_{\parallel}\Delta t}{k_B T}\cdot F_{\parallel} + \sqrt{2D_{\parallel}\Delta t}\cdot \xi_{\parallel}, \tag{5.1}$$

$$\Delta r_{\perp} = \frac{D_{\perp}\Delta t}{k_B T}\cdot F_{\perp} + \sqrt{2D_{\perp}\Delta t}\cdot \xi_{\perp}, \tag{5.2}$$

$$\Delta \theta = \frac{D_r\Delta t}{k_B T}\cdot \tau + \sqrt{2D_r\Delta t}\cdot \xi_r. \tag{5.3}$$

In these equations, $D_{\parallel}$, $D_{\perp}$, and D_r denote the diffusion coefficients along the particle's long axis, short axis, and orientation, respectively. Although the actual shape of the particle is more complex, we approximate it as an ellipsoid and calculate the diffusion coefficients using Perrin's analytical solution for ellipsoids [129, 130].

The expressions detailed above describe a microparticle undergoing Brownian diffusion while subject to applied forces. In our model, the influence of the optical landscape translates into forces through three key mechanisms:

- The propelling force (F_{prop}), arising from the exchange of linear momentum due to the particle's asymmetry, propels it along its long axis and is proportional to the intensity at the cap position. This force can be boosted by the effect of thermophoresis that we approximate as linearly depending on the intensity so all the effects can be included in the parameter α:

  $$\vec{F}_{prop} = \alpha \cdot I.$$

- The optical gradient force (F_{grad}) draws the particle towards areas of high intensity and is proportional to the light intensity gradient:

  $$\vec{F}_{grad} = \beta \cdot \nabla I.$$

- The torque (τ_{grad}) steers the particle towards high-intensity regions with a magnitude proportional to the intensity gradient along the angle:

  $$\vec{\tau}_{grad} = \gamma \cdot \frac{\partial I}{\partial \theta}.$$

Where α, β, and γ are free coefficients obtained from experiments. Although this approach considers forces and torques typical of optical forces [4], its simple formulation broadens its applicability to various systems.

5.4 Conclusions

In our study, we have explored the untapped potential of shape-driven asymmetry to scatter light asymmetrically and thereby propel particles. This achievement, demonstrating propulsion exclusively driven by optical forces, reveals an effect that can be combined with other phenomena like thermophoresis, paving the way for new approaches beyond traditional methods.

Our observations extend beyond mere propulsion. We found that optical forces act as navigators, guiding particles along complex paths. This guidance gives rise to a network of trajectories that are far from arbitrary, revealing an underlying structure that breaks the symmetry of system directionality. These paths, with the ability to merge and bifurcate, represent a fascinating interplay between direction and randomness. Supported by our numerical model, which successfully replicates the experimental phenomena, we have not only validated our insights but also established a framework to further control and manipulate these particle trajectories.

Our study marks a thoughtful step towards understanding and controlling motion at micro-scale levels, challenging traditional notions of what guides movement and trajectory. Beyond the immediate applications in targeted drug delivery or material deposition, these insights may resonate with broader phenomena in nature, such as bacterial motion or animal migration. By revealing the intricate interplay of forces that shape trajectories, we contribute to a growing conversation that transcends physics alone, inviting further exploration into the multifaceted determinants of movement in both natural and engineered systems.

Conclusion

From early observations of comet tails to intricate manipulations of microscopic entities, the relationship between light and matter has always been a rich avenue of study. This thesis is a modest contribution to this vast expanse of knowledge. Utilizing optical trapping, I have harnessed its potential to investigate novel systems and uncover the opportunities presented by modern innovations.

Our attempt to incorporate machine learning with traditional methods sought to strike a balance between computation speed and calculation precision. The cosmic realm, with its minute particles, underscored the potential of new tools to delve into the intricacies of our vast universe. Our exploration of the microengine aimed to demonstrate the enhanced control of the orbital motion by exploiting the interplay between optical and thermal forces. And by exploiting shape-asymmetry to propel active matter, we tried to offer a fresh perspective on the determinants of motion at the microscale.

In essence, this work is a small step in the ever-evolving exploration of optical forces and light matter interaction. Each chapter offers a glimpse into this expansive domain, together hinting at the untapped potential in the synergy of light and matter. In moving forward, the insights gained from this thesis may pave the way for new technological applications and further scientific inquiries. Harnessing the interplay between light and matter has the potential to open doors to new innovations and understandings. As the landscape of this research area expands, we hope that the foundations laid here serve as a useful platform for those who embark on this journey in the future.

References

[1] Arthur Ashkin. Forces of a single-beam gradient laser trap on a dielectric sphere in the ray optics regime. *Biophysical Journal*, 61(2):569–582, 1992.

[2] Agnese Callegari, Mite Mijalkov, A Burak Gököz, and Giovanni Volpe. Computational toolbox for optical tweezers in geometrical optics. *J. Opt. Soc. Am. B*, 32(5):B11–B19, 2015.

[3] Patrick C Chaumet and Manuel Nieto-Vesperinas. Time-averaged total force on a dipolar sphere in an electromagnetic field. *Opt. Lett.*, 25(15):1065–1067, 2000.

[4] Philip H Jones, Onofrio M Maragò, and Giovanni Volpe. *Optical Tweezers: Principles and Applications*. Cambridge University Press, 2015.

[5] E. Higurashi, H. Ukita, H. Tanaka, and O. Ohguchi. Optically induced rotation of anisotropic micro-objects fabricated by surface micromachining. *Appl. Phys. Lett.*, 64(17):2209–2210, 1994.

[6] G. A. Swartzlander Jr, T. J. Peterson, A. B. Artusio-Glimpse, and A. D. Raisanen. Stable optical lift. *Nature Photon.*, 5:48–51, 2010.

[7] S. H. Simpson, S. Hanna, T. J. Peterson, and G. A. Swartzlander. Optical lift from dielectric semicylinders. *Opt. Lett.*, 37(19):4038–4040, 2012.

[8] David B Phillips, Miles J Padgett, Simon Hanna, Y-LD Ho, David M Carberry, Mervyn J Miles, and Stephen H Simpson. Shape-induced force fields in optical trapping. *Nature Photonics*, 8(5):400–405, 2014.

[9] B. T. Draine and J. Goodman. Beyond clausius-mosotti: Wave propagation on a polarizable point lattice and the discrete dipole approximation. *Astrophys. J.*, 405:685–697, 1993.

[10] Hendrik Christoffel Hulst and Hendrik C van de Hulst. *Light scattering by small particles*. Courier Corporation, 1981.

[11] J. R. Arias-González and M. Nieto-Vesperinas. Optical forces on small particles: Attractive and repulsive nature and plasmon-resonance conditions. *J. Opt. Soc. Am. A*, 20(7):1201–1209, 2003.

[12] D. Gao, W. Ding, M. Nieto-Vesperinas, X. Ding, M. Rahman, T. Zhang, C.-T. Lim, and C.-W. Qiu. Optical manipulation from the microscale to the nanoscale: Fundamentals, advances and prospects. *Light Sci. Appl.*, 6(9):e17039, 2017.

[13] S. Albaladejo, M. I. Marqués, M. Laroche, and J. J. Sáenz. Scattering forces from the curl of the spin angular momentum of a light field. *Phys. Rev. Lett.*, 102:113602, 2009.

[14] S. Albaladejo, M. I. Marqués, F. Scheffold, and J. J. Sáenz. Giant enhanced diffusion of gold nanoparticles in optical vortex fields. *Nano Lett.*, 9:3527–3531, 2009.

[15] P. Zemánek, A. Jonáš, P. Jákl, M. Šerý, J. Ježek, and M. Liška. Theoretical comparison of optical traps created by standing wave and single beam. *Opt. Commun.*, 220:401–412, 2003.

[16] M. G. Donato, S. Vasi, R. Sayed, P. H. Jones, F. Bonaccorso, A. C. Ferrari, P. G. Gucciardi, and O. M. Maragò. Optical trapping of nanotubes with cylindrical vector beams. *Opt. Lett.*, 37:3381–3383, 2012.

[17] M. I. Marqués. Beam configuration proposal to verify that scattering forces come from the orbital part of the poynting vector. *Optics Letters*, 39:5122–5125, 2014.

[18] V Svak, O Brzobohatỳ, M Šiler, P Jákl, J Kaňka, P Zemánek, and SH Simpson. Transverse spin forces and non-equilibrium particle dynamics in a circularly polarized vacuum optical trap. *Nature communications*, 9(1):5453, 2018.

[19] M. I. Mishchenko. Radiation force caused by scattering, absorption, and emission of light by nonspherical particles. *J. Quant. Spectrosc. Radiat. Transfer*, 70:811–816, 2001.

[20] Rosalba Saija, Maria Antonia Iatı, Arianna Giusto, Paolo Denti, and Ferdinando Borghese. Transverse components of the radiation force on nonspherical particles in the t-matrix formalism. *Journal of Quantitative Spectroscopy & Radiative Transfer*, 94(2):163–179, 2005.

[21] F. Borghese, P. Denti, R. Saija, and M. A. Iatì. Radiation torque on nonspherical particles in the transition matrix formalism. *Optics Express*, 14:9508–9521, 2006.

[22] Robert N C Pfeifer, Timo A Nieminen, Norman R Heckenberg, and Halina Rubinsztein-Dunlop. Colloquium: Momentum of an electromagnetic wave in dielectric media. *Reviews of Modern Physics*, 79(4):1197, 2007.

[23] M. I. Mishchenko, L. D. Travis, and A. A. Lacis. *Scattering, absorption, and emmision of light by small particles.* Cambridge University Press, Cambridge, United Kingdom, 2002.

[24] M. A. Yurkin and A. G. Hoekstra. The discrete dipole approximation: An overview and recent developments. *J. Quant. Spect. Rad. Transf.*, 106:558–589, 2007.

[25] K. Yee. Numerical solution of initial boundary value problems involving maxwell's equations in isotropic media. *IEEE Trans. Antennas Propag.*, 14:302–307, 1966.

[26] P. C. Waterman. Symmetry, unitarity and geometry in electromagnetic scattering. *Phys. Rev. D*, 3:825–839, 1971.

[27] Stephen H. Simpson and Simon Hanna. Application of the discrete dipole approximation to optical trapping calculations of inhomogeneous and anisotropic particles. *Opt. Express*, 19:16526–16541, 2011.

[28] D. C. Benito, S. H. Simpson, and S. Hanna. Fdtd simulations of forces on particles during holographic assembly. *Opt. Express*, 16:2942–2957, 2008.

[29] P Polimeno, A Magazzù, MA Iatì, R Saija, L Folco, D Bronte Ciriza, MG Donato, A Foti, PG Gucciardi, A Saidi, et al. Optical tweezers in a dusty universe. *The European Physical Journal Plus*, 136(3):1–23, 2021.

[30] Giuseppe Pesce, Giorgio Volpe, Onofrio M Maragó, Philip H Jones, Sylvain Gigan, Antonio Sasso, and Giovanni Volpe. Step-by-step guide to the realization of advanced optical tweezers. *JOSA B*, 32(5):B84–B98, 2015.

[31] J. C. Crocker and D. G. Grier. Methods of digital video microscopy for colloidal studies. *J. Colloid Interf. Sci.*, 179:298–310, 1996.

[32] I. F. Sbalzarini and P. Koumoutsakos. Feature point tracking and trajectory analysis for video imaging in cell biology. *J. Struct. Biol.*, 151:182–195, 2005.

[33] Saga Helgadottir, Aykut Argun, and Giovanni Volpe. Digital video microscopy enhanced by deep learning. *Optica*, 6(4):506–513, 2019.

[34] F. Gittes and CH. F. Schmidt. Interference model for back-focal plane displacement detection in optical tweezers. *Opt. Lett.*, 23:7–9, 1998.

[35] O. M. Maragò, P. H. Jones, F. Bonaccorso, V. Scardaci, P. G. Gucciardi, A. G. Rozhin, and A. C. Ferrari. Femtonewton force sensing with optically trapped nanotubes. *Nano Lett.*, 8:3211–3216, 2008.

[36] Maria G Donato, Marco A Monaca, Giuliana Faggio, Luca De Stefano, Philip H Jones, Pietro G Gucciardi, and Onofrio M Maragò. Optical trapping of porous silicon nanoparticles. *Nanotechnology*, 22(50):505704, 2011.

[37] O. M. Maragò, F. Bonaccorso, R. Saija, G. Privitera, P. G. Gucciardi, M. A. Iatì, G. Calogero, P. H. Jones, F. Borghese, P. Denti, V. Nicolosi, and A. C. Ferrari. Brownian motion of graphene. *ACS Nano*, 4:7515–7523, 2010.

[38] Simon F Tolić-Nørrelykke, Erik Schäffer, Jonathon Howard, Francesco S Pavone, Frank Jülicher, and Henrik Flyvbjerg. Calibration of optical tweezers with positional detection in the back focal plane. *Rev. Sci. Instrum.*, 77(10):103101, 2006.

[39] A Buosciolo, G Pesce, and A Sasso. New calibration method for position detector for simultaneous measurements of force constants and local viscosity in optical tweezers. *Opt. Commun.*, 230(4):357–368, 2004.

[40] K. Berg-Sorensen and H. Flyvbjerg. Power spectrum analysis for optical tweezers. *Rev. Sci. Instrum.*, 75:594, 2004.

[41] M. G. Donato, E. Messina, A. Foti, T. J. Smart, P. H. Jones, M. A. Iatì, R. Saija, P. G. Gucciardi, and O. M. Maragò. Optical trapping and optical force positioning of two-dimensional materials. *Nanoscale*, 10:1245–1255, 2018.

[42] Max Born and Emil Wolf. *Principles of Optics, 7th (expanded) edition*. Cambridge University Press, 1999.

[43] Laura Pérez García, Jaime Donlucas Pérez, Giorgio Volpe, Alejandro V Arzola, and Giovanni Volpe. High-performance reconstruction of microscopic force fields from brownian trajectories. *Nature communications*, 9(1):1–9, 2018.

[44] S. Suresh. Mechanical response of human red blood cells in health and disease: Some structure-property-function relationships. *Journal of Materials Research*, 21(8):1871–1877, 2006.

[45] Rupesh Agrawal, Joseph Sherwood, Jay Chhablani, Ashutosh Ricchariya, Sangho Kim, Philip H. Jones, Stavroula Balabani, and David Shima. Red blood cells in retinal vascular disorders. *Blood Cells, Molecules, and Diseases*, 56(1):53 – 61, 2016.

[46] A. Ashkin and J. M. Dziedzic. Optical trapping and manipulation of viruses and bacteria. *Science*, 235:1517–1520, 1987.

[47] S. Suresh, J. Spatz, J.P. Mills, A. Micoulet, M. Dao, C.T. Lim, M. Beil, and T. Seufferlein. Single-cell biomechanics and human disease states: Gastrointestinal cancer and malaria. *Acta Biomater.*, 1:16, 2005.

[48] Jakob MA Mauritz, Teresa Tiffert, Rachel Seear, Franziska Lautenschläger, Alessandro Esposito, Virgilio L Lew, Jochen R Guck, and Clemens F Kaminski. Detection of plasmodium falciparum-infected red blood cells by optical stretching. *Journal of Biomedical Optics*, 15(3):030517, 2010.

[49] Rupesh Agrawal, Thomas Smart, João Nobre-Cardoso, Christopher Richards, Rhythm Bhatnagar, Adnan Tufail, David Shima, Phil H Jones, and Carlos Pavesio. Assessment of red blood cell deformability in type 2 diabetes mellitus and diabetic retinopathy by dual optical tweezers stretching technique. *Scientific Reports*, 6(1):1–12, 2016.

[50] Vahid Sheikh-Hasani, Mehrad Babaei, Ali Azadbakht, Hamidreza Pazoki-Toroudi, Alireza Mashaghi, Ali Akbar Moosavi-Movahedi, and Seyed Nader Seyed Reihani. Atorvastatin treatment softens human red blood cells: an optical tweezers study. *Biomed. Opt. Express*, 9(3):1256–1261, 2018.

[51] Robert C Hale, Meredith E Seeley, Mark J La Guardia, Lei Mai, and Eddy Y Zeng. A global perspective on microplastics. *Journal of Geophysical Research: Oceans*, 125(1):e2018JC014719, 2020.

[52] Donald E Brownlee. Cosmic dust: Collection and research. *Annual Review of Earth and Planetary Sciences*, 13(1):147–173, 1985.

[53] Paul Farrell and Kathryn Nelson. Trophic level transfer of microplastic: Mytilus edulis (l.) to carcinus maenas (l.). *Environmental pollution*, 177:1–3, 2013.

[54] Raymond Gillibert, Gireeshkumar Balakrishnan, Quentin Deshoules, Morgan Tardivel, Alessandro Magazzù, Maria Grazia Donato, Onofrio M Maragò, Marc Lamy de La Chapelle, Florent Colas, Fabienne Lagarde, et al. Raman tweezers for small microplastics and nanoplastics identification in seawater. *Environmental science & technology*, 53(15):9003–9013, 2019.

[55] Raymond Gillibert, Alessandro Magazzù, Agnese Callegari, David Bronte-Ciriza, Antonino Foti, Maria Grazia Donato, Onofrio M Maragò, Giovanni Volpe, Marc Lamy de La Chapelle, Fabienne Lagarde, et al. Raman tweezers for tire and road wear micro-and nanoparticles analysis. *Environmental Science: Nano*, 9(1):145–161, 2022.

[56] A Magazzù, D Bronte Ciriza, A Musolino, A Saidi, P Polimeno, MG Donato, A Foti, PG Gucciardi, MA Iatì, R Saija, et al. Investigation of dust grains by optical tweezers for space applications. *The Astrophysical Journal*, 942(1):11, 2022.

[57] Tamás Vicsek and Anna Zafeiris. Collective motion. *Physics reports*, 517(3-4):71–140, 2012.

[58] Sriram Ramaswamy. Active matter. *Journal of Statistical Mechanics: Theory and Experiment*, 2017(5):054002, 2017.

[59] Navish Wadhwa and Howard C Berg. Bacterial motility: machinery and mechanisms. *Nature reviews microbiology*, 20(3):161–173, 2022.

[60] Eamonn A Gaffney, Hermes Gadêlha, David J Smith, John R Blake, and Jackson C Kirkman-Brown. Mammalian sperm motility: observation and theory. *Annual Review of Fluid Mechanics*, 43:501–528, 2011.

[61] Andreas Zöttl and Holger Stark. Emergent behavior in active colloids. *Journal of Physics: Condensed Matter*, 28(25):253001, 2016.

[62] Edward M Purcell. Life at low reynolds number. *American journal of physics*, 45(1):3–11, 1977.

[63] Marcel Rey, Giovanni Volpe, and Giorgio Volpe. Light, matter, action: Shining light on active matter. *ACS photonics*, 10(5):1188–1201, 2023.

[64] Daniel Andrén, Denis G Baranov, Steven Jones, Giovanni Volpe, Ruggero Verre, and Mikael Käll. Microscopic metavehicles powered and steered by embedded optical metasurfaces. *Nature Nanotechnology*, 16(9):970–974, 2021.

[65] Yoshito Y Tanaka, Pablo Albella, Mohsen Rahmani, Vincenzo Giannini, Stefan A Maier, and Tsutomu Shimura. Plasmonic linear nanomotor using lateral optical forces. *Science Advances*, 6(45):eabc3726, 2020.

[66] Xiaofei Wu, Raphael Ehehalt, Gary Razinskas, Thorsten Feichtner, Jin Qin, and Bert Hecht. Light-driven microdrones. *Nature Nanotechnology*, 17(5):477–484, 2022.

[67] R Menzel. Comparative physiology and evolution of vision in invertebrates. *(No Title)*, page 503, 1979.

[68] Giacomo Frangipane, Dario Dell'Arciprete, Serena Petracchini, Claudio Maggi, Filippo Saglimbeni, Silvio Bianchi, Gaszton Vizsnyiczai, Maria Lina Bernardini, and Roberto Di Leonardo. Dynamic density shaping of photokinetic e. coli. *Elife*, 7:e36608, 2018.

[69] Nicola Pellicciotta, Ojus Satish Bagal, Viridiana Carmona Sosa, Giacomo Frangipane, Gaszton Vizsnyiczai, and Roberto Di Leonardo. Light controlled biohybrid microbots. *Advanced Functional Materials*, page 2214801, 2023.

[70] Jing Hu, Shuxue Zhou, Yangyi Sun, Xiaosheng Fang, and Limin Wu. Fabrication, properties and applications of janus particles. *Chemical Society Reviews*, 41(11):4356–4378, 2012.

[71] Hongxu Chen, Qilong Zhao, and Xuemin Du. Light-powered micro/nanomotors. *Micromachines*, 9(2):41, 2018.

[72] Jizhuang Wang, Ze Xiong, Jing Zheng, Xiaojun Zhan, and Jinyao Tang. Light-driven micro/nanomotor for promising biomedical tools: principle, challenge, and prospect. *Accounts of chemical research*, 51(9):1957–1965, 2018.

[73] Kilian Dietrich, Nick Jaensson, Ivo Buttinoni, Giorgio Volpe, and Lucio Isa. Microscale marangoni surfers. *Physical Review Letters*, 125(9):098001, 2020.

[74] Yang Song and Shaowei Chen. Janus nanoparticles: preparation, characterization, and applications. *Chemistry–An Asian Journal*, 9(2):418–430, 2014.

[75] Étude O'Neel-Judy, Dylan Nicholls, John Castañeda, and John G Gibbs. Light-activated, multi-semiconductor hybrid microswimmers. *Small*, 14(32):1801860, 2018.

[76] David Bronte Ciriza, Alessandro Magazzù, Agnese Callegari, Gunther Barbosa, Antonio AR Neves, Maria Antonia Iatì, Giovanni Volpe, and Onofrio M Maragò. Faster and more accurate geometrical-optics optical force calculation using neural networks. *ACS photonics*, 10(1):234–241, 2022.

[77] Aykut Argun, Tobias Thalheim, Stefano Bo, Frank Cichos, and Giovanni Volpe. Enhanced force-field calibration via machine learning. *Applied Physics Reviews*, 7(4):041404, 2020.

[78] Tanuj Aggarwal and Murti Salapaka. Real-time nonlinear correction of back-focal-plane detection in optical tweezers. *Review of Scientific Instruments*, 81(12):123105, 2010.

[79] Neuton Li, Jasper Cadusch, and Kenneth Crozier. Algorithmic approach for designing plasmonic nanotweezers. *Optics Letters*, 44(21):5250–5253, 2019.

[80] Yi-Ren Chang, Long Hsu, and Sien Chi. Optical trapping of a spherically symmetric sphere in the ray-optics regime: a model for optical tweezers upon cells. *Applied Optics*, 45(16):3885–3892, 2006.

[81] Susan E Skelton, Marios Sergides, Gianluca Memoli, Onofrio M Maragó, and Philip H Jones. Trapping and deformation of microbubbles in a dual-beam fibre-optic trap. *Journal of Optics*, 14(7):075706, 2012.

[82] Jing Liu, Chao Zhang, Yiwu Zong, Honglian Guo, and Zhi-Yuan Li. Ray-optics model for optical force and torque on a spherical metal-coated janus microparticle. *Photonics Research*, 3(5):265–274, 2015.

[83] Giorgio Volpe and Giovanni Volpe. Simulation of a Brownian particle in an optical trap. *American Journal of Physics*, 81(3):224–230, 2013.

[84] Richard W Bowman and Miles J Padgett. Optical trapping and binding. *Reports on Progress in Physics*, 76(2):026401, 2013.

[85] Ann AM Bui, Alexander B Stilgoe, Nima Khatibzadeh, Timo A Nieminen, Michael W Berns, and Halina Rubinsztein-Dunlop. Escape forces and trajectories in optical tweezers and their effect on calibration. *Optics Express*, 23(19):24317–24330, 2015.

[86] Leonardo Andr Ambrosio and HE Hernández-Figueroa. Inversion of gradient forces for high refractive index particles in optical trapping. *Optics Express*, 18(6):5802–5808, 2010.

[87] William H Press, Brian P Flannery, Saul Arno Teukolsky, and William T Vetterling. *Numerical Recipes in Pascal: The Art of Scientific Computing [disc]*. Cambridge university press Cambridge, UK, 1989.

[88] Isaac CD Lenton, Giovanni Volpe, Alexander B Stilgoe, Timo A Nieminen, and Halina Rubinsztein-Dunlop. Machine learning reveals complex behaviours in optically trapped particles. *Machine Learning: Science and Technology*, 1(4):045009, 2020.

[89] Tom M Mitchell. *Machine learning*, volume 1. McGraw-hill New York, 1997.

[90] John Peurifoy, Yichen Shen, Li Jing, Yi Yang, Fidel Cano-Renteria, Brendan G DeLacy, John D Joannopoulos, Max Tegmark, and Marin Soljačić. Nanophotonic particle simulation and inverse design using artificial neural networks. *Sci. Adv.*, 4(6):eaar4206, 2018.

[91] Yair Rivenson, Zoltán Göröcs, Harun Günaydin, Yibo Zhang, Hongda Wang, and Aydogan Ozcan. Deep learning microscopy. *Optica*, 4(11):1437–1443, 2017.

[92] Benjamin Midtvedt, Saga Helgadottir, Aykut Argun, Jesús Pineda, Daniel Midtvedt, and Giovanni Volpe. Quantitative digital microscopy with deep learning. *Applied Physics Reviews*, 8(1):011310, 2021.

[93] Laura Natali, Saga Helgadottir, Onofrio M Marago, and Giovanni Volpe. Improving epidemic testing and containment strategies using machine learning. *Machine Learning: Science and Technology*, 2(3):035007, 2021.

[94] Michel H Devoret, Daniel Esteve, John M Martinis, Andrew Cleland, and John Clarke. Resonant activation of a Brownian particle out of a potential well: Microwave-enhanced escape from the zero-voltage state of a Josephson junction. *Physical Review B*, 36(1):58, 1987.

[95] Nicolaas Godfried Van Kampen. *Stochastic processes in physics and chemistry*, volume 1. Elsevier, 1992.

[96] Andrej Šali, Eugene Shakhnovich, and Martin Karplus. How does a protein fold. *Nature*, 369(6477):248–251, 1994.

[97] Lowell I McCann, Mark Dykman, and Brage Golding. Thermally activated transitions in a bistable three-dimensional optical trap. *Nature*, 402(6763):785–787, 1999.

[98] AB Stilgoe, NR Heckenberg, TA Nieminen, and H Rubinsztein-Dunlop. Phase-transition-like properties of double-beam optical tweezers. *Phys. Rev. Lett.*, 107(24):248101, 2011.

[99] Martin Šiler and Pavel Zemánek. Particle jumps between optical traps in a one-dimensional (1d) optical lattice. *New Journal of Physics*, 12(8):083001, 2010.

[100] Loïc Rondin, Jan Gieseler, Francesco Ricci, Romain Quidant, Christoph Dellago, and Lukas Novotny. Direct measurement of kramers turnover with a levitated nanoparticle. *Nature Nanotechnology*, 12(12):1130–1133, 2017.

[101] F Borghese, P Denti, Rosalba Saija, MA Iatì, and OM Maragò. Radiation torque and force on optically trapped linear nanostructures. *Phys. Rev. Lett.*, 100(16):163903, 2008.

[102] MG Donato, S Vasi, R Sayed, PH Jones, F Bonaccorso, AC Ferrari, PG Gucciardi, and OM Maragò. Optical trapping of nanotubes with cylindrical vector beams. *Opt. Lett.*, 37(16):3381–3383, 2012.

[103] Paolo Polimeno, Rosalba Saija, Cristian Degli Esposti Boschi, Onofrio M Maragò, and Maria Antonia Iatì. Optical forces in the T-matrix formalism. *Atti della Accademia Peloritana dei Pericolanti-Classe di Scienze Fisiche, Matematiche e Naturali*, 97(1):2, 2019.

[104] SH Simpson and S Hanna. Stability analysis and thermal motion of optically trapped nanowires. *Nanotechnology*, 23(20):205502, 2012.

[105] Alessia Irrera, Pietro Artoni, Rosalba Saija, Pietro G Gucciardi, Maria Antonia Iatì, Ferdinando Borghese, Paolo Denti, Fabio Iacona, Francesco Priolo, and Onofrio M Marago. Size-scaling in optical trapping of silicon nanowires. *Nano Letters*, 11(11):4879–4884, 2011.

[106] Rupesh Agrawal, Joseph Sherwood, Jay Chhablani, Ashutosh Ricchariya, Sangho Kim, Philip H. Jones, Stavroula Balabani, and David Shima. Red blood cells in retinal vascular disorders. *Blood Cells, Molecules, and Diseases*, 56(1):53–61, 2016.

[107] Tatiana Avsievich, Ruixue Zhu, Alexey Popov, Alexander Bykov, and Igor Meglinski. The advancement of blood cell research by optical tweezers. *Reviews in Physics*, 5:100043, 2020.

[108] SC Grover, Robert C Gauthier, and AG Skirtach. Analysis of the behaviour of erythrocytes in an optical trapping system. *Optics Express*, 7(13):533–539, 2000.

[109] Guan-Bo Liao, Paul B Bareil, Yunlong Sheng, and Arthur Chiou. One-dimensional jumping optical tweezers for optical stretching of bi-concave human red blood cells. *Optics Express*, 16(3):1996–2004, 2008.

[110] Riccardo Tognato and Philip H Jones. Ray optics model for optical trapping of biconcave red blood cells. *Micromachines*, 14(1):83, 2022.

[111] Riccardo Tognato, David Bronte-Ciriza, Onofrio M Marago, and Philip H Jones. Modelling red blood cell optical trapping by machine learning improved geometrical optics calculations. *bioRxiv*, pages 2023–02, 2023.

[112] Jennifer E Curtis, Brian A Koss, and David G Grier. Dynamic holographic optical tweezers. *Optics communications*, 207(1-6):169–175, 2002.

[113] Yoshio Tanaka, Shogo Tsutsui, Mitsuru Ishikawa, and Hiroyuki Kitajima. Hybrid optical tweezers for dynamic micro-bead arrays. *Optics Express*, 19(16):15445–15451, 2011.

[114] Yilong Han, Ahmed M Alsayed, Maurizio Nobili, Jian Zhang, Tom C Lubensky, and Arjun G Yodh. Brownian motion of an ellipsoid. *Science*, 314(5799):626–630, 2006.

[115] Onofrio M Maragò, Francesco Bonaccorso, Rosalba Saija, Giulia Privitera, Pietro G Gucciardi, Maria Antonia Iatì, Giuseppe Calogero, Philip H Jones, Ferdinando Borghese, Paolo Denti, et al. Brownian motion of graphene. *ACS Nano*, 4(12):7515–7523, 2010.

[116] PH Jones, F Palmisano, F Bonaccorso, PG Gucciardi, G Calogero, AC Ferrari, and Onofrio M Maragò. Rotation detection in light-driven nanorotors. *ACS nano*, 3(10):3077–3084, 2009.

[117] Alessia Irrera, Alessandro Magazzù, Pietro Artoni, Stephen H Simpson, Simon Hanna, Philip H Jones, Francesco Priolo, Pietro Giuseppe Gucciardi, and Onofrio M Maragò. Photonic torque microscopy of the nonconservative force field for optically trapped silicon nanowires. *Nano letters*, 16(7):4181–4188, 2016.

[118] Giulia Rusciano, Anna C De Luca, Giuseppe Pesce, and Antonio Sasso. Raman tweezers as a diagnostic tool of hemoglobin-related blood disorders. *Sensors*, 8(12):7818–7832, 2008.

[119] Yongyin Cao, Alexander B Stilgoe, Lixue Chen, Timo A Nieminen, and Halina Rubinsztein-Dunlop. Equilibrium orientations and positions of non-spherical particles in optical traps. *Optics Express*, 20(12):12987–12996, 2012.

[120] Andrés Cózar, Fidel Echevarría, J Ignacio González-Gordillo, Xabier Irigoien, Bárbara Úbeda, Santiago Hernández-León, Álvaro T Palma, Sandra Navarro, Juan García-de Lomas, Andrea Ruiz, et al. Plastic debris in the open ocean. *Proceedings of the National Academy of Sciences*, 111(28):10239–10244, 2014.

[121] Gabriel Erni-Cassola, Matthew I Gibson, Richard C Thompson, and Joseph A Christie-Oleza. Lost, but found with nile red: a novel method for detecting and quantifying small microplastics (1 mm to 20 μm) in environmental samples. *Environmental science & technology*, 51(23):13641–13648, 2017.

[122] Giuseppe Suaria, Carlo G Avio, Annabella Mineo, Gwendolyn L Lattin, Marcello G Magaldi, Genuario Belmonte, Charles J Moore, Francesco Regoli, and Stefano Aliani. The mediterranean plastic soup: synthetic polymers in mediterranean surface waters. *Scientific reports*, 6(1):37551, 2016.

[123] Soeun Eo, Sang Hee Hong, Young Kyoung Song, Jongsu Lee, Jongmyoung Lee, and Won Joon Shim. Abundance, composition, and distribution of microplastics larger than 20 μm in sand beaches of south korea. *Environmental pollution*, 238:894–902, 2018.

[124] Martin Pivokonsky, Lenka Cermakova, Katerina Novotna, Petra Peer, Tomas Cajthaml, and Vaclav Janda. Occurrence of microplastics in raw and treated drinking water. *Science of the total environment*, 643:1644–1651, 2018.

[125] Julien Gigault, Alexandra Ter Halle, Magalie Baudrimont, Pierre-Yves Pascal, Fabienne Gauffre, Thuy-Linh Phi, Hind El Hadri, Bruno Grassl, and Stéphanie Reynaud. Current opinion: what is a nanoplastic? *Environmental pollution*, 235:1030–1034, 2018.

[126] Peter C Waterman. Symmetry, unitarity, and geometry in electromagnetic scattering. *Physical review D*, 3(4):825, 1971.

[127] François Chollet et al. Keras: The python deep learning library. *Astrophysics Source Code Library*, pages ascl–1806, 2018.

[128] Agnese Callegari and Giovanni Volpe. Numerical simulations of active Brownian particles. *Flowing Matter*, page 211, 2019.

[129] Francis Perrin. Mouvement brownien d'un ellipsoide-i. dispersion diélectrique pour des molécules ellipsoidales. *J. Phys. Radium*, 5(10):497–511, 1934.

[130] Yilong Han, Ahmed Alsayed, Maurizio Nobili, and Arjun G Yodh. Quasi-two-dimensional diffusion of single ellipsoids: Aspect ratio and confinement effects. *Physical Review E*, 80(1):011403, 2009.

[131] J García de la Torre, S Navarro, MC Lopez Martinez, FG Diaz, and JJ Lopez Cascales. Hydro: a computer program for the prediction of hydrodynamic properties of macromolecules. *Biophysical Journal*, 67(2):530–531, 1994.

[132] J García de la Torre, G del Rio Echenique, and A Ortega. Improved calculation of rotational diffusion and intrinsic viscosity of bead models for macromolecules and nanoparticles. *The Journal of Physical Chemistry B*, 111(5):955–961, 2007.

[133] José García de la Torre, María L Huertas, and Beatriz Carrasco. Calculation of hydrodynamic properties of globular proteins from their atomic-level structure. *Biophysical Journal*, 78(2):719–730, 2000.

[134] Jian S Dai. Euler–Rodrigues formula variations, quaternion conjugation and intrinsic connections. *Mechanism and Machine Theory*, 92:144–152, 2015.

[135] Francesco Calura, Antonio Pipino, and Francesca Matteucci. The cycle of interstellar dust in galaxies of different morphological types. *Astronomy & Astrophysics*, 479(3):669–685, 2008.

[136] Stanford E Woosley, Alex Heger, and Thomas A Weaver. The evolution and explosion of massive stars. *Reviews of modern physics*, 74(4):1015, 2002.

[137] SE Woosley and Thomas A Weaver. The evolution and explosion of massive stars ii: Explosive hydrodynamics and nucleosynthesis. Technical report, Lawrence Livermore National Lab., CA (United States), 1995.

[138] Frans JM Rietmeijer. Interplanetary dust particles. In *Planetary Materials*, volume 36. De Gruyter, 1998.

[139] Bruce T Draine. Interstellar dust grains. *Annual Review of Astronomy and Astrophysics*, 41:241–289, 2003.

[140] Katharina Lodders and Sachiko Amari. Presolar grains from meteorites: Remnants from the early times of the solar system. *Geochemistry*, 65(2):93–166, 2005.

[141] Andrew J Westphal, Rhonda M Stroud, Hans A Bechtel, Frank E Brenker, Anna L Butterworth, George J Flynn, David R Frank, Zack Gainsforth, Jon K Hillier, Frank Postberg, et al. Evidence for interstellar origin of seven dust particles collected by the stardust spacecraft. *science*, 345(6198):786–791, 2014.

[142] DE Brownlee, P Tsou, JD Anderson, MS Hanner, RL Newburn, Z Sekanina, BC Clark, F Hörz, ME Zolensky, J Kissel, et al. Stardust: Comet and interstellar dust sample return mission. *Journal of Geophysical Research: Planets*, 108(E10), 2003.

[143] David R Frank, Andrew J Westphal, Michael E Zolensky, Zack Gainsforth, Anna L Butterworth, Ronald K Bastien, Carlton Allen, David Anderson, Asna Ansari, Sasa Bajt, et al. Stardust interstellar preliminary examination ii: Curating the interstellar dust collector, picokeystones, and sources of impact tracks. *Meteoritics & Planetary Science*, 49(9):1522–1547, 2014.

[144] John P Testa Jr, John R Stephens, Walter W Berg, Thomas A Cahill, Takashi Onaka, Yoshikazu Nakada, James R Arnold, Norman Fong, and Paul D Sperry. Collection of microparticles at high balloon altitudes in the stratosphere. *Earth and planetary science letters*, 98(3-4):287–302, 1990.

[145] AD Taylor, WJ Baggaley, and DI Steel. Discovery of interstellar dust entering the earth's atmosphere. *Nature*, 380(6572):323–325, 1996.

[146] Vincenzo Della Corte, Pasquale Palumbo, Alessandra Rotundi, Simone De Angelis, Frans JM Rietmeijer, Ezio Bussoletti, Alessandra Ciucci, Marco Ferrari, Valentina Galluzzi, and Ernesto Zona. In situ collection of refractory dust in the upper stratosphere: The duster facility. *Space Science Reviews*, 169:159–180, 2012.

[147] DS Lauretta, SS Balram-Knutson, E Beshore, WV Boynton, C Drouet d'Aubigny, DN DellaGiustina, HL Enos, DR Golish, CW Hergenrother, ES Howell, et al. Osiris-rex: sample return from asteroid (101955) bennu. *Space Science Reviews*, 212(1):925–984, 2017.

[148] Matthew J Genge, Cécile Engrand, Matthieu Gounelle, and Susan Taylor. The classification of micrometeorites. *Meteoritics & Planetary Science*, 43(3):497–515, 2008.

[149] Luigi Folco and Carole Cordier. Micrometeorites. 2015.

[150] Susan Taylor, Scott Messenger, and Luigi Folco. Cosmic dust: finding a needle in a haystack. *Elements*, 12(3):171–176, 2016.

[151] Frans JM Rietmeijer. Identification of fe-rich meteoric dust. *Planetary and Space Science*, 49(1):71–77, 2001.

[152] Kani Rauf, Anthony Hann, MK Wallis, and NC Wickramasinghe. Evidence for putative microfossils in space dust from the stratosphere. *Int. J. Astrobiology*, 9(3):183–189, 2010.

[153] Vincenzo Della Corte, Frans JM Rietmeijer, Alessandra Rotundi, and Marco Ferrari. Introducing a new stratospheric dust-collecting system with potential use for upper atmospheric microbiology investigations. *Astrobiology*, 14(8):694–705, 2014.

[154] Ian DR Mackinnon and Frans JM Rietmeijer. Mineralogy of chondritic interplanetary dust particles. *Reviews of Geophysics*, 25(7):1527–1553, 1987.

[155] Roy S Lewis, Tang Ming, John F Wacker, Edward Anders, and Eric Steel. Interstellar diamonds in meteorites. *Nature*, 326(6109):160–162, 1987.

[156] A Rotundi, GA Baratta, J Borg, JR Brucato, H Busemann, L Colangeli, L d'Hendecourt, Z Djouadi, G Ferrini, IA Franchi, et al. Combined micro-raman, micro-infrared, and field emission scanning electron microscope analyses of comet 81p/wild 2 particles collected by stardust. *Meteoritics & Planetary Science*, 43(1-2):367–397, 2008.

[157] Jemma Davidson, Henner Busemann, and Ian A Franchi. A nanosims and raman spectroscopic comparison of interplanetary dust particles from comet grigg-skjellerup and non-grigg skjellerup collections. *Meteoritics & Planetary Science*, 47(11):1748–1771, 2012.

[158] Christine Floss, Frank J Stadermann, John P Bradley, Sasa Bajt, Giles Graham, A Scott Lea, et al. Identification of isotopically primitive interplanetary dust particles: A nanosims isotopic imaging study. *Geochimica et Cosmochimica Acta*, 70(9):2371–2399, 2006.

[159] Haifa Alali, Zhiyong Gong, Gorden Videen, Yong-Le Pan, Olga Muñoz, and Chuji Wang. Laser spectroscopic characterization of single extraterrestrial dust particles using optical trapping-cavity ringdown and raman spectroscopy. *Journal of Quantitative Spectroscopy and Radiative Transfer*, 255:107249, 2020.

[160] Agnese Fazio, Luigi Folco, Massimo D'Orazio, Maria Luce Frezzotti, and Carole Cordier. Shock metamorphism and impact melting in small impact craters on earth: Evidence from kamil crater, egypt. *Meteoritics & Planetary Science*, 49(12):2175–2200, 2014.

[161] Alberto Collareta, Massimo D'Orazio, Maurizio Gemelli, Andreas Pack, and Luigi Folco. High crustal diversity preserved in the lunar meteorite mount dewitt 12007 (victoria land, antarctica). *Meteoritics & Planetary Science*, 51(2):351–371, 2016.

[162] L Colangeli, JJ Lopez-Moreno, P Palumbo, J Rodriguez, M Cosi, V Della Corte, F Esposito, M Fulle, M Herranz, JM Jeronimo, et al. The grain impact analyser and dust accumulator (giada) experiment for the rosetta mission: design, performances and first results. *Space Science Reviews*, 128(1-4):803–821, 2007.

[163] Jan Gieseler, Juan Ruben Gomez-Solano, Alessandro Magazzù, Isaac Pérez Castillo, Laura Pérez García, Marta Gironella-Torrent, Xavier Viader-Godoy, Felix Ritort, Giuseppe Pesce, Alejandro V Arzola, et al. Optical tweezers—from calibration to applications: a tutorial. *Advances in Optics and Photonics*, 13(1):74–241, 2021.

[164] Giuseppe Pesce, Giorgio Volpe, Anna Chiara De Luca, Giulia Rusciano, and Giovanni Volpe. Quantitative assessment of non-conservative radiation forces in an optical trap. *EPL (Europhysics Letters)*, 86(3):38002, 2009.

[165] Philip L Marston and James H Crichton. Radiation torque on a sphere caused by a circularly-polarized electromagnetic wave. *Physical Review A*, 30(5):2508, 1984.

[166] Andrea Orlando, Massimo D'Orazio, Pietro Armienti, and Daniele Borrini. Experimental determination of plagioclase and clinopyroxene crystal growth rates in an anhydrous trachybasalt from mt etna (italy). *European Journal of Mineralogy*, 20(4):653–664, 2008.

[167] R Brunetto, C Lantz, D Ledu, D Baklouti, MA Barucci, P Beck, L Delauche, Z Dionnet, P Dumas, J Duprat, et al. Ion irradiation of allende meteorite probed by visible, ir, and raman spectroscopies. *Icarus*, 237:278–292, 2014.

[168] R Cristofolini, MA Menzies, L Beccaluva, and A Tindle. Petrological notes on the 1983 lavas at mount etna, sicily, with reference to their ree and sr—nd isotope composition. *Bulletin of volcanology*, 49(4):599–607, 1987.

[169] M. G. Donato, J Hernandez, A Mazzulla, C Provenzano, R Saija, R Sayed, S Vasi, A Magazzù, P Pagliusi, R Bartolino, et al. Polarization-dependent optomechanics mediated by chiral microresonators. *Nature communications*, 5(1):1–7, 2014.

[170] Paolo Polimeno, Alessandro Magazzu, Maria Antonia Iati, Francesco Patti, Rosalba Saija, Cristian Degli Esposti Boschi, Maria Grazia Donato, Pietro G Gucciardi, Philip H Jones, Giovanni Volpe, et al. Optical tweezers and their applications. *Journal of Quantitative Spectroscopy and Radiative Transfer*, 218:131–150, 2018.

[171] Frederick Gittes and Christoph F Schmidt. Interference model for back-focal-plane displacement detection in optical tweezers. *Optics letters*, 23(1):7–9, 1998.

[172] A Magazzú, D Spadaro, M. G. Donato, R Sayed, E Messina, C D'Andrea, A Foti, B Fazio, MA Iatí, A Irrera, et al. Optical tweezers: a non-destructive tool for soft and biomaterial investigations. *Rendiconti Lincei*, 26(2):203–218, 2015.

[173] Maria Antonia Iatì, Arianna Giusto, Rosalba Saija, Ferdinando Borghese, Paolo Denti, Cesare Cecchi-Pestellini, and Santi Aiello. Optical properties of composite interstellar grains: A morphological analysis. *The Astrophysical Journal*, 615(1):286, 2004.

[174] Maria Antonia Iatì, Rosalba Saija, Ferdinando Borghese, Paolo Denti, Cesare Cecchi-Pestellini, and David A Williams. Stratified dust grains in the interstellar medium–i. an accurate computational method for calculating their optical properties. *Monthly Notices of the Royal Astronomical Society*, 384(2):591–598, 2008.

[175] Karri Muinonen, T Nousiainen, P Fast, Kari Lumme, and JI Peltoniemi. Light scattering by gaussian random particles: ray optics approximation. *Journal of Quantitative Spectroscopy and Radiative Transfer*, 55(5):577–601, 1996.

[176] Zhiyong Gong, Yong-Le Pan, Gorden Videen, and Chuji Wang. Optical trapping and manipulation of single particles in air: Principles, technical details, and applications. *Journal of Quantitative Spectroscopy and Radiative Transfer*, 214:94–119, 2018.

[177] MD Summers, DR Burnham, and D McGloin. Trapping solid aerosols with optical tweezers: A comparison between gas and liquid phase optical traps. *Optics express*, 16(11):7739–7747, 2008.

[178] Tongcang Li. *Fundamental tests of physics with optically trapped microspheres*. Springer Science & Business Media, 2012.

[179] Vladlen G Shvedov, Andrei V Rode, Yana V Izdebskaya, Anton S Desyatnikov, Wieslaw Krolikowski, and Yuri S Kivshar. Giant optical manipulation. *Physical review letters*, 105(11):118103, 2010.

[180] Ryota Omori, Tamiki Kobayashi, and Atsuyuki Suzuki. Observation of a single-beam gradient-force optical trap for dielectric particles in air. *Optics letters*, 22(11):816–818, 1997.

[181] Brandon Redding, Steven C Hill, Dimitri Alexson, Chuji Wang, and Yong-Le Pan. Photophoretic trapping of airborne particles using ultraviolet illumination. *Optics express*, 23(3):3630–3639, 2015.

[182] Bin Zhao, David Katoshevski, and Ezra Bar-Ziv. Temperature determination of single micrometre-sized particles from forced/free convection and photophoresis. *Measurement Science and Technology*, 10(12):1222, 1999.

[183] Vojtěch Svak, Jana Flajšmanová, Lukáš Chvátal, Martin Šiler, Alexandr Jonáš, Jan Ježek, Stephen H Simpson, Pavel Zemánek, and Oto Brzobohatỳ. Stochastic dynamics of optically bound matter levitated in vacuum. *Optica*, 8(2):220–229, 2021.

[184] I Manek, Yu B Ovchinnikov, and R Grimm. Generation of a hollow laser beam for atom trapping using an axicon. *Optics communications*, 147(1-3):67–70, 1998.

[185] Arthur Ashkin and J. M. Dziedzic. Optical levitation by radiation pressure. *Applied Physics Letters*, 19(8):283–285, 1971.

[186] Yong-Le Pan, Aimable Kalume, Isaac CD Lenton, Timo A Nieminen, Alex B Stilgoe, Halina Rubinsztein-Dunlop, Leonid A Beresnev, Chuji Wang, and Joshua L Santarpia. Optical-trapping of particles in air using parabolic reflectors and a hollow laser beam. *Optics Express*, 27(23):33061–33069, 2019.

[187] Arthur Ashkin and JM Dziedzic. Feedback stabilization of optically levitated particles. *Applied Physics Letters*, 30(4):202–204, 1977.

[188] David Bronte Ciriza, Agnese Callegari, Maria Grazia Donato, Berk Çiçek, Alessandro Magazzù, Iryna Kasianiuk, Denis Kasianiuk, Falko Schmidt, Antonino Foti, Pietro G Gucciardi, et al. Optically driven janus micro engine with full orbital motion control. *arXiv preprint arXiv:2305.06688*, 2023.

[189] Alexander D. Fusi, Yudong Li, A. Llopis-Lorente, Tania Patiño, Jan C. M. van Hest, and Loai K. E. A. Abdelmohsen. Achieving control in micro-/nanomotor mobility. *Angewandte Chemie International Edition*, 62(5):e202214754, 2023.

[190] Xiao-Feng Lin, Guo-Qing Hu, Qi-Dai Chen, Li-Gang Niu, Qi-Song Li, Andreas Ostendorf, and Hong-Bo Sun. A light-driven turbine-like micro-rotor and study on its light-to-mechanical power conversion efficiency. *Applied Physics Letters*, 101(11):113901, 2012.

[191] UnėG. Būtaitė, Graham M. Gibson, Ying-Lung D. Ho, Mike Taverne, Jonathan M. Taylor, and David B. Phillips. Indirect optical trapping using light driven micro-rotors for reconfigurable hydrodynamic manipulation. *Nat Commun*, 10(1):1215, 2019.

[192] Falko Schmidt, Alessandro Magazzù, Agnese Callegari, Luca Biancofiore, Frank Cichos, and Giovanni Volpe. Microscopic engine powered by critical demixing. *Physical Review Letters*, 120(6):068004, 2018.

[193] Joseph Wang. Cargo-towing synthetic nanomachines: towards active transport in microchip devices. *Lab on a Chip*, 12(11):1944–1950, 2012.

[194] Maria Guix, Carmen C Mayorga-Martinez, and Arben Merkoçi. Nano/micromotors in (bio) chemical science applications. *Chemical reviews*, 114(12):6285–6322, 2014.

[195] Lluis Soler, Veronika Magdanz, Vladimir M Fomin, Samuel Sanchez, and Oliver G Schmidt. Self-propelled micromotors for cleaning polluted water. *ACS nano*, 7(11):9611–9620, 2013.

[196] Muhammad Safdar, Juliane Simmchen, and Janne Jänis. Light-driven micro-and nanomotors for environmental remediation. *Environmental Science: Nano*, 4(8):1602–1616, 2017.

[197] Andreas Walther and Axel HE Müller. Janus particles. *Soft matter*, 4(4):663–668, 2008.

[198] FS Merkt, Artur Erbe, and Paul Leiderer. Capped colloids as light-mills in optical traps. *New Journal of Physics*, 8(9):216, 2006.

[199] Henrique Moyses, Jérémie Palacci, Stefano Sacanna, and David G Grier. Trochoidal trajectories of self-propelled janus particles in a diverging laser beam. *Soft Matter*, 12(30):6357–6364, 2016.

[200] Spas Nedev, Sol Carretero-Palacios, Paul Kühler, Theobald Lohmüller, Alexander S Urban, Lindsey JE Anderson, and Jochen Feldmann. An optically controlled microscale elevator using plasmonic janus particles. *ACS photonics*, 2(4):491–496, 2015.

[201] Ognjen Ilic, Ido Kaminer, Yoav Lahini, Hrvoje Buljan, and Marin Soljacic. Exploiting optical asymmetry for controlled guiding of particles with light. *Acs Photonics*, 3(2):197–202, 2016.

[202] Hong-Ren Jiang, Natsuhiko Yoshinaga, and Masaki Sano. Active motion of a Janus particle by self-thermophoresis in a defocused laser beam. *Phys. Rev. Lett.*, 105:268302, 2010.

[203] Stefano Palagi, Dhruv P Singh, and Peer Fischer. Light-controlled micromotors and soft microrobots. *Advanced Optical Materials*, 7(16):1900370, 2019.

[204] Ivo Buttinoni, Lorenzo Caprini, Laura Alvarez, Fabian Jan Schwarzendahl, and Hartmut Löwen. Active colloids in harmonic optical potentials (a). *Europhysics Letters*, 140(2):27001, 2022.

[205] Georgiy Tkachenko, Viet Giang Truong, Cindy Liza Esporlas, Isha Sanskriti, and Síle Nic Chormaic. Evanescent field trapping and propulsion of janus particles along optical nanofibers. *Nature Communications*, 14(1):1691, 2023.

[206] DL Fan, Frank Q Zhu, Xiaobin Xu, Robert C Cammarata, and CL Chien. Electronic properties of nanoentities revealed by electrically driven rotation. *Proceedings of the National Academy of Sciences*, 109(24):9309–9313, 2012.

[207] Wei Gao, Daniel Kagan, On Shun Pak, Corbin Clawson, Susana Campuzano, Erdembileg Chuluun-Erdene, Erik Shipton, Eric E Fullerton, Liangfang Zhang, Eric Lauga, et al. Cargo-towing fuel-free magnetic nanoswimmers for targeted drug delivery. *small*, 8(3):460–467, 2012.

[208] Yoshihiko Arita, Michael Mazilu, and Kishan Dholakia. Laser-induced rotation and cooling of a trapped microgyroscope in vacuum. *Nature communications*, 4(1):2374, 2013.

[209] MEJ Friese, J Enger, H Rubinsztein-Dunlop, and Norman R Heckenberg. Optical angular-momentum transfer to trapped absorbing particles. *Physical Review A*, 54(2):1593, 1996.

[210] Marlies EJ Friese, Timo A Nieminen, Norman R Heckenberg, and Halina Rubinsztein-Dunlop. Optical alignment and spinning of laser-trapped microscopic particles. *Nature*, 394(6691):348–350, 1998.

[211] NB Simpson, K Dholakia, L Allen, and MJ Padgett. Mechanical equivalence of spin and orbital angular momentum of light: an optical spanner. *Optics letters*, 22(1):52–54, 1997.

[212] Péter Galajda and Pál Ormos. Complex micromachines produced and driven by light. *Applied Physics Letters*, 78(2):249–251, 2001.

[213] Antonio Alvaro Ranha Neves, Andrea Camposeo, Stefano Pagliara, Rosalba Saija, Ferdinando Borghese, Paolo Denti, Maria Antonia Iatì, Roberto Cingolani, Onofrio M Maragò, and Dario Pisignano. Rotational dynamics of optically trapped nanofibers. *Optics express*, 18(2):822–830, 2010.

[214] Yiwu Zong, Jing Liu, Rui Liu, Honglian Guo, Mingcheng Yang, Zhiyuan Li, and Ke Chen. An optically driven bistable janus rotor with patterned metal coatings. *ACS nano*, 9(11):10844–10851, 2015.

[215] Martin Fränzl, Santiago Muinos-Landin, Viktor Holubec, and Frank Cichos. Fully steerable symmetric thermoplasmonic microswimmers. *ACS nano*, 15(2):3434–3440, 2021.

[216] Claudio Maggi, Filippo Saglimbeni, Michele Dipalo, Francesco De Angelis, and Roberto Di Leonardo. Micromotors with asymmetric shape that efficiently convert light into work by thermocapillary effects. *Nature communications*, 6(1):7855, 2015.

[217] A Girot, N Danné, A Wurger, Thomas Bickel, F Ren, JC Loudet, and B Pouligny. Motion of optically heated spheres at the water–air interface. *Langmuir*, 32(11):2687–2697, 2016.

[218] Jing Liu, Hong-Lian Guo, and Zhi-Yuan Li. Self-propelled round-trip motion of janus particles in static line optical tweezers. *Nanoscale*, 8(47):19894–19900, 2016.

[219] S Masoumeh Mousavi, Iryna Kasianiuk, Denis Kasyanyuk, Sabareesh KP Velu, Agnese Callegari, Luca Biancofiore, and Giovanni Volpe. Clustering of janus particles in an optical potential driven by hydrodynamic fluxes. *Soft matter*, 15(28):5748–5759, 2019.

[220] Diptabrata Paul, Rahul Chand, and GV Pavan Kumar. Optothermal evolution of active colloidal matter in a defocused laser trap. *ACS Photonics*, 9(10):3440–3449, 2022.

[221] Étienne Fodor and Michael E Cates. Active engines: Thermodynamics moves forward. *Europhysics Letters*, 134(1):10003, 2021.

[222] Massimo Antognozzi, CR Bermingham, RL Harniman, Stephen Simpson, Jorden Senior, Rosie Hayward, Heinrich Hoerber, MR Dennis, AY Bekshaev, KY Bliokh, et al. Direct measurements of the extraordinary optical momentum and transverse spin-dependent force using a nano-cantilever. *Nature Physics*, 12(8):731–735, 2016.

[223] Lukas Novotny and Bert Hecht. *Principles of nano-optics*. Cambridge university press, 2012.

[224] Stephen M Barnett and L Allen. Orbital angular momentum and nonparaxial light beams. *Optics communications*, 110(5-6):670–678, 1994.

[225] Xiaoqing Gao, Yali Wang, Xuehao He, Mengjun Xu, Jintao Zhu, Xiaodong Hu, Xiaotang Hu, Hongbin Li, and Chunguang Hu. Angular trapping of spherical janus particles. *Small Methods*, 4(12):2000565, 2020.

[226] J L Anderson. Colloid transport by interfacial forces. *Annual Review of Fluid Mechanics*, 21(1):61–99, 1989.

[227] Andreas P Bregulla and Frank Cichos. Flow fields around pinned self-thermophoretic microswimmers under confinement. *The Journal of chemical physics*, 151(4):044706, 2019.

[228] Samuel Sánchez, Lluís Soler, and Jaideep Katuri. Chemically powered micro-and nanomotors. *Angewandte Chemie International Edition*, 54(5):1414–1444, 2015.

[229] Alberto Credi. Artificial molecular motors powered by light. *Australian journal of chemistry*, 59(3):157–169, 2006.

[230] Jeremie Palacci, Stefano Sacanna, Asher Preska Steinberg, David J Pine, and Paul M Chaikin. Living crystals of light-activated colloidal surfers. *Science*, 339(6122):936–940, 2013.

[231] Mite Mijalkov, Austin McDaniel, Jan Wehr, and Giovanni Volpe. Engineering sensorial delay to control phototaxis and emergent collective behaviors. *Physical Review X*, 6(1):011008, 2016.

[232] Giorgio Volpe, Lisa Kurz, Agnese Callegari, Giovanni Volpe, and Sylvain Gigan. Speckle optical tweezers: micromanipulation with random light fields. *Optics express*, 22(15):18159–18167, 2014.

[233] Stephen H Simpson and Simon Hanna. Optical trapping of spheroidal particles in gaussian beams. *JOSA A*, 24(2):430–443, 2007.

[234] Alexander R Sprenger, Miguel Angel Fernandez-Rodriguez, Laura Alvarez, Lucio Isa, Raphael Wittkowski, and Hartmut Löwen. Active brownian motion with orientation-dependent motility: theory and experiments. *Langmuir*, 36(25):7066–7073, 2020.

[235] Sriram Ramaswamy. The mechanics and statistics of active matter. *Annu. Rev. Condens. Matter Phys.*, 1(1):323–345, 2010.

[236] Clemens Bechinger, Roberto Di Leonardo, Hartmut Löwen, Charles Reichhardt, Giorgio Volpe, and Giovanni Volpe. Active particles in complex and crowded environments. *Reviews of Modern Physics*, 88(4):045006, 2016.

[237] Grover A Swartzlander, Timothy J Peterson, Alexandra B Artusio-Glimpse, and Alan D Raisanen. Stable optical lift. *Nature Photonics*, 5(1):48–51, 2011.

[238] Roberto Piazza and Alberto Parola. Thermophoresis in colloidal suspensions. *Journal of Physics: Condensed Matter*, 20(15):153102, 2008.